2. AUTOMOTIVE METALS—WROUGHT

A. Thermomechanical Processing Design for Lightweight Materials

Principal Investigator: Esteban B. Marin
Senior Structural Analyst
Center for Advanced Vehicular Systems
Mississippi State University
200 Research Blvd.
Mississippi State, MS 39762
(662) 325-6696; fax: (662) 325-5433; e-mail: ebmarin@cavs.msstate.edu

Co-Principal Investigators: Paul T. Wang
Manager, Computational Manufacturing and Design
Center for Advanced Vehicular Systems
Mississippi State University
P.O. Box 5405
Mississippi State, MS 39762-5405
(662) 325-2890; fax: (662) 325-5433; e-mail: pwang@cavs.msstate.edu

Wei Chen
Professor of Mechanical Engineering
Robert R. McCormick School of Engineering and Applied Science
Northwestern University
Department of Mechanical Engineering
2145 Sheridan Road
Evanston, Illinois 60208-3111
(847) 491-7019; fax: (847) 491-3915; e-mail: weichen@northwestern.edu

Jian Cao
Professor of Mechanical Engineering
Robert R. McCormick School of Engineering and Applied Science
Northwestern University
Department of Mechanical Engineering
2145 Sheridan Road
Evanston, Illinois 60208-3111
(847) 467-1032; fax: (847) 491-3915; e-mail: jcao@northwestern.edu

Participants:
Sebastien Groh
Center for Advanced Vehicular Systems
Mississippi State University
200 Research Blvd.
Mississippi State, MS 39762
(662) 325-5576; fax: (662) 325-5433; email: groh@cavs.msstate.edu

Stephen Horstemeyer
Center for Advanced Vehicular Systems
Mississippi State University
200 Research Blvd.
Mississippi State, MS 39762
(662) 325-3685; fax: (662) 325-5433; email: sjhorst@cavs.msstate.edu

Andrew Oppedal
Center for Advanced Vehicular Systems
Mississippi State University
200 Research Blvd.
Mississippi State, MS 39762
(662) 325-8502; fax: (662) 325-5433; email: aoppedal@cavs.msstate.edu

Balasubramaniam Radhakrishnan
Oak Ridge National Laboratory
P.O. Box 2008
Oak Ridge, TN 37831-6164
(865) 241-3861; fax: (865) 241-0381; e-mail: radhakrishnb@ornl.gov

Gorti Sarma
Oak Ridge National Laboratory
P.O. Box 2008
Oak Ridge, TN 37831-6164
(865) 574-5147; fax: (865) 241-0381; e-mail: sarmag@ornl.gov

Joe Horton
Oak Ridge National Laboratory
P.O. Box 2008
Oak Ridge, TN 37831-6487
(865) 574-5575; fax: (865) 574-7659; e-mail: hortonja@ornl.gov

Technology Area Development Manager: Joseph A. Carpenter
(202) 586-1022; fax: (202) 586-1600; e-mail: joseph.carpenter@ee.doe.gov

---

Contractor: Mississippi State University (MSST)
Contract No.: 4000054701

Objective

- Develop physics-based, experimentally-validated, thermomechanical processing (TMP) models and design methodologies for improving manufacturability and forming technology of lightweight materials such as wrought aluminum (Al) and magnesium (Mg) alloys.

Approach

- Build an experimental material database that captures the important features of microstructure evolution during hot/cold rolling and stamping, and extrusion processes of Al and Mg alloys.
- Develop a multiscale material model using an internal state variable (ISV) formalism that is able to predict microstructure evolution (hardening, recovery, recrystallization, and texture-induced anisotropy) of metals during TMP.

- Construct numerical models of metal forming (rolling, stamping, extrusion) for process design.
- Use optimization techniques with uncertainty to establish an integrated approach for material-process design using simulation-based techniques.
- Main activities (subtasks) planned to perform the proposed research areas are as follows.
  - — Develop plane-strain compression (rolling), biaxial stretching (stamping), and laboratory-scale extrusion techniques for Al/Mg alloys at room and elevated temperature.
  - — Build an experimental database capturing microstructure evolution of Al alloys.
  - — Perform pilot-scale rolling experiments and material characterization of Mg alloys.
  - — Extend experimental database with microstructure information for Mg alloys.
  - — Develop multiscale ISV model to predict microstructure evolution of Al and Mg alloys during TMP.
  - — Construct thermomechanical process models and develop manufacturability metrics for process design (rolling, stamping, and extrusion).
  - — Develop methodologies for uncertainty quantification and reliability based design optimization of metal-forming processes.

- Team members participating in this task are as follows.
  - — MSST: Paul Wang, Esteban Marin (macroscale ISV model development, extrusion modeling), Sebastien Groh (support ISV model development with microscale/discrete dislocation/crystal plasticity simulations), Stephen Horstemeyer (laboratory-scale extrusion experiments), and Andrew Opeddal (mechanical testing of magnesium).
  - — Oak Ridge National Laboratory (ORNL): Balasubramaniam Radhakrishnan and Gorti Sarma (support ISV model development with mesoscale/crystal plasticity simulations), and Joe Horton (pilot-scale rolling experiments and characterization of Mg alloys).
  - — Northwestern University (NWU): Jian Cao (biaxial stretching experiments and stamping simulations), and Wei Chen (design optimization under uncertainty).

Accomplishments

- Performed channel die compression (CDC) experiments at room temperature (RT) on Al 6022 with a new-designed fixture that improved the outcome of the plane-strain compression tests. Compressed specimens (reduction of 60%) were annealed at different temperatures and times, and then subjected to microindentation tests. Hardness measurements showed the sigmoidal shape typically depicted by plots of differential hardness versus annealed time. Electron backscatter diffraction (EBSD) studies have been initiated on the annealed specimens to quantify the fraction of recrystallized material and model the recrystallization kinetics of aluminum alloys.
- Completed mechanical testing and texture measurements of pure polycrystalline magnesium deformed under simple compression have been completed. In these experiments, samples extracted from extruded/rolled plates were compressed in the through thickness (TT) and in-plane transverse (IPT) directions. Results from these tests (stress-strain curves and texture) showed clearly the effect of twinning on the deformation behavior of the material. Additional experiments considering strain-path changes and temperature reloads are works in-progress.
- Rolled, tested, and analyzed 19 alloys from a set of 97 experimental alloy slabs cast by Magnesium Elektron North America Inc. (MENA). A recipe adapted to ORNL's mill size was developed to allow hot rolling of these slabs to a thickness of 1.5 mm. Several of the alloys have strengths and ductilities near those of AZ31. Recovery/recrystallization on one selected alloy (AZ31b-H24) showed that only 15 min at 200°C or 8 min at 250°C was required for recovery as contrasted with the standard *ASM Handbook* recommendations of 1 hour at 345°C.
- Performed preliminary extrusion tests on Mg AZ61 using a laboratory-scaled, indirect-extrusion fixture designed to learn about the process and generate experimental data for modeling purposes. Experiments were not fully successful but limited microstructure information (texture, grain maps and grain orientation spread) was obtained at specific points of the material as it was flowing through the die. A new design for the fixture is currently underway.

- Performed quasi-statics and dynamics calculations in Mg to establish a dislocation mobility rule for each slip system. Peierls stresses (minimum stress needed to move a dislocation at 0°K) were calculated for each slip system, and a good agreement with experimental data was obtained. At finite temperatures two types of anisotropy were identified, which were related to (1) the dislocation character and (2) the slip system. Independently of the slip systems, edge dislocations move faster than screw dislocations, and regardless of the dislocation character (edge or screw), dislocations moving in the basal plane travel faster than dislocations sliding in the prismatic plane. Viscous-drag coefficients were calculated for each character lying in each slip system.
- Implemented and tested kinematics, kinetics and hardening rules for twinning deformation in a crystal-plasticity code. Analyzed dislocation/twin activities in a Mg single crystal under different loading conditions and used that information to identify the parameters of slip-hardening rules. This multiscale material model of Mg alloys reproduced well the anisotropy reported in the literature.
- Developed a new recovery model for cube texture evolution in Al. The nucleation model was based on orientation dependent "excess dislocations" and was incorporated into Monte Carlo recrystallization simulations. The model successfully predicted strengthening of cube texture during recrystallization following plane-strain compression.
- Investigated kinematic-hardening behavior in sheet metals using a novel design of test apparatus and a new model. An attempt on simulating material behavior of Mg alloys was made using a phenomenological approach. A method was developed for establishing the multilength-scale statistical microstructure-constitutive property relations through the statistical volume element (SVE) method, statistical sensitivity analysis, and stochastic calibration. Efficient random field uncertainty propagation techniques were developed for robust and reliability-based design involving multiscale analysis. Generic computational methods were established for robust design considering uncertainty with arbitrary distributions.

Future Direction

- Finish EBSD analyses (i.e., local texture) on channel die compressed specimens. Extend the capabilities of the CDC setup to test materials at high temperatures. Initiate experimental recrystallization studies for Mg alloys.
- Finish experiments considering strain-path changes and temperature reloads of pure Mg. Characterize the microstructure of the deformed specimens: measure bulk texture via neutron diffraction and microtexture and evolution of twinning via EBSD. Develop a dislocation-based, strain-rate- and temperature-dependent constitutive model for Mg. Implement model in crystal-plasticity numerical codes and use it to predict the experimental results, in particular the evolution of deformation twinning.
- Perform laboratory-scale extrusion experiments to study the effect of processing parameters on the microstructure and material properties of extruded Mg alloys. Develop finite-element models of the extrusion process. Validate material and numerical models by comparing predictions with experimental data from the laboratory-scale experiments.
- Use molecular dynamics (MD) simulation to complete the calculation of dislocation velocities in pure Mg. Exercise the discrete dislocation simulation code to compute the interaction coefficient between different slip systems (basal, prismatic, and pyramidal) for use in the hardening law of crystal-plasticity models. Validate the multiscale methodology established previously for Al by predicting the mechanical response of Mg single crystals.
- Conduct experimental investigation of forming limits of Mg alloys and forming behavior in stamping, and correlate the results with numerical simulations. Demonstrate the use of robust and reliability-based design framework for optimizing the sheet-metal forming process for Mg alloys.
- No new activities are planned by the team members at ORNL due to the lack of funding.

Introduction

Thermomechanical processing is typically used to improve mechanical properties of a material by inducing changes in its microstructure (grain structure, texture, precipitates). Properties such as plasticity, strength, ductility, and formability can be tailored by a proper design of different steps in TMP (e.g., hot/cold rolling, extrusion, heat treatment, stamping) as well as the design of material microstructure. In this context, building robust design methodologies and multiscale material models under uncertainty for TMP can contribute to improve current manufacturing processes and/or fix many technical problems (e.g., formability) that at present hinder the production of selected lightweight materials such as Mg alloys.

The focus of this task is to build a comprehensive framework that facilitates the reliability based optimum design of TMP for lightweight materials. This framework includes building an extensive material database capturing the processing-structure-property relationship of Al and Mg alloys, developing a multiscale constitutive approach for the history-dependent response of the alloys, and establishing an integrated robust and reliability optimization method with uncertainty for TMP as applied to Al and Mg alloys.

Based on these three major activities, the presentation below has been divided in three sections; each of them describes the details of the work performed by team members during 2008.

Material Database for Al and Mg Alloys

Channel Die Compression and Annealing of Al 6022 (MSST)

A previously constructed CDC fixture was redesigned to better control the homogeneity of deformation during the RT plane-strain compression experiments (Figure 1). Using this new fixture, CDC tests were performed on samples of Al 6022 extracted from a 1/8 in. rolled plate.

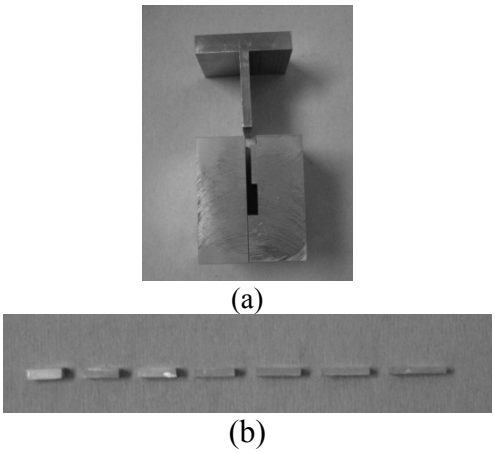

Figure 1. (a) Redesigned CDC fixture and (b) deformed specimen at different levels of strain (up to 50% strain). This new fixture promotes a more uniform deformation of the Al 6022 specimens.

Each CDC test used two specimens, with dimensions 5 mm × 10 mm, stacked and super-glued together to prevent the surfaces from sliding along one another. To reduce friction between the samples and the channel die, the samples were wrapped in Teflon tape and polytetraflouroethylene powder was applied to the surfaces. Using an Instron machine and the CDC fixture, the samples were then compressed up to a strain of 60% at a rate of 0.05 in./min.

The deformed samples were then annealed in a salt bath at temperatures of 375 and 400°C, with annealing times varying from 0 to 5,000 seconds (Figure 2). After the prescribed annealing time, each sample was removed from the furnace and immediately quenched in water.

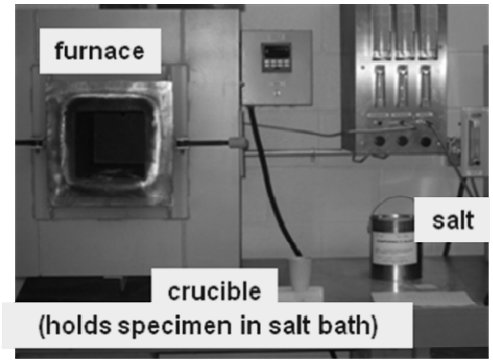

Figure 2. Annealing equipment for CDC samples of Al 6022.

The annealed samples were next prepared for hardness measurement using a microindenter. As expected, the hardness values decrease for longer annealing times and for higher temperatures [Figure 3(a)]. The plot of differential hardness versus annealing time [Figure 3(b)] shows a typical sigmoidal shape representative of recrystallization processes. Currently, the annealed samples are being prepared for EBSD studies to quantify the fraction of recrystallized grains, information needed to model the recrystallization kinetics in Al alloys.

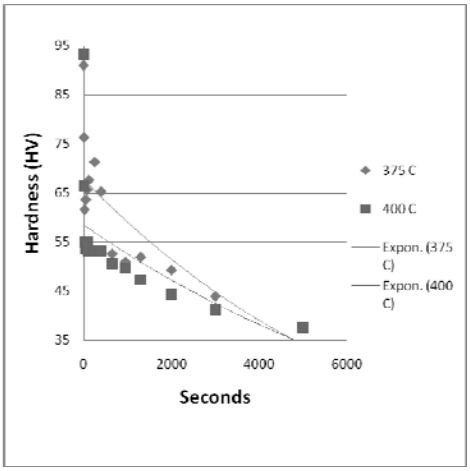

(a)

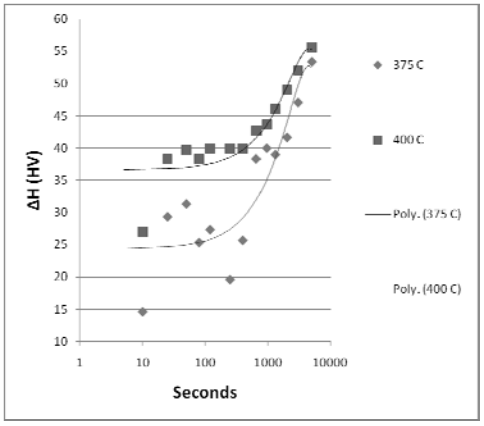

(b)

Figure 3. (a) Hardness vs time and (b) differential hardness vs time for the annealed Al 6022 specimens (HV denotes the Vickers Hardness).

Mechanical Testing and Texture Measurements on Pure Polycrystalline Magnesium (MSST)

Magnesium has attractive properties in applications that favor lower weight [1]. Its density (1.73 g/cm^3) is among the lowest of common structural metals, yet its hexagonal close-packed (hcp) structure demands additional consideration because of the limited ductility and mechanical anisotropy compared to face-centered cubic (fcc) and body-centered cubic (bcc) metals. Magnesium alloys such as AZ31, AM50, and AM60 and newer alloys recently developed such as AM30, AZ61, and AE44 will fill the market need as lighter-weight, more fuel-efficient vehicles become important. Because of this, understanding the structure-property relationships of Mg and its alloys, in particular the effect of deformation twinning on mechanical properties, will contribute to a better use of these materials in technological applications.

In this context, simple compression experiments have been conducted on polycrystalline pure Mg samples cut via electrical discharge machining from extruded and rolled plates. The samples were tested in the TT and IPT directions at RT and a strain rate of 10^{-3} s^{-1}. Figure 4 shows the

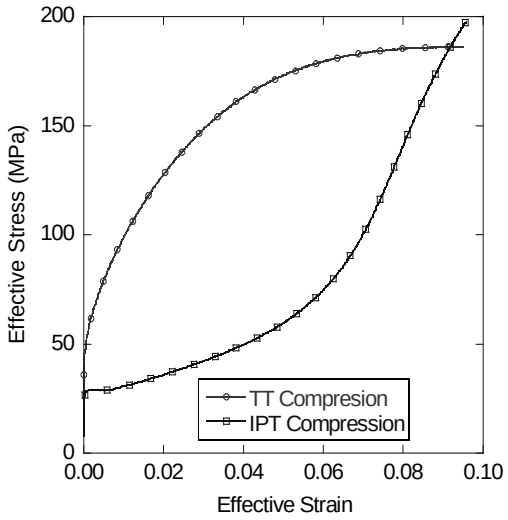

Figure 4. Simple compression of pure polycrystalline Mg showing anisotropy caused by basal texture and twinning. TT compression has the characteristic "parabolic" shape, while IPT compression has a characteristic "sigmoidal" shape caused by twinning activity.

mechanical behavior of the material while Figures 5, 6, and 7 show, respectively, the initial texture and resulting texture after mechanical testing. Note the effect of twinning on both the mechanical response and texture evolution. Texture was determined via neutron diffraction and represents the bulk texture of the material.

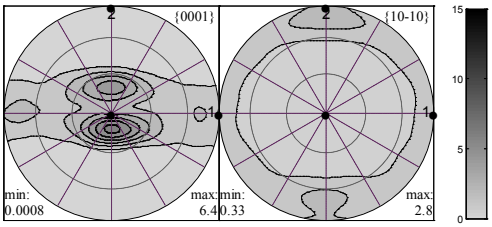

Figure 5. Initial texture of extruded/rolled material. The texture is dominated by the orientation of the basal poles.

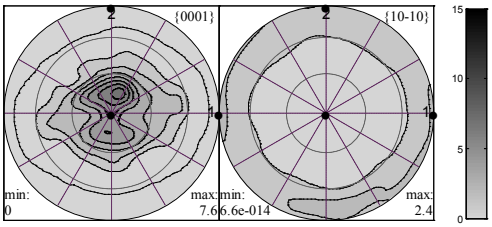

Figure 6. Texture after TT compression of 9.5%. Note the sharpening of the texture.

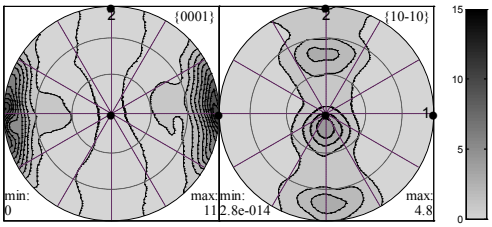

Figure 7. Texture after IPT compression of 9.6%. Note rotation of basal pole.

Additional experiments are being conducted to characterize the material under strain-path changes and temperature reloads. In the strain-path change experiment, an initial compression preload in the TT (IPT) direction is followed by a reload in the IPT (TT) direction. In the temperature-reload experiment, the material is preloaded in the TT (IPT) direction at liquid nitrogen temperature to create twinned structures, and subsequently reloaded in the TT (IPT) direction at RT. In all these experiments, the interplay between twin and slip will be examined and the results will be used for model development.

Rolling and Annealing Experiments on Magnesium Alloys (ORNL)

The goal of these experiments is to develop a wrought Mg alloy and/or processes for the cost-effective production of Mg sheet which is both economical and formable enough for practical application in vehicle structures. Current work is centered on an alloy development program to produce a lower-cost wrought alloy with properties close to those of AZ31. In this frame, activities during the last year were concentrated in two areas: (1) evaluating the feasibility of using innovative roll processing together with lower-cost alloyed ingots to reduce the total cost of sheet materials and (2) developing a basic understanding of the mechanisms of deformation and recrystallization in order to develop less-expensive processing methods.

Pilot-scale rolling experiments at ORNL were continued on 11 new alloy compositions provided by MENA. Eight other alloys failed to roll. The rolling schedule, developed for a laboratory-sized 6 in. mill, was similar to the one described in the previous annual report and essentially consisted of overnight annealing at 400°C, hot rolling at 400°C with different reductions and reheating steps and then cold rolling. Table 1 shows RT tensile properties at a strain rate of 10^{-3} for these laboratory-scale rolled alloys. As with the alloys reported previously, several of these new alloys have properties similar to those for AZ31.

Annealing experiments were also performed on specimens of as-received commercial AZ31b-H24. The annealing was carried out in air, for the times and temperatures indicated by the graph in Figure 8. This alloy in the as received condition cracked after 7% additional cold rolling, indicating that the cold work in the specimens was near a comfortable limit to simulate the required times and temperatures for intermediate anneals during multiple rolling operations. As evident from the graph, substantial recovery occurred in 15 min at 200°C or just 8 min at 250°C. Metallography for grain size and determination of when

Table 1. Tensile properties of successfully rolled experimental wrought magnesium alloys. (hr = hot rolling; cr = cold rolling

Alloy #	Processing	Yield (MPa)	Tensile (MPa)	Elong (%)
az31*	hr	145	263	14
	hr+10%cr	145	145	0
mel 102	hr	128	230	25
	hr+10%cr	246	257	5.2
	hr+20%cr	283	283	0.3
mel 105	hr	95	220	23
	hr+10%cr	242	254	2.8
	hr+20%cr	263	269	4.2
mel 108	hr	187	203	2.6
	hr+10%cr	23	238	0
mel 118	hr	142	236	21
	hr+10%cr	230	251	10
	hr+20%cr	274	281	2.3
mel 119	hr	165	239	14
	hr+10%cr	256	269	4
mel 120	hr	127	212	5.4
	hr+10%cr	220	237	0.6
mel 138	hr	111	238	24
	hr+10%cr	244	266	6
	hr+20%cr	287	294	3
mel 139	hr	114	225	13
	hr+10%cr	226	253	4.5
mel 140	hr	84	207	6.6
	hr+10%cr	216	216	0
mel 185	hr	123	179	19
	hr+10%cr	159	234	9
	hr+20%cr	211	231	9

*az31 cast into 1/2 slab at mel, hot rollec at ornl

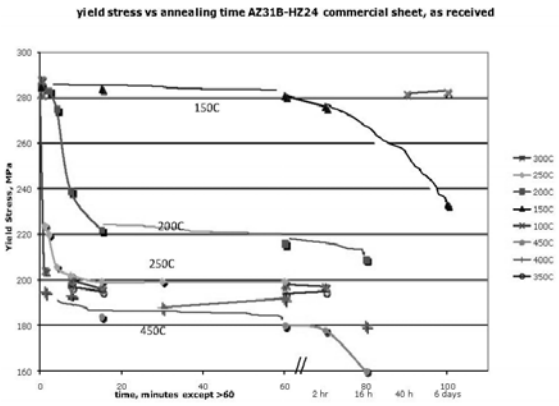

Figure 8. Recovery (tensile stress) of commercial AZ31b-H24 after the indicated times and temperatures for air anneals.

recrystallization occurred has not been performed yet.

In summary, a series of new compositions that were cast in laboratory-sized ingots by MENA were successfully hot rolled and tested at ORNL. Some of the compositions showed comparable results to AZ31, suggesting that this alloying approach may achieve the goal of a less-expensive alloy that is still comparable in properties. Recovery/recrystallization studies showed that 15 min at 200°C or 8 min at 250°C was sufficient for recovery, suggesting that a continuous rolling process should be possible.

Experimental and Numerical Investigation of Kinematic Hardening Behavior in Sheet Metals (NWU)

Northwestern University has been continuously working on the experimental apparatus for testing material's kinematic hardening behavior of thin sheets. A novel in-plane tension-compression device was introduced for sheet materials (Figure 9).

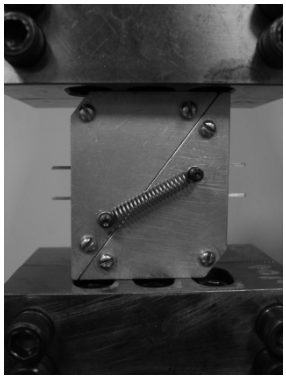

Figure 9. Front view of the test apparatus.

This double-wedge device is easy to fabricate and able to cover the specimen surface completely, preventing potential buckling of sheet. Using the developed device, the frictional force between the plate and specimen can be neglected for both tension and compression tests. The TT biaxial stress and plane-strain condition were also investigated by using the finite-element modeling (FEM) simulation for the compression test. Once the Teflon film was attached on the plate, the material status was not under the plane-strain condition, which is desired for the uniaxial tension-compression test. Also, the stress ratio between the equivalent stress and the compressive axial loading stress was less than 1.6%, so that the biaxial effect of the TT stress can be ignored in the

tension-compression test using the double-wedge device.

To measure the strain correctly, the transmission type laser extensometer was used and the double-side fins were considered in the specimen, as depicted in Figure 10. Through FEM simulations, it was found that the specimen with double-side fins resulted in a more uniform strain distribution than that from the specimen with single-side fins. Test results showed that the double-wedge device can perform stable tension-compression (15% prestrain) and compression-tension (9% prestrain) tests for a sheet thickness of 0.8 mm and a good repeatability for a couple of cyclic tests (Figure 11).

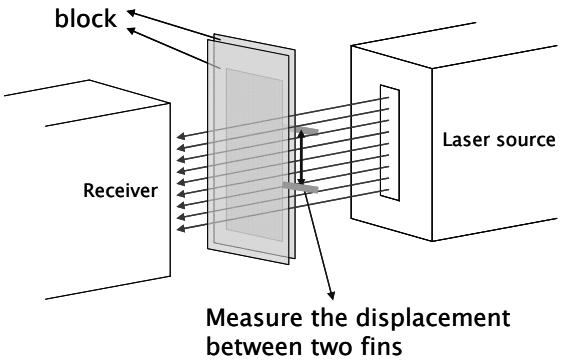

Figure 10. Strain measurement system used.

Laboratory-Scale Extrusion Experiments (MSST)

Extruded structural components of Mg alloys are increasingly being used in the automotive industry due to their good mechanical properties, including low density and high specific strength. However, the extrudability of these alloys is still limited because of their highly anisotropic mechanical behavior originating from their hcp structure. Because of this, understanding the microstructure-property relationship of these alloys as related to the extrusion process can help to improve their manufacturability.

In this subtask, we are developing a laboratory-scale indirect extrusion facility to determine the processing-structure-property relationship of extruded Mg AZ61 and AM30 alloys. Direct extrusion could be designed by this concept. The main goal is to understand the influence of process parameters (temperature, pressure, ram speed, extrusion ratio) on the microstructure and mechanical properties of extruded material and to generate experimental data for model validation.

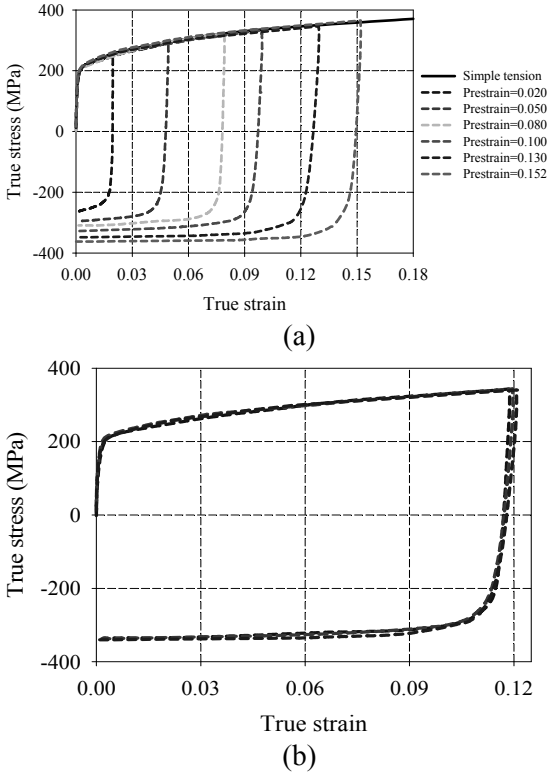

Figure 11. Test results of the 0.8 mm BH180 steel sheet: (a) tension-compression test; (b) repeatability (at 0.12 prestrain level).

A preliminary design of this device has been tested by extruding Mg AZ61 (Figure 12).

Although the test was not completely successful (extrudate came out in fractured parts) possibly due to unsuitable processing conditions (temperature and ram speed), some microstructure information was obtained through EBSD. Figures 13 and 14 show the device cut in half to exhibit the Mg alloy and the grain map, texture, and grain orientation spread (GOS) obtained at two points as the material was flowing though the die. This preliminary test gave some insights on how to modify the device to be reusable and hence able to test a batch of Mg alloy billets under new processing conditions. This new design is a work-in-progress.

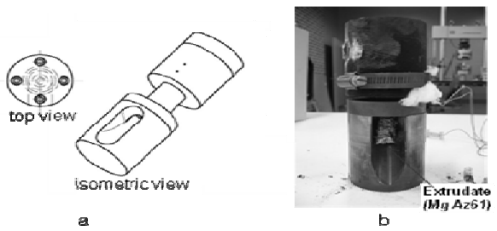

Figure 12. (a) Drawing of extrusion device; device is mounted in a servohydraulic loading frame with a capacity of 67,000 lb. (b) Device after preliminary testing; processing parameters used were temperature = 583°C, ram speed = 1.4 in./min, extrusion ratio = 22.

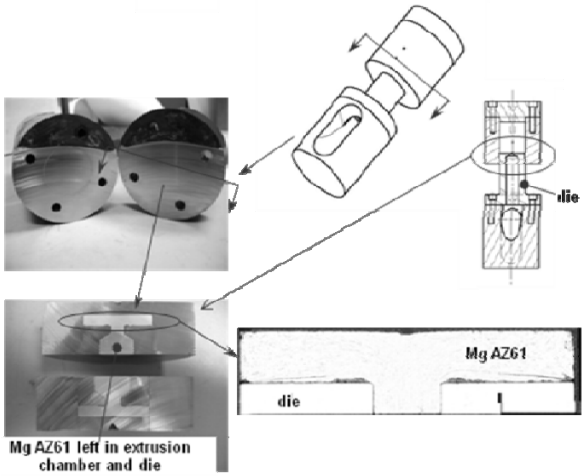

Figure 13. Details of extrusion chamber, die, and material (Mg AZ61) after preliminary test, the material welded to the walls of the chamber and die. Device had to be cut in half twice to exhibit the material flow during extrusion.

Constitutive Model Development/Implementation

Dislocation Motion in Magnesium by Molecular Static and Molecular Dynamics Simulations (MSST)

Metals with hcp crystal structure such as Mg have a wide variety of mechanical and physical properties, and understanding the links between atomic properties, microstructure, and mechanical properties can open the way for new applications. In this sense, atomistic simulations can provide a good deal of information to understand their deformation mechanisms and how these mechanisms affect the overall mechanical behavior of hcp materials.

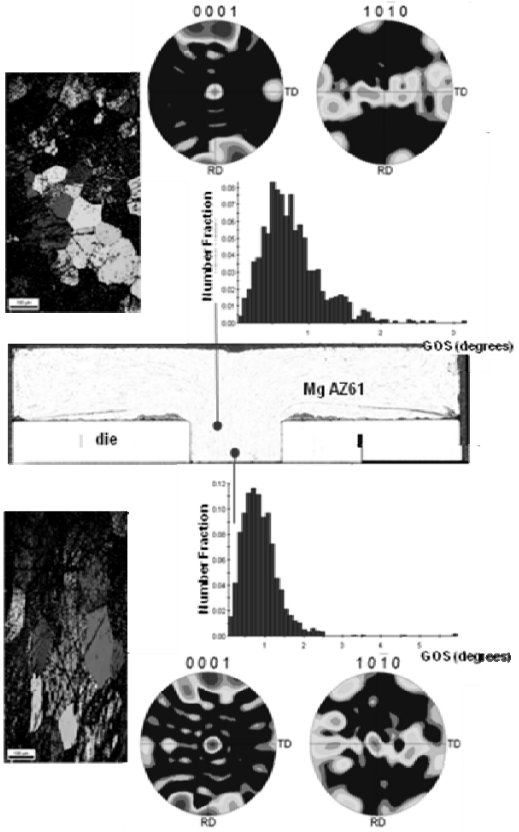

Figure 14. Microstructure information (texture, grain map, GOS) obtained from two points of the material as it was flowing through the extrusion die.

Figure 15 shows the possible dislocation slip systems able to accommodate plastic deformation in hcp crystals. From these, basal, prismatic, and <**c+a**>-pyramidal are the most active slip systems in Mg. basal and prismatic are perpendicular to the **c**-axis, and therefore, slip in <**a**> direction cannot produce strain parallel to the **c**-axis. Dislocations lying in the <**c+a**>-pyramidal slip plane can accommodate deformation along the **c**-axis, but such activity is mainly active at high temperatures. On the other hand, deformation twinning can contribute to the general deformation along the **c**-axis at low temperatures.

A multiscale modeling framework developed previously for fcc materials [2] has shown that the mechanical response of a material can be related to (1) the intersections and reactions between dislocations and (2) the average dislocation velocity. In an effort to extend such a framework to hcp materials, this work focused on studying the

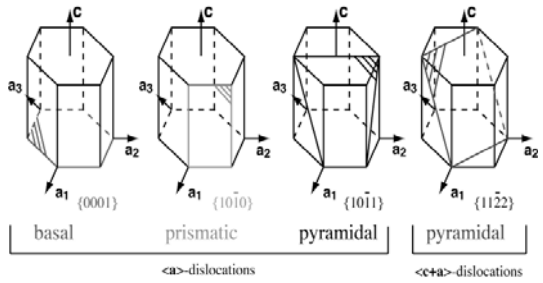

Figure 15. Slip system in hcp crystals.

motion of dislocations on basal, prismatic and <**a**>-pyramidal slip systems (Figure 15). In particular, the study investigates the mobility of edge/screw dislocations with a $1/3[11\bar{2}0]$ Burgers by both molecular statics (MS) and MD simulations. The goal is to derive a dislocation velocity rule usable for simulation at a higher length scale (i.e., discrete dislocations model). In what follows, we present a summary of the methodology, including the description of the dislocation core structures obtained to start the simulations, the quasi-static calculations performed to compute the Peierls stress and the dynamic calculations to determine the mobility of dislocations.

Simulation Setup

The evolution of the dislocation mobility as a function of dislocation character, temperature, and shear stress is studied using the MD code LAMMPS [3], where the simulations can be run under either static- or dynamic-loading conditions.

This section presents the main characteristics of the MS/MD simulation models that allow the analysis of edge/screw dislocations in an infinite periodic glide plane. The simulations employed the embedded-atom method (EAM) potential developed by [4]. For the edge dislocations, periodic boundary conditions were applied along the line and motion directions, while the top and bottom surfaces were fixed along their normal direction and constrained to two-dimensional dynamics. For the screw dislocations, periodicity along the line direction was insured by the invariance of the displacement field in this direction. Along the moving direction, periodic boundary conditions were applied with a shift of +b/2 (b is the Burgers vector) along the line direction for atoms leaving the cell from the left hand negative surface and the reentering the cell on the right hand positive surface. For atoms moving in the opposite direction, an opposite shift was applied.

For the static analysis, a rigid displacement was applied in the direction of the Burgers vector to model the motion of an edge dislocation. The critical stress value at which the dislocation moves defines the Peierls stress. The stress is calculated using the engineering definition (i.e., $\sigma_{dn} = F_{int}/A_{dL}$, where F_{int} is the applied force and A_{dL} is the area of the top surface).

In dynamic conditions and for temperatures greater than 0°K, the applied stress was implemented through a constant force to each atom on the top surface. Calculations were performed using the microcanonical ensemble (NVE) with a time step of 0.002 picoseconds (ps).

Structure of the Dislocation Core

Figure 16 shows the core structure of the basal, prismatic, and pyramidal-<a> edge dislocation, obtained after minimization of the potential energy. The core of the basal edge dislocation (c.f. Figure 16a) dissociated into two Shockley partials bounding an intrinsic fault I_2 according to the reaction

$$\frac{1}{3}[11\bar{2}0] \rightarrow \frac{1}{3}[10\bar{1}0] + \frac{1}{3}[01\bar{1}0],$$

and a distance close to 8b separated the two partials. The core structure of the prismatic edge dislocation (cf Figure 16b) was undissociated, but spreads in the plane $(10\bar{1}0)$, while the dislocation core structure of the edge dislocation lying in the pyramidal plane remained undissociated (c.f. Figure 16c), independently of the position of the origin chosen for the initial elastic solution. Note that the different core structures obtained will affect (1) the value of the Peierls stress and (2) the mechanism of motion.

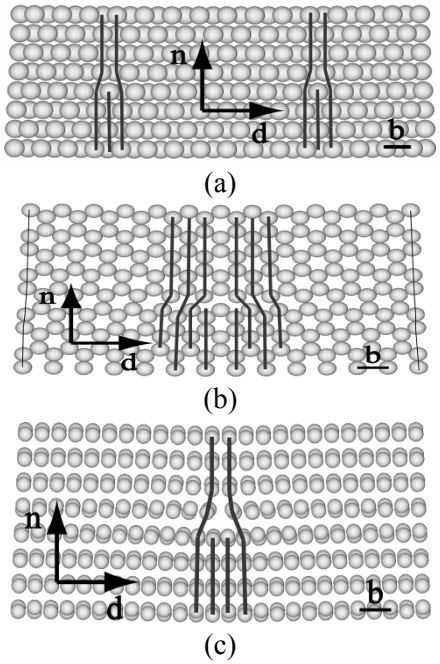

Figure 16. Core structure of <a> -edge dislocation in the (a) basal, (b) prismatic, and (c) pyramidal planes.

Estimation of the Peierls Stress by Molecular Statics

Molecular static calculations were performed to estimate the value of the Peierls stress for edge dislocations lying in the basal, prismatic, and pyramidal slip planes. As a reference, the size of the simulation cell was 100b × 100b along the displacement and normal directions. To capture the simple Peierls picture and not a more complicated mechanism of motion (simple kink or kink-pairs mechanisms), the dimension of the simulation cell along the dislocation line was restricted to one lattice period (i.e., 0.55 nm, 0.52 nm and 1.18 nm for basal, prismatic, and pyramidal crystallographic orientations, respectively). A strain increment $\Delta\varepsilon = 10^{-5}$ applied on the top surface followed by relaxation to the minimum potential energy was repeated until the total strain reached 0.2% for the basal and prismatic crystal orientations and 0.5% for the pyramidal orientation.

Figure 17 shows the strain-stress behaviors calculated for the basal, prismatic, and pyramidal edge dislocations. In the cases of prismatic and pyramidal edge dislocations, we observed that

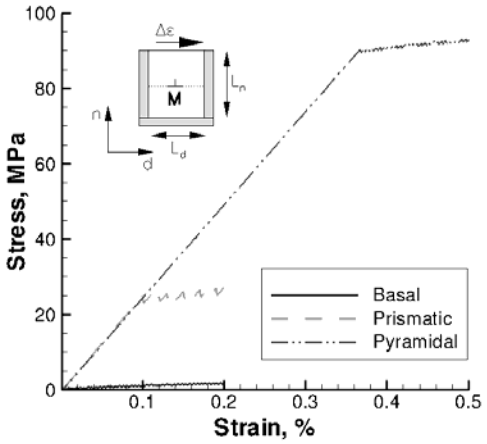

Figure 17. Strain-stress curves obtained by molecular static to model dislocation motion lying on the basal, prismatic, and pyramidal slip planes. ($\Delta\varepsilon = 10^{-5}$, L_n = 100b, and L_d = 100b).

before the dislocation moved, the stress increased linearly with the strain. The corresponding shear modulus was 12.6 GPa, which is in good agreement with the shear modulus reported by Sun et al. [4] (C_{44} = 12.8 GPa). The Peierls stress, which defines the minimum stress needed for moving a dislocation, was reached when the dislocation started to move without increasing the stress. A strong anisotropy between slip systems was observed (Table 2). The obtained Peierls stresses were in agreement with the nature of the dislocation core structures (i.e., a low Peierls stress for a dissociated core and a larger Peierls stress for an undissociated core) [5].

Table 2. Peierls stress (MPa) for basal, prismatic, and pyramidal slip systems in Magnesium calculated by molecular statics. (a: [6]; b: [7]; c: [8]; *numerical value.)

	Experimental data (MPa)	This study (MPa)	
		Liu et al. (1996)	Sun et al. (2006)
Basal 0.	52 (a)	14	0.35 ± 0.5
Prismatic 3	9.2 (b)	22	23.7 ± 0.5
Pyramidal 10	5* (c)	24	90–92

The Peierls stresses were not affected by a change of strain increment. Increasing the simulation cell size did not affect significantly the Peierls stress on the basal plane. On the other hand, increasing the cell size from 80b × 80b to 120b × 120b,

decreased the Peierls stress on the prismatic slip plane from 25.5 ± 1.5 MPa to 23.7 ± 0.5 MPa. The length of the edge dislocation lying in the prismatic plane (lengths ranging from one lattice period to thirty lattice periods were tested) did not affect its Peierls stress.

As reported in Table 2, the calculated Peierls stresses for each system are in a good agreement with experimental data. To determine the sensitivity of the Peierls stresses to the particular potential used, similar calculations were performed using the EAM potential proposed by Liu et al. [9]. Although the core structure for the edge dislocations was similar to the one reported above, the corresponding Peierls stresses (Table 2) were not in agreement with both the experimental data and the value calculated using the potential from [4].

Dislocation Mobility by Molecular Dynamics

MD simulations have been performed to determine the velocity of dislocations lying on the basal and prismatic slip planes. For comparison purposes, the velocities of edge/screw dislocations lying on these slip planes are plotted in Figure 18 as a function of the applied stress for a temperature of 100°K.

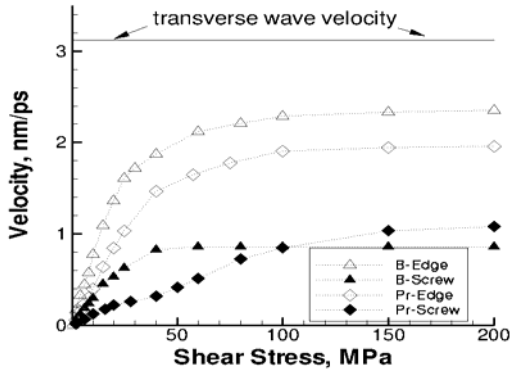

Figure 18. Dislocation velocity for edge and screw dislocations lying on the basal (B) and prismatic (Pr) slip planes.

Two types of anisotropy were observed: (1) anisotropy of the velocity related to the dislocation character and (2) anisotropy of the velocity related to the slip plane. Before the dislocation velocity saturates, the dislocation velocity increases linearly with the stress for a dislocation lying on either the basal or the prismatic slip planes. At 100°K, the drag coefficients are 4.7×10^{-6} Pa.s and 1.3×10^{-5} Pa.s for edge and screw dislocations on the basal slip plane, respectively, while 7.7×10^{-6} Pa.s and 3.7×10^{-5} Pa.s for edge and screw dislocations lying on the prismatic slip plane, respectively. In addition, as the Peierls barrier is higher in the prismatic than in the basal slip planes, the lower velocity for a dislocation lying in the prismatic plane compared to the velocity of a dislocation lying in the basal plane is the consequence of a stronger interaction between the dislocation and the Peierls barrier. For example, at 50 MPa, screw dislocations moved with a speed of 0.84 nm/ps and 0.41 nm/ps in the basal and prismatic slip planes, respectively, while edge dislocations moved with a speed of 2 nm/ps and 1.5 nm/ps in the basal and prismatic slip planes, respectively. Figure 19 shows two snapshots of the dislocation line under different conditions of loading. Figure 19a was obtained for an applied stress of 2 MPa at 100°K, while Figure 19b was obtained for an applied stress of 300 MPa at 500°K. Both configurations were extracted at the same time.

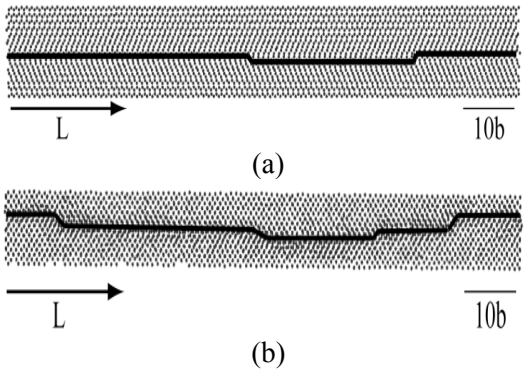

Figure 19. Projection on the (0001) plane of a screw dislocation lying on the basal plane after 1 ps. (a) 6 MPa, 100°K. (b) 300 MPa, 500°K.

Independent of the stress and temperature, the dislocation is moving by kink-pair mechanisms [5]. A portion of the line jumps to the next lattice position forming a pair of atomic-sized kinks. Driven by the stress, the kinks rapidly migrate along the dislocation line and recombine through the periodic boundary conditions. As a result, the entire dislocation translates to the next lattice

position. This mechanism explains generally the dislocation motion at low temperature when the applied stress is below the Peierls stress. However, although the Peierls stress in the basal plane is close to 0.3 MPa, the mechanism of motion by kink-pairs was still observed when the applied stress was above the Peierls stress.

Summary

In this work, we reported on the velocity of dislocation with <a> Burgers vector lying in either the basal, prismatic, or pyramidal slip plane, and calculated by either quasi-static calculations or MDs simulations. The effect of (1) the temperature and (2) the dislocation character on the dislocation mobility was investigated on each slip system. The Peierls stresses for edge and screw dislocations moving on either the basal, prismatic, or pyramidal slip plane were also determined, and a good agreement with experimental data from the literature was found.

From the dynamics calculations, we found a strong anisotropy of the dislocation velocity related to (1) the dislocation character and (2) the slip systems. In general, edge dislocations lying on the basal slip plane are moving two times faster than screw dislocations from the same slip system. On the other hand, edge dislocations lying on the prismatic slip plane are moving five times faster than screw dislocations gliding on the same slip plane. In addition, dislocations moving on the basal plane are two to three times faster (edge-screw) than dislocations from the prismatic slip system. The numerical dislocation velocities obtained during this study were correlated to a dislocation mobility rule following a viscous drag form, and the corresponding drag coefficients calculated at 100°K are reported in Table 3.

Table 3. Value of the drag coefficient (Pa.s) for edge/screw dislocations lying on the basal, prismatic, and pyramidal slip planes at 100°K

	Edge	Screw
Basal	4.7×10^{-6}	1.3×10^{-5}
Prismatic	7.7×10^{-6}	3.7×10^{-5}
Pyramidal	8.0×10^{-5}	Does not exist

Numerical Implementation of Deformation Twinning in a Crystal-Plasticity Model (MSST)

Mg single crystals and associated polycrystalline alloys are characterized by highly anisotropic mechanical behavior [10, 11, 12], with twinning being an important deformation mechanism at low temperatures. Hence, realistic modeling of Mg and its alloys requires accounting for deformation twinning in the constitutive equations. Over the last two decades, an extensive effort has been made to incorporate twinning deformation in polycrystalline modeling. The main assumption common to most models is to consider that a critical resolved shear stress exists to activate twinning, and therefore deformation twinning is considered as a polar pseudo-slip. Such an assumption is also considered in our development.

The aim of the work was to implement deformation twinning in an existing crystal plasticity framework. As a benchmark to validate the implementation, we applied the model to reproduce the anisotropic behavior of a Mg single crystal under plane-strain compression. The subsections below describe the implementation of deformation twinning in the crystal-plasticity framework and the numerical results obtained.

Modeling Framework

The crystal-plasticity framework developed in [13], where crystallographic slip is the only deformation mechanism, has been extended to account for deformation twinning. This development follows closely the work of [14]. This section presents solely the main aspects of the framework that need modifications to account for twinning.

The multiplicative decomposition of the local deformation gradient **F** can be written as the following (Figure 20):

$$\boldsymbol{F} = \boldsymbol{F}^e\boldsymbol{F}^p \text{ with } \boldsymbol{F}^e = \boldsymbol{V}^e\boldsymbol{R}^e \quad (1)$$

Here, $\boldsymbol{F}^e$ is the local elastic deformation gradient, decomposed in the elastic stretch, $\boldsymbol{V}^e$, and lattice rotation, $\boldsymbol{R}^e$, while $\boldsymbol{F}^p$ represents the local plastic deformation gradient due to both slip and deformation twinning.

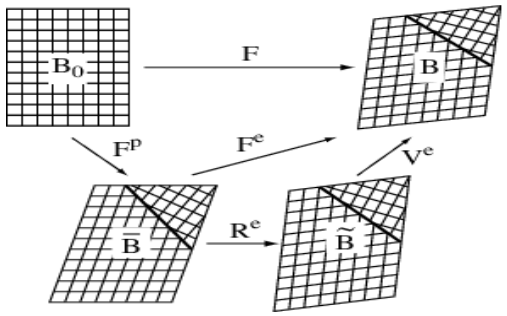

Figure 20. Kinematics of elastoplastic deformation of single crystals deforming by crystallographic slip and twinning.

In configuration $\bar{B}$, the plastic velocity gradient, $\bar{L}^{p}$, is written as the sum of the slip contribution in the nontwinned region and the twin contribution, and is given by

$$\bar{L}^{p} = \left(1 - \sum_{\beta}^{N^{tw}} f^{\beta}\right) \sum_{\alpha}^{N^{sl}} \dot{\gamma}^{\alpha} \bar{s}^{sl,\alpha} \otimes \bar{m}^{sl,\alpha} + \sum_{\alpha}^{N^{tw}} \delta \dot{f}^{\alpha} \gamma^{tw} \bar{s}^{tw,\alpha} \otimes \bar{m}^{tw,\alpha} \tag{2}$$

where $\dot{\gamma}^{\alpha}$ is the plastic shearing rate on the α-slip system which is defined by the unit vectors ($\bar{s}^{sl,\alpha}$, $\bar{m}^{sl,\alpha}$), $\dot{f}^{\alpha}$ is the rate of volume fraction of the α-twin system which is represented by the unit vectors ($\bar{s}^{tw,\alpha}$, $\bar{m}^{tw,\alpha}$), γ^{tw} is the constant shear strain associated with twinning, and δ is a material constant.

Note that Eq. (2) does not consider the slip system activity in the twinned region. This implies that the disorientation between the twin and the parent stays constant during the deformation. Also, this equation introduces the rate of the volume fraction on each α-twin system and the total volume fraction of twins in the formulation. The evolution equation of the twin volume fraction is represented by a power-law expression

$$\begin{cases} \dot{f}_v^{\alpha} = \dfrac{\dot{\gamma}_0}{\gamma^{tw}} \left(\dfrac{\tau^{\alpha}}{\kappa^{tw,\alpha}}\right)^{1/m} \text{ if } \left(\tau^{\alpha} > 0\right) \text{ and } \left(\sum_{\alpha} f_v^{\alpha} \le f_v^{sat}\right) \\ \dot{f}_v^{\alpha} = 0 \text{ if } \left(\tau^{\alpha} \le 0\right) \text{ or } \left(\sum_{\alpha} f_v^{\alpha} > f_v^{sat}\right) \end{cases} \tag{3}$$

where τ^{α} and $\kappa^{tw,\alpha}$ represent, respectively, the resolved shear stress on the α-twin system and the associated twin resistance. Note that the saturation of the twin volume fraction is controlled by the parameter f_v^{sat}. The hardening of the twin system is modeled by the expression

$$\kappa^{tw} = \kappa^{tw}{}_0 + h_{tw} \left(\sum_{i}^{N^{tw}} \frac{\dot{\gamma}^{i}}{\dot{\gamma}_{ref}}\right)^{d} \tag{4}$$

where $\kappa^{tw}{}_0$ is the twin critical resolve shear stress, $\dot{\gamma}_{ref}$ is a reference shear rate set up to 1 s^{-1}, and h_{tw} and d are material parameters.

Finally, slip-system hardening is modeled by an extended Palm-Voce rule [15] for each slip-system family: basal-<**a**>, prismatic-<**a**>, and pyramidal-<**c+a**>:

$$\dot{\kappa}_{sl}^{i} = h_{sl,s}^{i}(f) \left(\frac{\kappa_{sl,s}^{i}(f) - \kappa_{sl}^{i}}{\kappa_{sl,s}^{i}(f) - \kappa_{sl,0}^{i}}\right) \sum_{k}^{N^{sl,i}} |\dot{\gamma}^{k}| \tag{5}$$

$$\text{with} \quad \begin{cases} h_{sl,s}^{i}(f) = h_{sl,s0}^{i} \left(1 + C \sum_{\beta} f^{\beta}\right)^{b} \\ \kappa_{sl,s}^{i}(f) = \kappa_{sl,s0}^{i} + \kappa_{pr} \left(\sum_{\beta} f^{\beta}\right)^{0.5} \end{cases} \tag{5}$$

where $h_{sl,s0}^{i}$, $\kappa_{sl,0}^{i}$, $\kappa_{sl,s0}^{i}$ are material constants, and the parameters C, κ_{pr}, and b define the coupling between slip and twinning.

The developed framework has been implemented in both a material point simulator and an ABAQUS user material subroutine. These implementations have been used to determine the stress-strain behavior of Mg single crystals under plane- strain compression.

Numerical Results

Kelley and Hosford [12] have conducted deformation studies at RT on Mg single crystals. These crystals were oriented to suppress shear on the easily activated basal slip systems and were deformed by plane-strain compression. Table 4

Table 4. Direction of the compressive load and constraint for the plane-strain compression testing

Id	Compression	Constrain	Euler angle
A	< 0001 >	$< 10\bar{1}0 >$	(150, 0, 0)
B	< 0001 >	$< 1\bar{2}10 >$	(240, 0, 0)
C	$< 10\bar{1}0 >$	< 0001 >	(0, 90, 30)
D	$< 1\bar{2}10 >$	< 0001 >	(0, 90, –60)
E	$< 10\bar{1}0 >$	$< 1\bar{2}10 >$	(–90, 90, 30)
F	$< 1\bar{2}10 >$	$< 10\bar{1}0 >$	(90, 90, –60)

presents the six predefined orientations and the experimental results are given in Figure 21(a). Note that, for orientations E and F, twinning was observed at the beginning of the deformation to accommodate the compression perpendicular to the unconstrained **c**-axis. Once twinning was virtually completed, deformation continued by $\{10\bar{1}1\}$ banding.

Based on the analysis of the slip/twin activity for each orientation, the hardening parameters of the model were calibrated with the experimental data as follows.

- Orientation C gives the material parameters for the prismatic slip system.
- Orientation A gives the material parameters for the pyramidal slip system.
- Orientation E gives the materials parameters for the twinning activity.
- The coupling parameters between slip and twins, C, κ_{pr}, h_{tw}, b, and d were obtained using a parameter sensitivity study.

The computed stress-strain behaviors for the six orientations are given in Figure 21(b). Note that the trends observed in experiments are well predicted by the model.

Summary

In this work, an existent crystal-plasticity framework was extended to account for deformation twinning, where twins were considered as pseudo-dislocations. The framework was based on the multiplicative decomposition of the local deformation gradient. One of the main

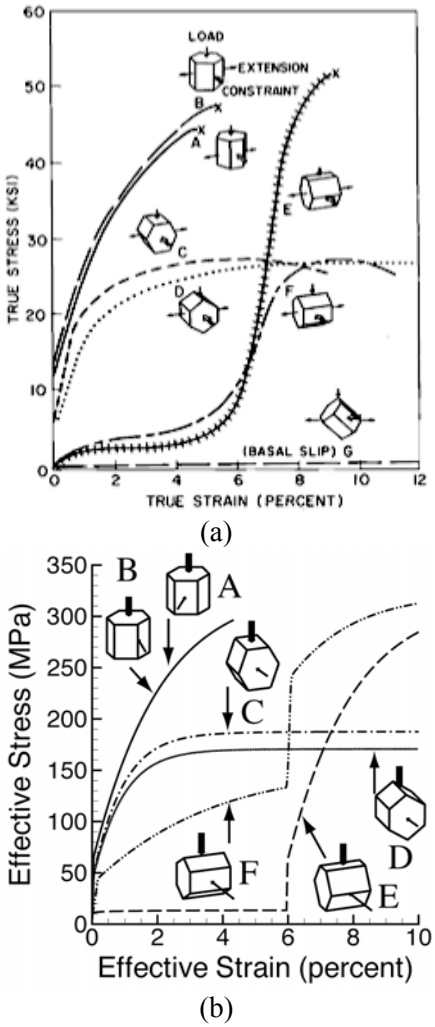

Figure 21. Stress vs strain in pure magnesium single crystal for the orientations given in Table 4: (a) experimental results [12] and (b) predictions from the model.

assumptions of this modeling approach is a constant orientation between the twinned region and the parent material. This assumption implies that no slip activity occurs in the twinned material. The model also assumes a power-law type for the evolution of the twin volume fractions and a constant hardening on both the slip and the twin systems.

The crystal-plasticity model was applied to predict stress-strain curves under plane-strain compression of Mg single crystals with six predefined orientations. Deformation twinning was only visible when the loading was applied perpendicularly to the unconstrained **c**-axis. The

predicted stress-strain curves agreed well with data from the open literature.

Recrystallization and Grain Growth Studies Using a Mesoscale Approach (ORNL)

The objective of these studies is to develop and validate mesoscale simulations of microstructure and texture evolution during TMP of Al- and Mg-alloy sheets, and to provide a comprehensive microstructure module that can be integrated with the ISV material model being developed by MSST for capturing the main features of microstructure evolution and corresponding history effects occurring during cold/hot working and heat treatment of Al and Mg alloys.

This work involves large-scale, crystal-plasticity modeling of microstructural deformation, extracting the deformation substructure, and evolving the substructure during annealing using a mesoscale technique that includes a nucleation model for recrystallization based on orientation-dependent recovery of subgrains.

Coupled Deformation-Recrystallization Simulations

TMP to produce optimum grain structure and texture is essential for the successful utilization of commercial Al and Mg alloys as sheet products. Several modeling techniques have been developed in the past with a reasonably good predictive capability for bulk deformation textures [16]. Significant progress has also been made in the last decade in the development of advanced measurement techniques for characterizing microtextures with high spatial resolution, both in two and three dimensions. However, prediction of microtexture evolution during deformation, and its subsequent evolution during recrystallization, remains very challenging because of uncertainties involved in predicting the mechanisms that lead to the formation of recrystallization nuclei with specific crystallographic orientations, and the uncertainties involved in predicting the grain/subgrain boundary properties that determine the growth kinetics of the nuclei. With the availability of large computers and advances in software, it is now possible to perform simulations of polycrystalline deformation with a high enough resolution to capture the formation of in-grain misorientations [17]. Mesoscale simulations of annealing have been combined with the output of deformation simulations to predict the evolution of recrystallization textures [18–21]. In these simulations, nucleation is modeled by heterogeneous subgrain growth, incorporating misorientation and structure-dependent boundary properties. A recent development in the modeling of nucleation is based on an assumption of orientation-dependent recovery of subgrains [22, 23]. Such an orientation-dependent recovery has been demonstrated in Al [24], copper [25] and steels [26, 27, 28]. It has also been shown that the cell morphology in the deformed structure is a function of the grain orientation. In the case of polycrystalline Al, it was shown that orientations in the vicinity of the cube had equiaxed cell structure while the other deformation orientations had a cell structure that had a linear morphology [29]. The orientation-dependent cell morphology was explained on the basis of the number of different noncoplanar active slip systems [29]. For example, a high number of noncoplanar active slip systems were correlated with more equiaxed cell morphology than when only a few coplanar slip systems are active during deformation. It has also been experimentally observed in Al polycrystals that orientations such as cube that have equiaxed cell structures also recover extremely fast compared to other deformation components.

Computational Approach

Microstructural Deformation: Mesoscale deformation simulations were performed using a polycrystal plasticity model incorporating neighboring grain interactions in which the applied deformation is distributed in a nonuniform fashion among the polycrystals [30]. Interactions with surrounding crystals are incorporated in the calculation of the deformation rate of each crystal through an appropriately defined local neighborhood. A compliance tensor is computed for each crystal based on a viscoplastic constitutive relation for deformation by crystallographic slip. The compliance of the crystal relative to that of its neighborhood provides a means for partitioning the macroscopic deformation rate among the crystals. The

deformation of fcc polycrystals under hot-rolling conditions was simulated using 18 slip systems, consisting of the 12 {111}<110> octahedral slip systems and the 6 {110}<110> nonoctahedral slip systems.

Recrystallization simulations were performed using a three-dimensional Monte Carlo approach on a cubic grid. For local-energy calculations, the energy of the site and a neighborhood consisting of the first, second, and third nearest neighbors was used. The input microstructure for the Monte Carlo simulations was obtained from the output of the crystal-plasticity simulations. The details of the Monte Carlo procedure are described elsewhere [18]. A combined simulation code that involves both deformation and recrystallization was developed for execution on parallel computers, in order to handle computational domains containing a large number of grains in the microstructure.

New Nucleation Model: A new model for the nucleation of recrystallized grains in fcc polycrystals was developed, based on the concept of "excess" hardening dislocations. The basic premise behind this approach is the existence of dislocations with mutually perpendicular Burgers vectors in fcc polycrystals. Interaction of these mutually perpendicular dislocations does not lead to hardening, since these dislocations remain mobile and do not form locks. The high mobility of the resulting special boundaries promotes rapid recovery of the dislocation substructure. Crystal orientations that have equal amounts of mutually perpendicular dislocations will recover very quickly to form recrystallized nuclei. While orientations with "excess" dislocations will form complex dislocation substructures that are slow to recover.

The nucleation step during recrystallization was modeled as follows. For each site in the simulation domain, the slip system deformation rate in the crystal coordinate system is calculated as

$$D_{ij}^{\alpha} = \dot{\gamma}_{\alpha} P_{ij}^{\alpha} \quad , \qquad (6)$$

where P_{ij}^{α} is the symmetric part of the Schmidt tensor and $\dot{\gamma}_{\alpha}$ is the shear rate on slip system α. Among the octahedral slip systems, those containing mutually- perpendicular Burgers vectors are identified, and "excess" dislocations are calculated by taking the absolute difference in slip system deformation rates on all such systems. A recovery factor is computed based on the sum of the "excess" dislocations over the entire deformation history, and a probability for nucleation is computed based on the recovery factor. An illustration of the distribution of slip system deformation rates in some of the commonly found orientations in rolled Al sheet is shown in Figures 22–24 for the D_{12}, D_{13} and D_{23} components, respectively. For cube orientation, the slip-system deformation rates are completely balanced, and can form high-mobility, low-energy boundaries contributing to quick recovery. On the other hand, for copper and S oriented grains, the slip-system deformation rates are not balanced, leading to "excess" dislocations that interact to form complex dislocation substructures and lead to slow recovery.

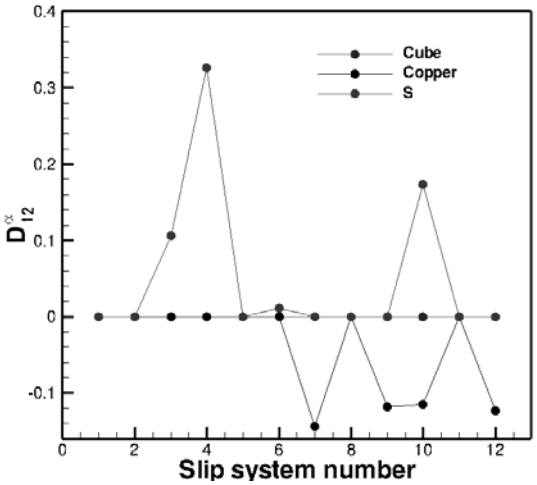

Figure 22. Distribution of deformation rate component D_{12} among various slip systems.

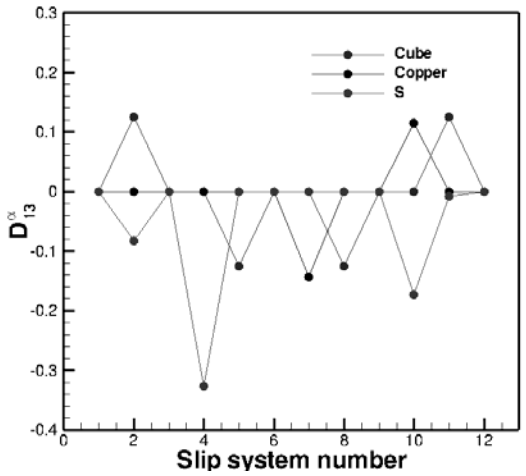

Figure 23. Distribution of deformation rate component D_{13} among various slip systems.

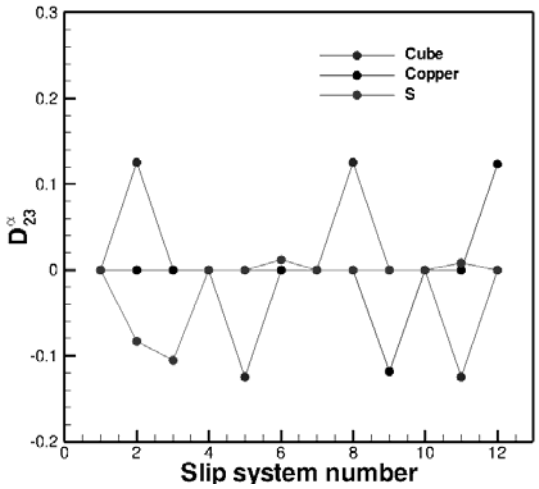

Figure 24. Distribution of deformation rate component D_{23} among various slip systems.

Results

The combined deformation and recrystallization model was used to simulate the deformation of an fcc polycrystal using a domain size of 180 × 180 × 180 sites. This problem was simulated on 216 processors. The input microstructure for the deformation model was obtained through grain growth, starting with a different orientation from a random distribution at each site. The grain-growth simulation was performed until the average grain size was about 8, which resulted in a microstructure with about 11,000 grains. The initial texture for this microstructure is shown in Figure 25 as a <111> pole figure.

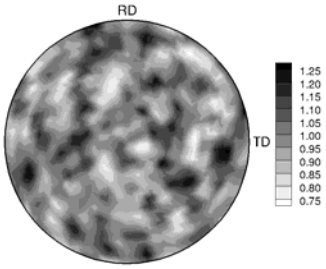

Figure 25. <111> pole figure showing the initial texture for the microstructure with about 11,000 grains.

The microstructure was deformed in plane-strain compression using the neighborhood compliance model described above under hot-rolling conditions to a compressive strain of –2.0 (about 86% reduction). The resulting deformation texture is shown as a <111> pole figure in Figure 26. The microstructure was then recrystallized, making use of the nucleation model discussed above. The result is a strong cube texture, as shown in Figure 27, even though Cube is not a major component in the deformed texture.

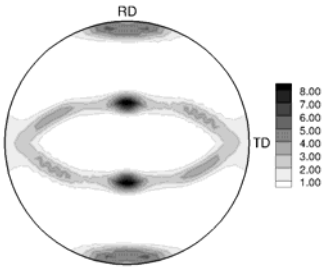

Figure 26. <111> pole figure showing the texture after deformation in plane-strain compression to 86% reduction.

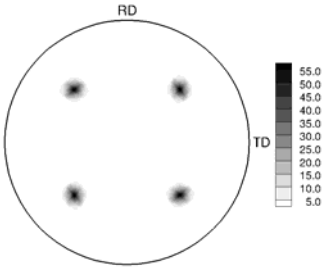

Figure 27. <111> pole figure showing the texture after recrystallization, indicating a strong cube component.

UMAT Subroutine for Magnesium Metals and Alloys (NWU)

Because of the light weight and ease of recycling, Mg alloys are of particular interest for automotive companies. However, due to the special material behaviors of these materials, few finite-element analysis implementations customized for magnesium constitutive law are available. Based on the existing theoretical work of orthotropic yield stress function by [31] and separate isotropic hardening law for tension and compression by [32], a numerical implementation procedure is proposed in this work. Our goal is to develop realistic finite-element simulations for modeling the behavior of magnesium alloys.

The proposed numerical implementation procedure consists of the following two phases: elastic and elastoplastic. In the elastic phase, a trial stress for a given discrete strain increment is evaluated assuming that the increment is elastic, while the equivalent plastic strain is kept as previous. If the effective stress given by the yield criterion is less than the yield stress calculated from the hardening law, the process is considered as elastic. Otherwise, the second phase is carried out. In the elastoplastic phase, a Newton-Raphson iteration method is used to solve the equivalent plastic strain increment, which allows effective stresses calculated separately from yield criterion and hardening law to be equal.

For verifying the numerical implementation procedure proposed above, a single shell element was created in the commercial FEM package ABAQUS and tested under uniaxial tension and compression in rolling and transverse directions using the developed user-defined material UMAT subroutine. As shown in Figure 28, the transverse direction exhibits higher yield strength than that in the rolling direction, which is consistent with the experimental data presented in [32]. Similar results are shown in Figure 29. If tension and compression results are compared, it can also be observed that the compression yield stress is less than the tension yield stress, which is a phenomenon observed from Mg alloys.

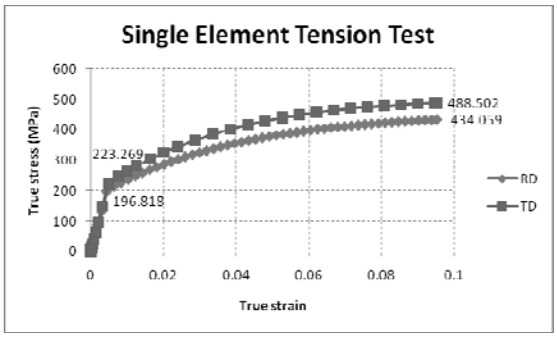

Figure 28. Stress-strain curve in uniaxial tension test.

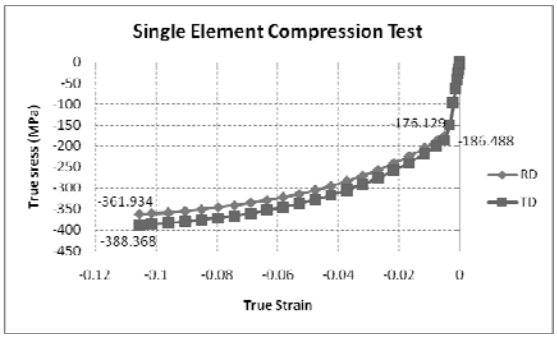

Figure 29. Stress-strain curve in uniaxial compression test.

Framework for Uncertainty Quantification and Reliability Based Design Optimization of Thermomechanical Processing

Statistical Volume Element Method for Predicting Microstructure-Constitutive Property Relations (NWU)

In materials design, there is an inevitable need to establish multilength scale statistical microstructure-constitutive property relations. In this research, we developed an SVE method to analyze, quantify, and calibrate such microstructure-constitutive property relations by statistical means. SVE simulations were adopted to predict material constitutive properties corresponding to various realizations of random microstructure configurations. As shown in Figure 30, a computing framework that links random configuration generators and finite-element analysis has been developed. A statistical cause-effect analysis approach was proposed to study the influence of random material microstructure on material constitutive properties.

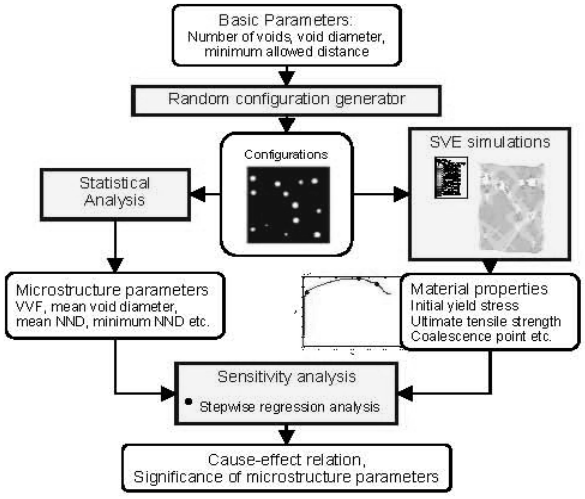

Figure 30. Statistical analysis study of material microstructure-constitutive property relation.

Within the proposed approach, statistically significant microstructure parameters are first identified based on their linear impacts on material constitutive properties. Global sensitivity analysis is then employed to provide a more comprehensive importance ranking of these critical microstructure parameters considering both main and interaction effects. The uncertainties in material constitutive properties due to random microstructure configurations are quantified in terms of distributions, statistical moments, and correlations, as shown in Figure 31. The obtained probabilistic constitutive relations are used to calibrate the model parameters in a constitutive relation model following a statistical calibration process. As shown in Figure 32, with the statistical calibration approach the obtained probabilistic constitutive relation can be reproduced through a calibrated Bammann-Chiesa-Johnson (BCJ) constitutive model.

Although our approach is currently demonstrated for a single-scale microstructure material model, our proposed techniques are generic enough to be applied to more sophisticated multiscale material models in either a hierarchical or a fully coupled (all-in-one) manner. The calibrated material constitutive models that incorporate the uncertainties propagated from random material microstructure will facilitate probabilistic analyses of material performance at the continuum level in

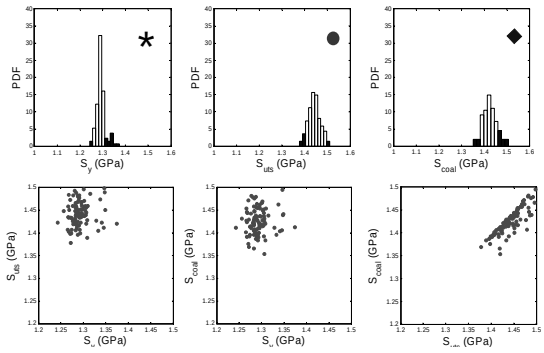

Figure 31. Distributions and correlation plots of stresses.

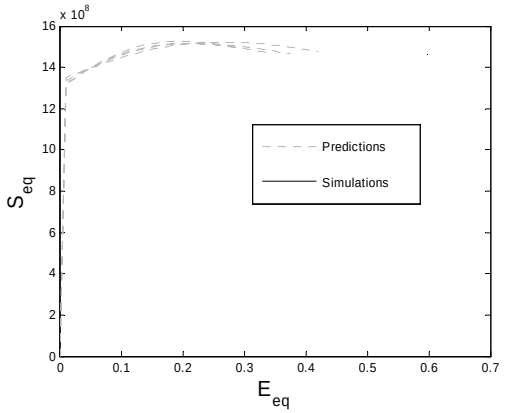

Figure 32. Random predictions/reproductions of the calibrated BCJ model compared to the SVE simulation results

multiscale design and analysis. Furthermore, the capability of deriving probabilistic material constitutive relations is essential in model validation process where the statistical computational results will be compared against random experimental results following the similar statistical model calibration procedure. The capability will also allow designers to assess the reliability of product performance by introducing the statistical representation of material constitutive relations.

A Multiscale Design Approach with Random Field Representation of Material Uncertainty (NWU)

To facilitate product design considering the impact of manufacturing process and material on product performance, a multiscale design approach is developed in our research with an emphasis on the treatment of material uncertainty across a product

domain as random field. By integrating manufacturing simulations, multiscale material models, and product models in a multiscale framework, the proposed approach allows either hierarchical or concurrent designs of manufacturing process, material and product in a multiscale content. A control-arm-design problem considering the spatial variation of initial porosity level due to casting process is used to demonstrate the applicability of the proposed approach.

For designing reliable products, uncertainty propagation under the proposed multiscale framework poses a significant computational challenge. An efficient procedure for uncertainty propagation from material random field to end product performance is developed (Figure 33). Material random field is discretized based on the product finite-element mesh and a reduced-order Karhunen-Loeve representation is derived from the covariance matrix of the discretized random field, which significantly reduces the dimensionality of random-field representation. The univariate dimension-reduction method and the Gaussian quadrature formula are applied to efficiently evaluate the statistical moments of the end-product performance.

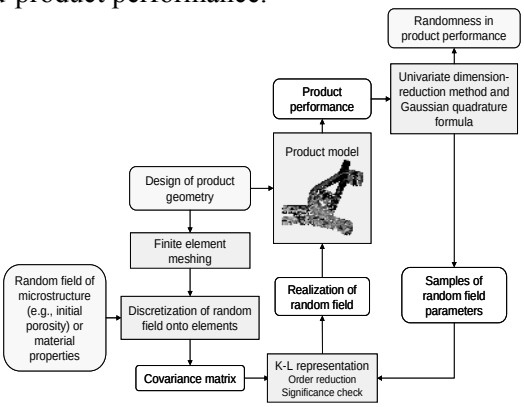

Figure 33. Efficient random field uncertainty propagation in design using multiscale analysis

The impact of a material microstructure random field with different correlation lengths on the statistical moments of product performance is studied. It is found that when the correlation parameter approaches infinity, the random field degenerates to a random variable which is uniform across the spatial domain. Based on the empirical study of the control-arm-design problem, it is discovered that the correlation parameter of input random field has a larger impact on the higher-order moments of product performance than on its mean value. Meanwhile, the correlation parameter has a monotonic negative effect on the mean product performance while a larger correlation length causes a greater standard deviation of the product performance.

A reliability-based design of the control arm is demonstrated with the consideration of uncertainty propagation across multiple scales from the material domain to the product domain. Reliable geometry designs of the control arm in terms of wall thicknesses are achieved to minimize the control-arm volume while keeping the damage level of the product under specified values. The control-arm-design example demonstrates the feasibility of the proposed approach with the random field representation of material uncertainty.

Robust Design with Arbitrary Distribution Using Gauss-Type Quadrature Formula

As a rigorous method of uncertainty propagation, the Gauss-type quadrature formula is investigated and applied to robust design formulated in terms of statistical moments of system performances. Due to the highest precision it provides, the Gauss-type quadrature formula is a well known method in the field of numerical integration. However, it has not been extensively used for uncertainty propagation involving various types of random variables. In this work, we developed a systematic procedure to find the nodes and weights of the Gauss-type quadrature formula for arbitrary input distributions and examined its mathematical meaning. It is shown that the nodes and weights of a m-node Gauss-type quadrature formula for a continuous random variable X are the samples and probability mass function of a discrete distribution, respectively, which is equivalent to X in terms of moments up to $2m-1$ order. Thus, those nodes and weights can be found from the moments of input random variables with various numerical approaches (Figure 34). Multidimensional quadrature formula can be built from the one-dimensional quadrature formula, and the tensor product formula and univariate dimension-reduction method are adopted in our work.

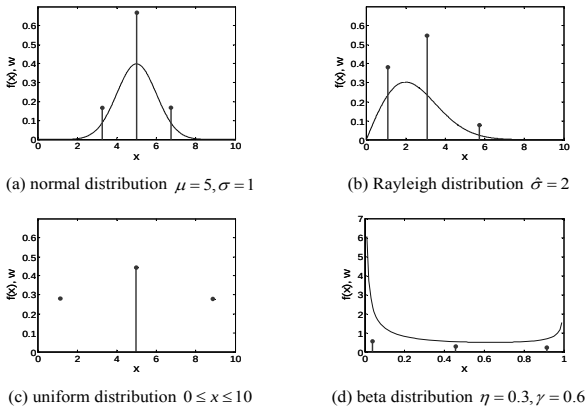

(a) normal distribution $\mu = 5, \sigma = 1$ (b) Rayleigh distribution $\hat{\sigma} = 2$

(c) uniform distribution $0 \le x \le 10$ (d) beta distribution $\eta = 0.3, \gamma = 0.6$

Figure 34. Nodes and weights in 3-node quadrature formulas for four different distributions. The vertical axis represents the values of probability distribution functions (PDF) and weights.

A procedure for robust design optimization using the Gauss-type quadrature formula is proposed with an emphasis on the efficient calculation of design sensitivity. Since one evaluation of statistical moments requires multiple function evaluations, the design sensitivity evaluation using approximate schemes such as finite-difference method will increase the computational cost of optimization significantly. In our research, formulas for semi-analytic design sensitivity of statistical moments are derived for tensor product and univariate dimension-reduction method, which utilize the sample data obtained during the moments estimation. It is shown from our case studies that the proposed design sensitivity analysis reduces the computational cost of robust design up to 40% when compared to the finite-difference method.

Conclusions

During 2008, the project has continued to make good progress on the activities planned. Also, new activities have been added to the work plan, in particular aspects related to the extrusion of Mg alloys. On the experimental part, the main focus has been on annealing studies to characterize recrystallization in Al and Mg alloys, uniaxial mechanical tests to study twinning effects in pure Mg, laboratory-scale experiments to learn about specific aspects of the extrusion process, and mechanical tests to capture the hardening behavior of sheet metals. On the material modeling part, the focus has been on MD simulations for mobility studies of hcp structures, enhancements of a crystal plasticity model to model deformation twinning, and developing a new nucleation model for recrystallization of fcc crystal structures using Monte Carlo techniques. Finally, on the design/optimization part, a probabilistic framework with its numerical aspects has been developed to quantify/propagate uncertainties due to different sources when designing/optimizing deformation processes. All this work will contribute to the development of robust TMP models and design methodologies for improving manufacturability and forming technology of lightweight materials, in particular, Al and Mg alloys.

Presentations/Publications/Patents

1. S. Groh, E. B. Marin, M. F. Horstemeyer, and H. Zbib (2008), "Multiscale Modeling of the Plasticity in Aluminum Single Crystal," *International Journal of Plasticity*, in press.
2. S. Groh, E. B. Marin, D. J. Bammann, and M. F. Horstemeyer, "Implementation of Deformation Twinning in a Crystal Plasticity Code: Application to Mg Single Crystal," CAVS internal report, under review.
3. J. Cao, W. Lee, H. S. Cheng, H. Wang, and K. Chung (2008), "Experimental and Numerical Investigation of Combined Isotropic-kinematic Hardening Behavior," to appear International *Journal of Plasticity*. doi:10.1016/j.ijplas.2008.04.007.
4. X. Yin, W. Chen, W. K. Liu, and A. To, "A Statistical Volume Element Method for Predicting Microstructure Constitutive Relations," *Computer Methods in Applied Mechanics and Engineering*, available online, January 2008.
5. X. Yin, S. Lee, W. Chen, W. K. Liu, and M. F. Horstemeyer, "A Multiscale Design Approach with Random Field Representation of Material Uncertainty," Paper No. DETC2008-49560, Proceedings of the ASME 2008 International Design Engineering Technical Conferences & Computers and Information in Engineering Conference, August 3–6, 2008, Brooklyn, New York. In press, *ASME Journal of Mechanical Design*.

6. S. Lee, W. Chen, and B. M. Kwak, "Robust Design with Arbitrary Distributions using Gauss-type Quadrature Formula," Proceedings of the 12th AIAA/ISSMO Multidisciplinary Analysis and Optimization Conference, September 10–12, 2008, Victoria, British Columbia, Canada, in press, Structural and Multidisciplinary Optimization.

References

1. [Mordike, 2001] B. L. Mordike, and T. Ebert, "Magnesium—Properties—applications—potential," *Materials Science and Engineering A*, 12 (2001) 37–45.
2. [Groh, 2008] Groh, S., Marin, E. B., Horstemeyer, M. F., and Zbib, H. M., 2008. *Int. J. Plast.,* in print.
3. [Plimpton, 1995] Plimpton, S. J., 1995. *J. Comp. Phys.* 117, 1–19.
4. [Sun, 2006] Sun, S. L., Mendelev, M. I., Becker, C. A., Kudin, K., Haxhimali, T., Asta, M., Hoyt, J. J., Karma, A., and Srolovitz, D. J., 2006. *Phys. Rev. B.,* 73, 024116-1-12.
5. [Hirth and Lothe, 1992] Hirth, J. P., and Lothe, J., *Theory of dislocations*, Krieger Publishing Company, Malabar, Florida.
6. [Conrad, 1957] Conrad, H., and Robertson, W. D., *AIME* 209 (1957) 503.
7. [Reed-Hill, 1957] Reed-Hill, R. E., and Robertson, W. D., 1957. *Acta Metall.,* 5, 717–727.
8. [Staroselsky, 2003] Staroselsky, A., and Anand, L., 2003. *Int. J. Plasticity.* 19, 1843–1864.
9. [Liu, 1996] X.-Y. Liu, J. B. Adams, F. Ercolessi, and J. A. Moriarty, *Modelling. Simul. Mater. Sci. Eng.* 4 (1996) 293–303.
10. [Kelley, 1968] Kelley, E. W., and Hosford, Jr., W. F., 1968. Trans. Metal. Soc. *AIME*, 242, 5–13.
11. [Kelley, 1968] Kelley, E. W., and Hosford, Jr., W. F., 1968. Trans. Metal. Soc. *AIME*, 242, 5–13.
12. [Kelley, 1968] Kelley, E. W., and Hosford, Jr., W. F., 1968. Trans. Metal. Soc. *AIME,* 242, 5–13.
13. [Marin, 2006] Marin, E. B., 2006 Sandia National Laboratories, CA, SAND2006-4170.
14. [Kalidindi, 1998] Kalidindi, S. R., 1998. *J. Mech. Phys. Solids.* 46, 267–271.
15. [Kelley, 1968] Kelley, E. W., and Hosford, Jr., W. F., 1968. *Trans. Metal. Soc. AIME*, 242, 5–13.
16. [Nave, 2004] Nave, M. D., and Barnett, M. R., 2004. *Scripta Mater.,* 51, 881–885.
17. [Barnett, 2007] M. R. Barnett, *Mat. Sc. Eng.* A, 464 (2007) 1–7.
18. [Salem, 2005] Salem, A. A., Kalidindi, S. R., and Semiatin, S. L., 2005. *Acta Mater.* 53, 3495–3502.
19. [Kocks, 1998] U. F. Kocks, C. N. Tomé, and H.-R. Wenk, *Texture and Anisotropy,* Cambridge University Press, Cambridge, 1998.
20. [Sarma, 1998] G. B. Sarma, B. Radhakrishnan, and T. Zacharia, Comput. *Mater. Sci.* 12 (1998) 105–123.
21. [Radhakrishnan, 1998] B. Radhakrishnan, G. Sarma, and T. Zacharia, *Acta Mater.* 46 (1998) 4415–4433.
22. [Radhakrishnan, 2000] B. Radhakrishnan, G. Sarma, H. Weiland, and P. Baggethun, *Model. Simul. Mater. Sci. Eng.* 8 (2000) 737–750.
23. [Radhakrishnan, 2004A] B. Radhakrishnan, G. Sarma, *Phil. Mag.* A22 (2004) 2341–2366.
24. [Radhakrishnan, 2004B] B. Radhakrishnan, G. Sarma, JOM 56 (2004) 55–62.
25. [Crumbach, 2004] M. Crumbach, M. Goerdeler, G. Gottstein, L. Neumann, H. Aretz, and R. Kopp, *Model. Simul. Mater. Sci. Eng.* 12 (2004) S1–S18.
26. [Radhakrishnan] B. Radhakrishnan and G. Sarma, *Mater. Sci. Eng.* A494 (2008) 73–79.
27. [Theyssier, 1999] M. C. Theyssier and J. H. Driver, *Mater. Sci. Eng.* A272 (1999) 73–82.

28. [Ridha, 1982] A. A. Ridha and W. B. Hutchinson, *Acta Metall. Mater.* 30 (1982) 1929–1939.

29. [Humphreys, 1995] F. J. Humphreys, M. Hatherly, *Recrystallization and Related Annealing Phenomena,* first ed., Elsevier, New York, 1995, pp. 335–337.

30. [Barnett, 1999] M. R. Barnett and L. Kastens, ISIJ International 39 (1999) 923–929.

31. [Yoshinaga, 1998] N. Yoshinaga, D. Vanderschueren, L. Kestens, K. Ushioda, and J. Dilewijns, *ISIJ International* 38 (1998) 610–616.

32. [Liu, 1998] Q. Liu, D. Juul Jensen, and N. Hansen, *Acta Mater.* 46 (1998) 5819–5838.

33. [Sarma, 1996] G. Sarma and P. R. Dawson, Int. J. Plast. 12 (1996) 1023-1054.

34. [Cazacu, 2005] Cazacu, O., Plunkett, B., and Barlat, F., "Orthotropic yield criterion for hexagonal closed packed metals," *Int. J. Plasticity*, 2005.

35. [Kim, 2008] Kim, J., Ryou, H., Kim, D., Kim, D., Lee, W., Hong, S. H., and Chung, K., "Constitutive Law for AZ31B Mg Alloy Sheets and Finite Element Simulation for Three Point Bending," 2008.

B. Development of High-Volume Warm Forming of Low-Cost Magnesium Sheet (AMD602*)

Principal Investigator: Peter Friedman
Ford Motor Company
Ford Research and Innovation Center
2101 Village Road, MD 3135
Dearborn, MI 48121-2053
313-248-3362; fax: 313-390-0514; e-mail: pfriedma@ford.com

Principal Investigator: Paul Krajewski
General Motors Corporation
General Motors R&D and Planning
Mail Code 480-106-212
30500 Mound Road
Warren, MI 48090-9055
586-986-8696; fax: 586-986-9204; e-mail: paul.e.krajewski@gm.com

Principal Investigator: Jugraj Singh
Chrysler Corporation LLC
Body Materials Engineering
Mail Code 482-00-11
800 Chrysler Drive
Auburn Hills, MI 48326-2757
(248) 512-0029; fax: (248)576-7490; e-mail: js329@chrysler.com

Technology Area Development Manager: Joseph A. Carpenter
(202) 586-1022; fax: (202) 586-1600; e-mail: joseph.carpenter@ee.doe.gov

Field Project Officer: Aaron D. Yocum
(304) 285-4852; fax: (304) 285-4403; e-mail: aaron.yocum@netl.doe.gov

---

Contractor: United States Automotive Materials Partnership
Contract No.: FC26-020R22910 through the DOE National Energy Technology Laboratory

---

Objective

Develop the technology and material supply base for cost-effective lightweight body panels fabricated from sheet magnesium (Mg). A warm-forming system will be designed and built to develop a suitable process for forming Mg sheet as well as a test bed to evaluate potential low-cost Mg sheet from various global producers. Specific deliverables from this project will include the following:

- Design and build a warm-forming die and demonstrate a deep-draw capability on conventional direct chill (DC) material.
  - — Demonstrate pan forming of at least 100 mm.
- Evaluate materials and compare the formability of continuous cast (CC) and DC materials.
  - — Evaluate high-temperature elongation, which is equal or greater in CC material compared to DC material.

*Denotes project 602 of the Automotive Materials Division of the United States Automotive Materials Partnership, one of the formal consortia of the United States Council for Automotive Research set up by Chrysler, Ford, and General Motors to conduct joint, precompetitive research and development (see www.uscar.org).

- Demonstrate high-volume cycle times with CC material on an integrated forming cell.
  - Part-to-part cycle time with CC material of 5–10 jobs per minute (jpm).

Approach

Continuous casting is a key technology for enabling the development of low-cost Mg sheet. This project will drive material development in the supply base by giving them a mechanism for evaluating materials. The project will receive material from major global Mg suppliers including Magnesium Elektron, CSIRO, ThyssenKrupp, LY Copper, and POSCO. These materials will be characterized via tensile testing at the University of Virginia, biaxial forming at Canada Centre for Mineral & Energy Technology (CANMET), and through stamping trials at Troy Tooling Technologies.

- Novel die systems will be designed and constructed that enable the use of warm forming in conventional single-action presses. The die will be used to determine critical forming parameters for Mg sheet, including lubricant thickness, preheat temperature, die temperature, forming speed, etc. The forming windows for the different materials will be determined to see the effect of processing via different methods, e.g., CC vs ingot (DC) casting.
- Full automation including loading of pre-heated sheet and part extraction will be developed to achieve acceptable cycle times (5–10 jpm) demonstrating the high-volume feasibility of warm forming.

Accomplishments

- Completed the material characterization work through microscopy, elevated temperature tensile testing and formability experiments on alloys from four suppliers.
- Demonstrated the formability of the CC alloys with both tensile testing, lab-scale formability experiments, and full warm-forming trials. Developed forming-limit curves at CANMET for all test alloys at two different temperatures.
- Completed first full-scale forming trial and determined a forming window for Mg sheet with respect to temperature, binder pressure, lubricant, and blank size.
- Developed a strategic approach to automating the warm-forming system based on existing equipment donated to the project from General Motors (sheet pre-heater) and Ford (robot).
- Established the feasibility of using a new, lower-cost synthetic oil lubricant for forming at temperatures up to 275°C.

Future Direction

- Forming trials on newer materials.
- Post-form analysis
- Develop automated system to pre-heat sheets and deliver them to the die to support the goal of 5 to 10 parts per minute.
- Full-scale trials on automated system

Introduction

The major barrier to the application of Mg sheet components in vehicle structures is a combination of two factors: the limited formability of Mg sheet and the cost of producing the sheet itself. Warm-forming processes similar to what was demonstrated in aluminum with the USAMP Warm Forming Project (AMD 307) can be used to significantly improve the formability of Mg sheet. This project is leveraging the accomplishments of AMD 307 to develop equipment, lubricant, simulation and forming equipment for the cost-effective forming of Mg sheet. A warm-forming cell based on the lessons learned of AMD 307 will be designed and built to demonstrate the efficient forming of Mg sheet. The target application for this process is deep-draw panels with specific interest in door inners.

The cost of Mg sheet is driven by the high conversion costs of rolling an ingot into sheet form. This is a direct result of the hexagonal close-packed (HCP) structure of Mg that requires the sheet to be rolled in small increments often with annealing steps between rolling passes. CC is a technology with the potential to reduce this cost dramatically. By casting directly into sheet form, CC offers a higher production rate, a smaller capital investment, and significantly less energy and labor as compared with the conventional DC ingot-casting process. The opportunities for decreasing the cost of Mg sheet via continuous casting have been described by Hunt et al. in their 2005 report to the DOE. Suppliers globally are working on developing CC technology. In this project, all of the major global Mg suppliers will be included to determine if their materials are suitable for the warm-forming process. The new warm-forming system will be used as a standard test bed for the evaluation of these materials as well as new Mg sheet materials produced in the future.

Low-Cost Magnesium Sheet

The project includes Mg sheet from five major global Mg suppliers. This includes two DC casters (Magnesium Elektron and ThyssenKrupp) and three continuous casters (CSIRO, LY Copper, and POSCO). Four suppliers have provided 100 blanks of 1 mm × 600 mm × 600 mm of AZ31B-O material. All of the materials will be used at three locations, The University of Virginia, CANMET, and Troy Tooling Technologies.

Materials in this work have been coded so that the technical results can be shared with all the material suppliers without providing company information. Samples of all the materials have been provided to Professor Sean Agnew at the University of Virginia and Dr. Kevin Boyle at CANMET.

Deliverable:

- Determine best AZ31 alloy for warm forming and provide guidance to the materials community on how CC materials compare with DC cast materials.

Material Characterization

The University of Virginia

In this work, the microstructure and tensile properties of four different materials of nominally the same composition but produced by distinct processing routes were characterized. While such comparative studies are often conducted in a blind or double-blind fashion in the biological, medical, and social sciences, it is rather atypical to do so within the field of metallurgy. The experimentalists in this study were unaware of the processing route, and as such were able to probe the fundamental microstructure–property relationships without any bias associated with knowledge of the processing history.

Experimental Procedures

Four heats of Mg alloy, AZ31B, sheet were examined in this study. Each of the sheets was received in the O temper (fully annealed) with a nominal thickness of 1 mm and a length and width of approximately 600 mm whose compositions are presented in Table 1. Some of the alloys were produced by strip casting and warm/cold rolling to the finish gage and some were DC cast as thick slabs, hot rolled, and finally warm/cold rolled to finish gage.

Table 1. Sample designations and compositions

Sheet	Al	Zn	Mn	Mg
M	2.6	0.71	0.32	Balance
N	3.0	0.74	0.35	Balance
O	3.0	0.74	0.32	Balance
X	2.9	0.95	0.53	Balance

The microstructures of the sheets were analyzed using optical and scanning electron microscopy. Standard metallographic sample preparation was employed, with a requirement that oil-based lubrication be used (rather than water) for all polishing steps. An acetal-picric etchant was used which revealed grains and grain boundaries. The average grain size was determined using a computer-aided linear intercept measurement.

Texture measurements were performed on the sheet surfaces and midplanes. A Scintag X1 X-ray diffractometer equipped with a CuK_{α} sealed tube source, energy-dispersive detector and a 4-circle

goniometer was employed to measure pole figures to a sample tilt of 80°. The (00.2), (10.0), and (10.1) pole figures were measured and the preferred orientation package of Los Alamos (popLA) software was used to calculate the complete orientation distribution which, in turn, allowed the recalculation and presentation of complete pole figures. Standard X-ray powder diffraction was also used to determine the phase content.

An Instron universal testing machine, equipped with a clam-shell cylindrical furnace, was used for tensile testing over a range of temperatures, from room temperature to 350°C, and a range of constant true strain rates, from 5×10^{-5} to 1 s^{-1}. Samples were tested with the stress axis aligned with two orthogonal directions: the rolling direction (RD) and the transverse direction (TD). The sample geometry was a compromise between the American Society for Testing and Materials (ASTM) standard for the characterization of sheet superplasticity [1] and a similar sample developed at General Motors (GM) Research and Development Center. The sample has a straight gage length of 32 mm, sharp radius of 1.25 mm, and large grip tabs. The sample is pulled by the grip shoulders, which enables quick loading, to avoid large temperature transients in the furnace, and quick unloading which allows rapid quenching following testing. A small number of tests were conducted in an MTS screw-driven testing machine within an ATS convection furnace, which is capable of sustaining more uniform temperature distribution, even at large deformations. Finally, because sheet-metal formability can be influenced by strain anisotropy, the Lankford coefficient r was calculated as

$$r = \varepsilon_w / \varepsilon_t \quad , \qquad (1)$$

where ε is the logarithmic true plastic strain along the sample width *w* and thickness *t*. The variation in *r* was determined as a function of strain at specific temperatures and strain rates relevant to warm forming.

Results and Discussion

Typical optical sections of the sheets, looking along the rolling direction, are shown in Figure 1.

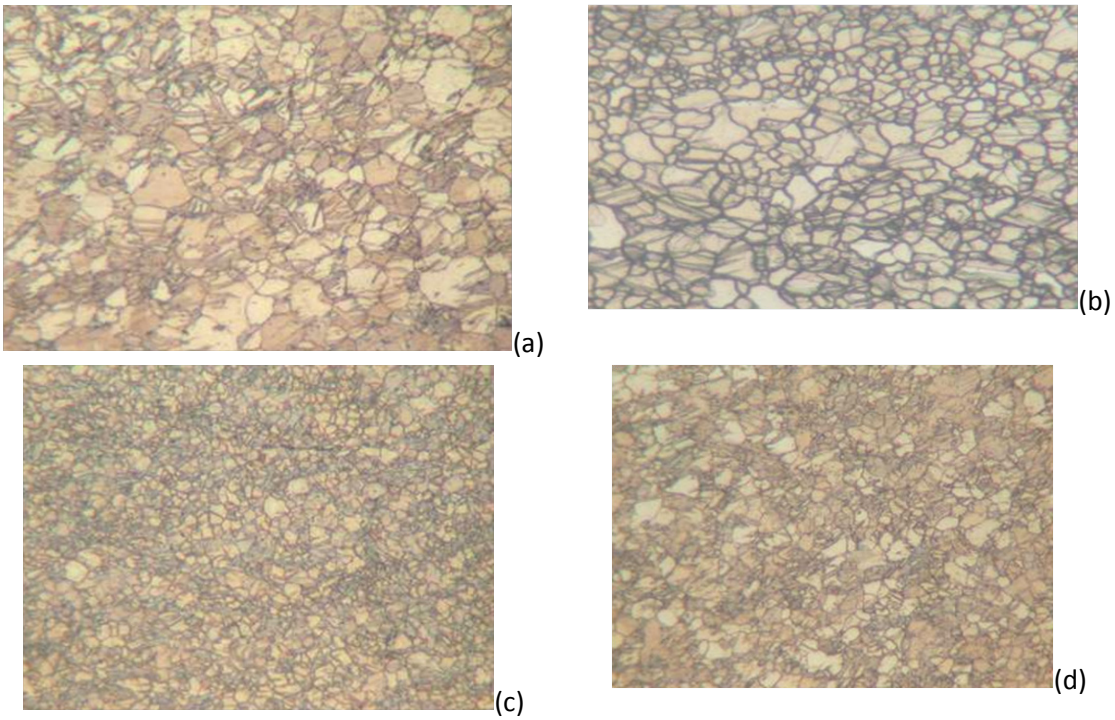

Figure 1. Optical micrographs (at right) illustrate the similarities and distinctions among the four alloys (a) M, (b) N, (c) O, and (d) X.

The grain sizes were measured using the Heyn intercept method, as described by Vander Voort [2] with measurements obtained using lines oriented parallel to the three orthogonal axes, RD, TD, and the normal direction (ND). Measurements were made on faces perpendicular to each of the three orthogonal directions. The results show that all of the sheets, without respect for the gross differences in processing history, acquired equiaxed microstructures (Table 2.), with the presence of twins more obvious in the samples with coarser grain sizes. A summary of the data is contained in Tables 2 and 3. It was found that sample M had the coarsest average grain size, samples N and X were very similar, and sample O had the finest grain sizes.

Table 2. Linear intercept grain size (in μm) measured along various directions and the corresponding aspect ratios

Sheet	d_{RD}	d_{TD}	d_{ND}	RD/TD	RD/ND	TD/ND
M	11.1	12.2	10.1	0.91	1.10	1.20
N	8.3	8.1	8.0	1.03	1.04	1.01
O	5.8	6.2	5.6	0.93	1.04	1.11
X	8.0	8.8	8.2	0.92	0.98	1.06

Table 3. Overall grain size (again in μm, and assumed equiaxed) and statistics, including standard deviation of the mean (**Σ)**, 95% confidence interval, and %-relative accuracy (RA)

Sheet	d_{avg}	Σ	95%	% RA
M	11.0	0.4	0.9	8.4
N	8.2	0.2	0.3	4.6
O	5.8	0.1	0.3	5.3
X	8.3	0.1	0.3	3.8

Additionally, while all the alloys did contain second phase particles, most notable are the large (~10 μm) particles within sheet X. Figure 2 is an SEM micrograph of a typical cracked particle. Energy-dispersive X-ray spectra (EDS) were collected to determine their chemistry. On average, the precipitates contain approximately 80% Mn, 8% Al, 5% Fe and 0–2% Mg, Na, Cr, O, Si, Cl. The presence of Fe is not surprising given that one role of the Mn additions is to scavenge such transition metal impurities.

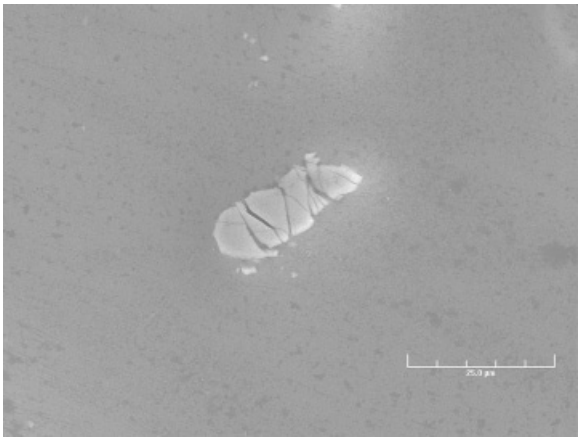

Figure 2. Scanning electron microscope image of a typical large particle in sheet X.

X-ray powder diffraction was used to determine the phase of these particles. Given that the volume fraction of second-phase particles is low, the only phase that could be unquestionably identified using initial XRD scans of monolithic samples was the α-Mg phase. Different chemical methods were explored which would digest the Mg phase, and enhance the signal from the particles. An aggressive etch of the surface, which exposed a larger fraction of particles, proved successful in confirming that the particles are the α-Mn phase. The presence of large Mn particles is consistent with the fact that sheet X had the highest Mn content. Although space precludes presentation of the images, metallography of tensile-tested samples has demonstrated that these particles initiate cavities, although this does not result in an overall lowering of the ductility with respect to the sheets which have smaller particles.

Texture:

Recalculated (00.1)- and (10.0)-pole figures are presented in Figure 3 showing that all of the sheets have a basal texture characteristic of Mg alloy AZ31B sheet, regardless of whether they were processed by DC casting and heavy reduction by hot rolling or by strip casting. This suggests that the texture is most heavily influenced by the final warm/cold reduction and annealing steps. Only the mid-plane textures are presented, since they are characteristic, although the texture was measured at the surface-, 1/8-, 1/4-, 3/8-, and mid-thickness planes of each sheet. There is no significant gradient in the texture between the 1/8- and mid-planes. Rather, the gradients are restricted to the

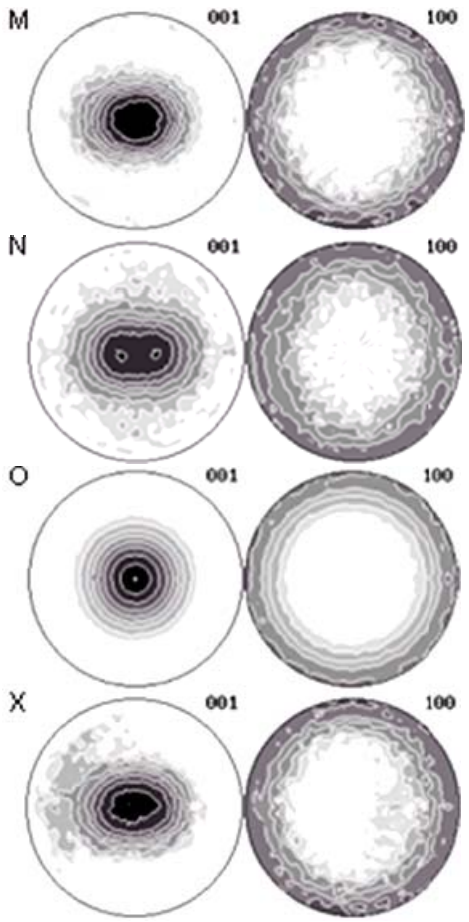

Figure 3. Textures of the 4 alloy sheets measured at the mid-plane (RD to the right, ND normal to the page, and intensity contours on a log scale: 0.21, 0.35, 0.50, 1.0, 1.7, 2.8, 4.8, 8.0).

near-surface region, which is influenced most heavily by the shear stresses imposed by contact with the rolls.

Only sheet N shows the splitting of the basal pole intensity toward the rolling direction, which is characteristic of Mg alloy AZ31B sheet in the H24 temper (e.g., [3]). Although the O temper was specified for each of the sheets, it appears that a larger volume fraction of material retained the deformation texture components in this sheet than in the others. The other sheets show a surprising level of radial symmetry about the sheet ND, which is characteristic of sheets with the O temper [4], and presumably characteristic of the recrystallization texture. Curiously, the mechanical properties (strengths) of sheet N are not distinct, although it will be shown that the Lankford coefficient, r, does show a stronger in-plane variation in this alloy than the others.

Mechanical Properties:

Figures 4 and 5 show representative flow curves out of ~235 tests performed over the temperature and rate regime of interest. None of the alloys exhibit significant strength anisotropy. Thus, only data from RD samples are presented in order to avoid cluttering the plots. In general, the four alloy sheets behave quite similar to one another, in terms of flow strength, strain hardening, and ductility.

As reported previously by Jiang et al. [5] and the present group [6], wrought Mg alloys undergo a plateau or even a decrease in ductility with increasing temperature within the temperature range examined. Note the decrease in flow stress *and ductility* as the temperature is increased from 150 to 200°C [e.g., Figure 4(a)]. This anomaly also occurs with respect to strain rate, whereby the ductility can decrease with decreasing strain rate [e.g., Figure 5(b)]. These anomalies can be predicted using a continuum mechanical model of plastic instability, if one accounts for the simultaneous changes in strain and strain rate hardening behaviour [6], and it has been mechanistically ascribed to incomplete (heterogeneous) dynamic recrystallization, which occurs within the same rate and temperature regime [5].

Figure 6 shows multiple engineering stress vs strain curves obtained from samples of each sheet at a temperature of 300°C and a strain rate of 0.005 s^{-1} within a convection furnace that ensures a uniform temperature distribution, even at large elongations. This presentation emphasizes the similarity of the flow curves, e.g., each have a "knee" in their flow curve at about 50% elongation, and exhibit plastic instability at a low strain, which means that most of the elongation is "post-uniform" and due to the finite rate sensitivity of the alloys. It is observed that the three curves with the highest peak stresses are from sheet M, which has the largest grain size, and the curves with the lowest peak stress are from sheet O, with the finest grain size.

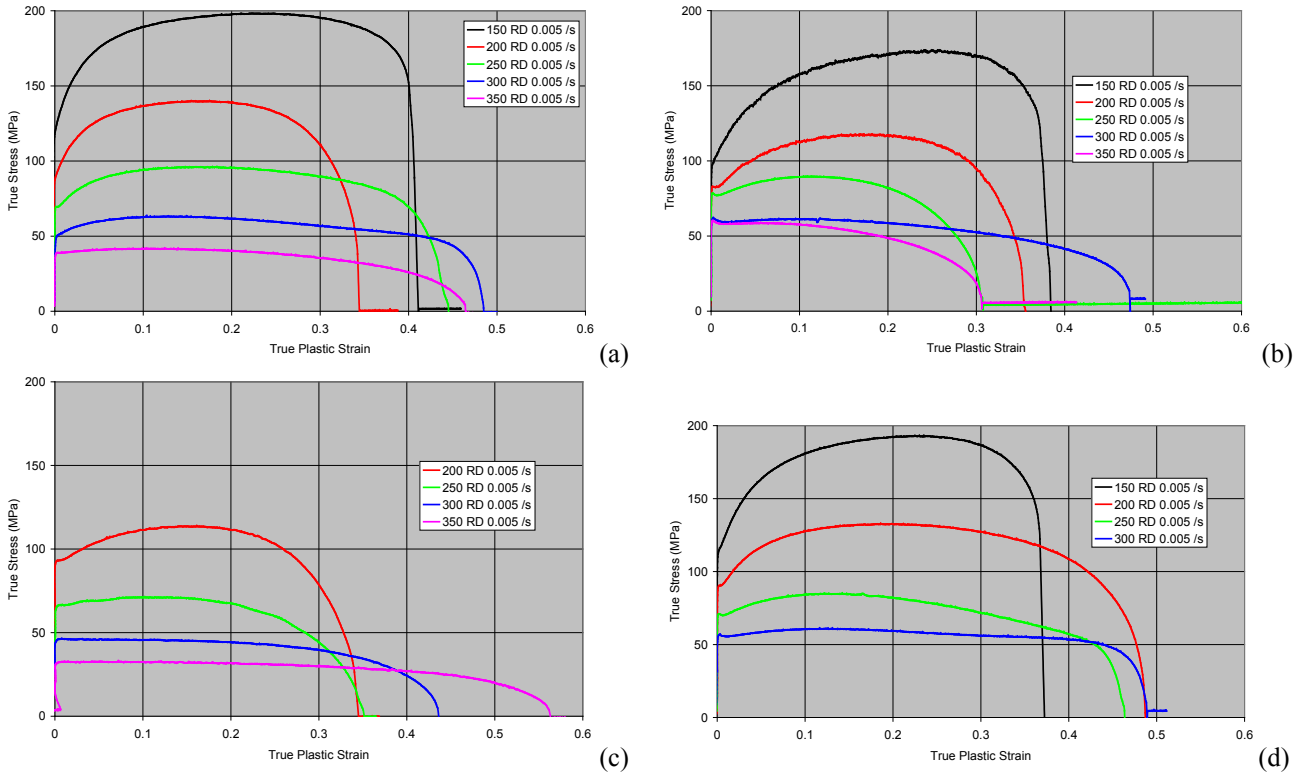

Figure 4. Temperature dependence of the RD tensile flow curves of sheets a) M, b) N, c) O, and d) X at a constant true strain rate of $.5 \times 10^{-3}$ s^{-1}.

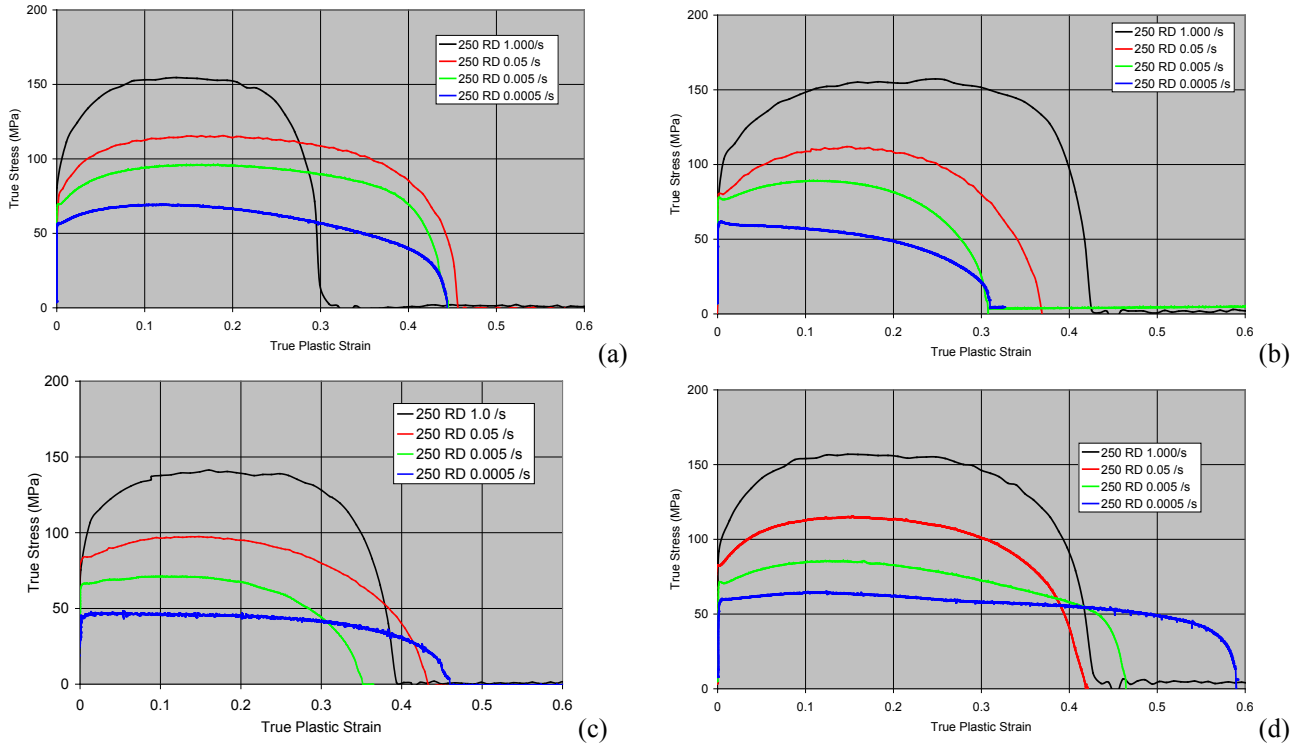

Figure 5. Strain-rate dependence of the RD flow curves of sheets (a) M, (b) N, (c) O, and (d) X at a temperature of 250°C.

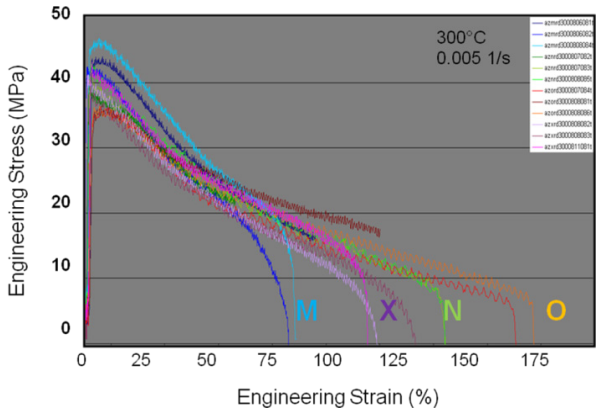

Figure 6. Engineering stress vs engineering strain at a temperature of 300°C and strain rate of 5×10^{-3} s^{-1}.

Samples of sheets N and X exhibit intermediate flow strengths in keeping with their intermediate grain sizes. At this temperature, finer grains promote easier flow and higher strain-rate sensitivity. This helps explain why samples of sheet O have the highest elongation to failure, and M samples the lowest, at this temperature.

Constitutive Modeling:

Sellars & Tegart [7] suggested the use of a hyperbolic sine function to describe the relationship between rate and flow stress over a wide range of hot-working and creep conditions.

$$\dot{\varepsilon} = A \exp\left(\frac{-Q}{RT}\right)\left[\sinh\left(\alpha\sigma\right)\right]^n \quad . \qquad (2)$$

This equation is often expressed [8,9] in terms of the Zener-Holloman parameter, Z or temperature-compensated strain rate,

$$Z = A\left[\sinh\left(\alpha\sigma\right)\right]^n = \dot{\varepsilon}\exp\left(\frac{Q}{RT}\right) \quad . \qquad (3)$$

The relationship approaches a simple power law flow stress, which is typical of high-temperature creep, and asymptotes to an exponential function at high stresses, which is typical of thermally activated slip. We determined the parameters A, α, n, and Q for each of the alloys independently, and obtained activation energies, $Q \sim 120$–160 kJ/mol. While it is possible that the fundamental controlling mechanisms could be distinct between the different sheets, it was noted that these values are close to the activation energies of Mg self-diffusion and Mg-Al interdiffusion [10]. A value of $Q = 140$ kJ/mol provides a high goodness of fit (R^2 value) for all the sheets, and the use of a single value more readily allows for comparisons, since a given temperature-strain rate pair corresponds to a single value of Z for all the sheets.

Figure 7 presents the experimentally-measured flow stresses at a strain of $\varepsilon = 0.1$ for the RD of all the sheets examined and the best fit curves corresponding to Eq (3), with an activation energy of 140 kJ/mol. Table 4 presents the fit parameters and goodness-of-fit measures for each of these curves, as well as the corresponding curves from the TD samples. It is noted that the equation does not accurately describe lower temperatures ($T < 150$°C) behavior, and this is believed to be a

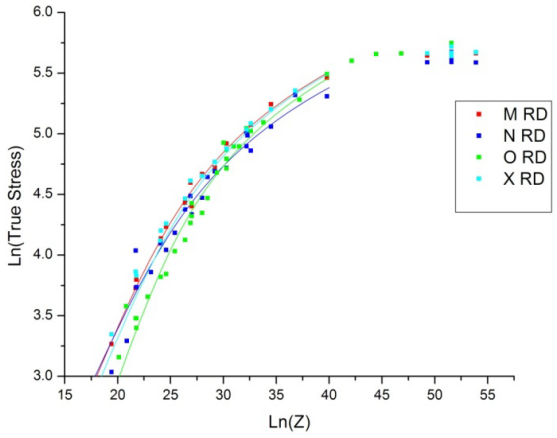

Figure 7. Best fits of the Sellars-Tegart Eq (3) to the flow stresses at a strain of 0.1 of the four sheets over a wide range of deformation conditions, Z (assuming Q = 140 kJ/mol).

Table 4. Fit parameters with the grain size.

Alloy	Grain size	ln *(A)*	*n*	*α*	R^2
M RD	11.0	22.95	4.69	0.017	0.993
M TD		22.1	4.67	0.019	0.997
N RD	8.2	21.37	3.53	0.027	0.982
N TD		23.4	4.87	0.017	0.991
O RD	5.8	22.83	3.66	0.023	0.975
O TD		24.35	3.80	0.020	0.996
X RD	8.3	23.55	4.64	0.012	0.993
X TD		25.41	5.46	0.013	0.998

result of a mechanistic transition whereby the flow stress at lower temperatures is controlled by the thermally activated slip of <a> type dislocations on non-basal planes (e.g., [3]). In summary, the overall behavior is very similar between the four heats, and that Eq (3) accurately captures the change in apparent stress exponent at high *Z*.

Focusing on the low *Z* end of the curves, a trend toward linearity is observed, i.e., the data asymptote to a power law typical of high-temperature creep. Under these conditions, alloy O has the lowest flow stresses and while the other sheets typically have power-law exponents in the range of n = 4-5 typical of diffusion-controlled climb and glide, alloy O has a lower exponent. This suggests that it may be undergoing a transition to another mechanism, such as grain-boundary sliding, characterized by n = 2. The finer grain size of sheet O would promote such a transition.

Anisotropy:

The final behavior examined is the strain anisotropy, or r-value. The r-values were measured as a function of strain from 0.1–0.3 (provided the samples underwent sufficient uniform straining to allow accurate measurements at the higher strain levels). For the present report, typical values at a strain of 0.15 are reported for tests performed along the RD and TD (Figure 8). The r-values of all the sheets tend toward 1 (isotropy) as the temperature is raised from 250 to 300°C. It has been previously reported by one of the authors [3], that this could be due to the promotion of another deformation mode at high temperatures, such as the slip of dislocations with a <c+a> Burgers vector. While this is plausible, the evidence increasingly suggests a role of a diffusion controlled process, such as dislocation climb, grain-boundary sliding, or dynamic recrystallization.

The distinct anisotropy exhibited by the four alloys (Figure 7) is readily understood in terms of their textures presented earlier (Figure 2). Sheets M and X show the highest r-values overall, and this is presumably linked with the higher over strengths of the basal textures in these sheets. Sheets N and X show greater in-plane anisotropy

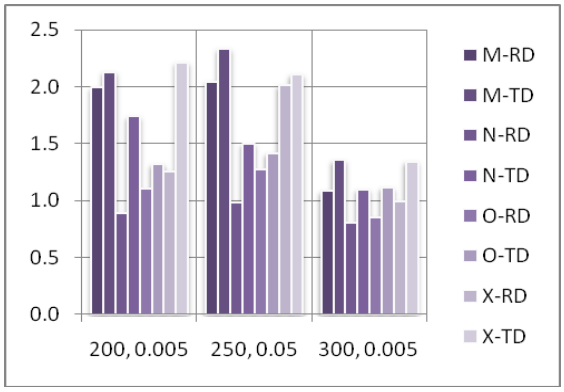

Figure 8. Comparison of r-values at a strain of ε = 0.15 show that the strain anisotropy dimishes at the highest temperatures.

than the others, and this can be explained in terms of the lower symmetry in the pole figures of these two sheets. This connection between texture and r-value was reported previously by Kaiser et al. [11] and simulated using a polycrystal plasticity model by Agnew et al. (e.g., [6,7]). The lower r-value along the RD is due to the tilt of basal poles toward the RD, which in turn allows basal slip to accommodate a large portion of the strain, while the high r-value along the TD is due to the promotion of prismatic slip, which does not produce significant strain along the thickness direction.

Summary and Conclusions

The four sheets examined in this blind study were either DC cast and hot-rolled or strip cast prior to warm/cold rolling to final gage. Neither the metallographic nor mechanical characterization made the processing history immediately apparent. Rather, simple structure property relationships were shown to describe the behaviors observed. Samples with the finest grain size exhibited the lowest flow stress and highest elongation at high temperatures (T ~ 300°C). Samples with the most asymmetric textures showed the most in-plane anisotropy in the Lankford coefficient (r-value). These results provide the process engineer with confidence that control of measurable microstructure characteristics will provide the desired control of properties, and that the details of processing history are not so important.

CANMET

The potential for warm forming was quantified by determining forming limits for strain paths including stretch, draw and bending conditions. Optical microscopy was used to determine the microstructure evolution during the warm-forming testing. General tasks included in this work consisted of:

- Determination of warm-forming limits for stretch and draw strain paths
- Establishing warm bendability (e.g., Figure 9)
- Investigating microstructural evolution during warm forming using optical metallography

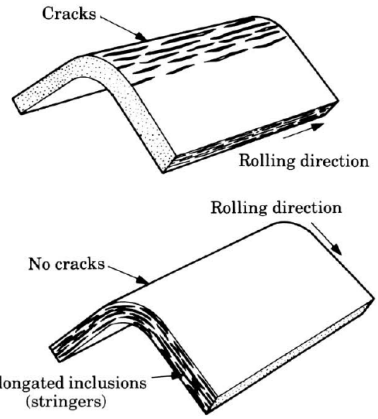

Figure 9. Bendability of sheet showing planar anisotropy.

Technical Progress

Warm-forming limits were constructed for 1.3 mm thick commercially-supplied AZ31B sheet.

- Warm FLDs are shown in Figure 10(a) for temperatures of 200°C and 250°C
- Warm-forming limits for two strain paths ($\beta = 0.8$ and -2.0, where $\beta = E_{22}/E_{11}$) were determined for range of temperatures 100 to 300°C in 25°C increments [Figure 10(b)]

Microstructural Characterization

Optical microscopy of the bulk sample reveals microstructure evolution at the limit strain for samples deformed with strain path $\beta = 0.8$. Limit strains for each temperature are given in Figure 10(b). Significant dynamic recrystallization (DRX) is observed at between 150°C and 250°C inclusive. However, DRX is most uniform and complete at 200°C [Figure 11(c)].

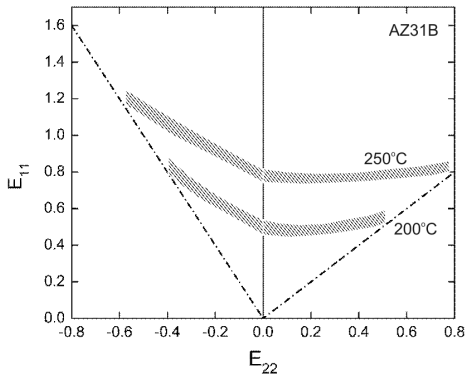

(a)

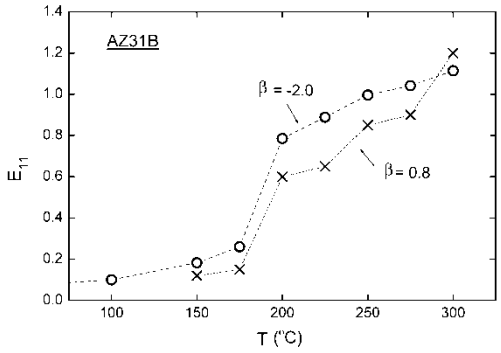

(b)

Figure 10. (a) Warm-forming limit diagrams for 1.3-mm thick AZ31B sheet and (b) forming limits for strain path $\beta = 0.8$ and –2.0 for 100 to 300°C in 25°C increments.

Inhomogeneously flow is observed at 150°C [Figure 11(b)].

At 300°C, a more equiaxed microstructure with a grain size comparable to the undeformed microstructure [Figure 11(e)] is observed, which suggests possible grain growth or the lack of DRX. The microstructure near the fracture area is compared for samples deformed at 150°C and 300°C [Figure 12(a) and 12(b)].

Planning and Deliverable for the Next Period

- Warm-forming limits will be determined for $\beta = 0.8$ for three remaining Mg sheets for temperature between room temperature and 300°C.
- Warm bending of Mg sheet will be investigated with V-notch bending for 100–300°C.

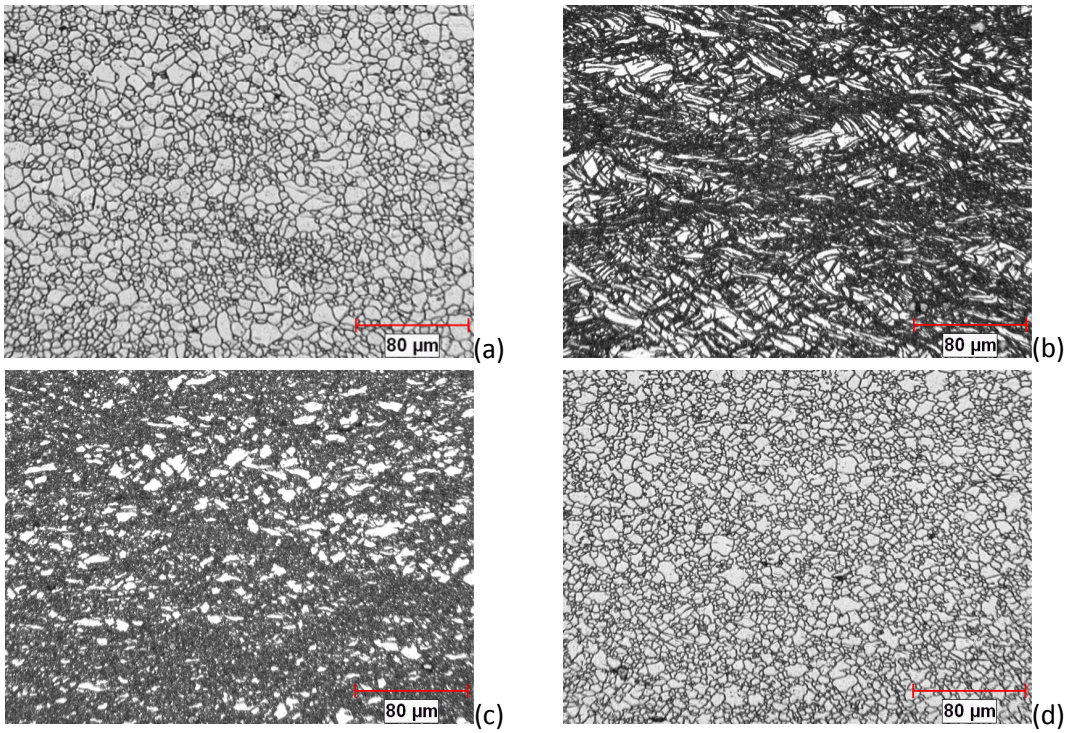

Figure 11. Optical Microscopy of RD-ND sections with strain path β = 0.8 at forming limit strain for (a) undeformed, (b) 150°C, (c) 200°C, (d) 250°C, and (e) 300°C.

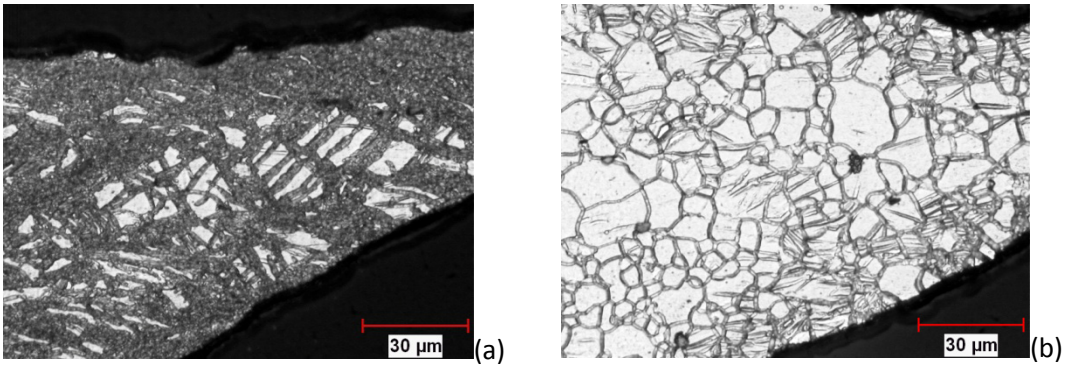

Figure 12. Optical microscopy of RD-ND sections for strain path β = 0.8 at forming-limit strain near fracture surface for a) 150°C and b) 300°C.

- A methodology for characterizing small dynamically-recrystallized grains will be investigated.
- Optical characterization of all Mg sheet at the forming limit will be completed.

Design and Build Warm Forming Tool

The previous Warm Forming Project (AMD 307) provided a great deal of information about the design and fabrication of a die for warm forming. This current project is leveraging these lessons learned and the existing equipment to create an optimized die system for warm forming.

Key elements of this optimization are using advanced simulation techniques for both thermal control (GM) and formability (Ford). A photograph of the warm-forming die is shown in Figure 13.

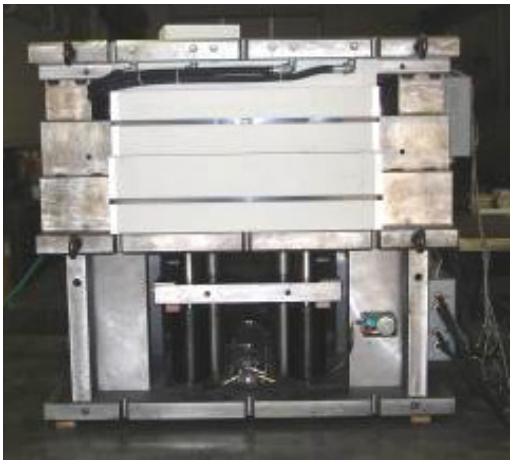

Figure 13. Modified warm forming die.

As noted in a previous report, successful pans from DC-Cast material were produced during the first forming trial to a full depth of 125 mm as shown in Figure 14. This established the feasibility to form conventional DC-cast material to a minimum of 100 mm depth which in turn achieved Gate 1 of the project.

Figure 14. Rectangular pan formed to full depth from DC-Cast AZ31.

More recently, the die has been modified to allow for the capture of both thermal and forming data through a new data-acquisition system. Data such as temperature across the tool, pressing force and forming rate will now be recorded for each formation.

Press tonnage will be measured in four locations with new load cells positioned in the die system. These load cells in cooperation with the linear potentiometer will allow for the detection of splitting as a function of both the draw depth and location. A schematic of the new cushion system re-designed to accommodate the load cells is shown in Figure 15.

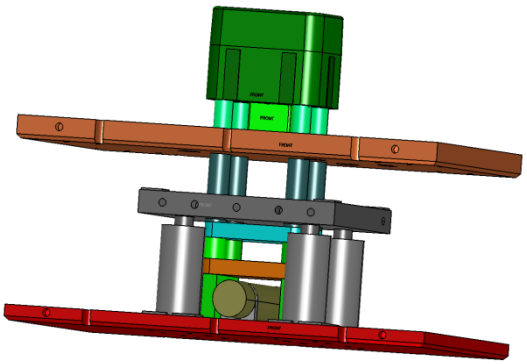

Figure 15. Schematic of the lower cushion system showing the new design to accommodate the four load cells.

The data-acquisition system designed and purchased in the previous Warm Forming Project (AMD 307) will be used to record the data from the load cells, linear potentiometer and the thermocouples.

Deliverables:

- Warm-forming die with improved thermal control and instrumented to record critical forming data such as temperature, press tonnage and deformation rate.
- Established feasibility to form conventional DC-cast material to a minimum of 100 mm depth. (Gate 1 Achieved)

Press Design and Optimization

A hydraulic press, shown in Figure 16, was chosen for the development and modified to perform the required strokes per minute and operate at different travel speeds. The press in its original state was relatively slow with a maximum down-speed of 43 mm per second and an up-speed of 56 mm per second. In order to achieve the targeted cycle times, new hydraulics were designed and implemented on the press to achieve significantly faster speeds.

The study done to modify the press hydraulic system showed that by adding a second pump and motor, modifying the existing cylinder and adding a larger oil tank, the following range of speeds could be obtained.

Down Pressing Speed 1	42.3 mm per second
Down Pressing Speed 2	80.4 mm per second
Down Pressing Speed 3	152.4 mm per second
Rapid Down Speed	311.1 mm per second
Rapid Up Speed	296.3 mm per second

Figure 16. Photograph of new dedicated press and pre-heater for the development of the fully automated warm-forming cell.

The next forming trial will be conducted using the range of speeds to determine optimal pressing speed and temperature. Subsequent trials will be performed to quantify the formability of all of the test alloys under identical forming conditions.

Deliverables:

- Dedicated hydraulic press for the AMD 602 project capable of achieving the targeted production rate of 5 to 10 jobs per minute.

Forming Trials

The aim of the first full forming trial on the newly-modified press system at Troy Tooling was to develop baseline formability data on a commercially-available Mg sheet alloy. Variables such as draw depth, binder load, forming temperature and lubricant were all investigated to determine a suitable forming window for this material as well as to develop metrics to compare the formability of all the test alloys. In this section, the results of this first full forming trial are presented and discussed.

Experimental Procedure

To minimize variation, a standard process of heating the blanks in the die was used for this trial. All experiments were conducted at a pressing speed of 80.4 mm per second which is approximately half the full speed of the press. Two lubricants were used in this investigation—the solid lubricant containing boron nitride developed in the previous project (AMD 307) which has been shown to be an effective lubricant and a new oil-based lubricant available from Fuchs called Stabylan 600HT. Interest in a new oil-based lubricant stems from two issues with the currently used solid lubricant. The first of these has to do with the cost of applying the lubricant to the sheet as well as the cost of the lubricant itself. The second issue is related to the potential for the lubricant to build up in the die and the cost of cleaning off the lubricant from the formed panels. Hence, the target for an oil-based lubricant is to be compatible with down-stream processes such that cleaning of formed panels would not be necessary. The Stabylan 600HT lubricant used in this work has a flash point around 300°C so it could not be used at all of the test temperatures of interest.

The pan formed in this work (Figure 14) is a significant test of material drawability. Each corner can be viewed as a unique experiment during the forming process, with two failure modes: splits and wrinkles. Wrinkling occurs when insufficient binder pressure is applied so that the material buckles rather than compresses in the corners. Splits occur when there is insufficient ductility in the material to be stretched into the desired shape.

Results and Discussion

A forming window based on a wide range of temperatures and binder pressures is shown in Figure 17. In this plot, panels with one or two successfully formed corners are binned together as well as panels with three and four successfully-formed corners. All of these panels were formed with the solid lubricant and binned in terms of the number of successfully-formed corners. As predicted, the forming window becomes wider in terms of binder pressure at the higher temperatures. Insufficient binder pressure results in wrinkles and failure. The forming window collapses at approximately 275°C which indicates a minimum temperature to achieve a successfully forming.

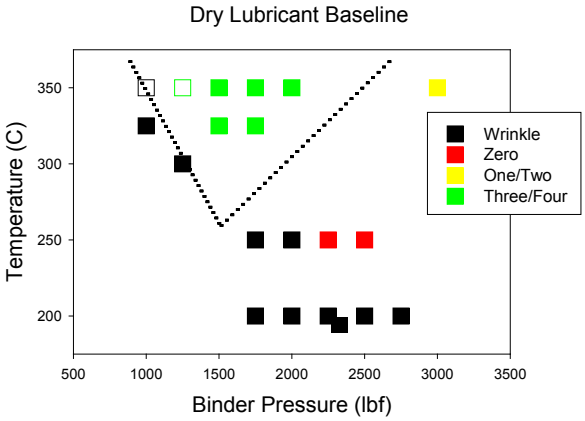

Figure 17. Forming window as a function of temperature and binder force. The successful number of corners made have been lumped in to two groups (3&4 and 1&2).

Lubricant

The Stabylan 600HT lubricant has a flash point at approximately 300°C so experiments were performed at a maximum of 290°C. As shown in Figure 18, no pans were successfully formed and a distinct border between wrinkling and splitting developed. While the results of Figure 17 indicate that some level of forming success is possible at temperatures in this range, there were no successful corners recorded for the pans formed with oil. This is most likely a result of lubricant breakdown as the temperatures approached the flashpoint. Further investigations into this lubricant (shown below) reinforce this conclusion.

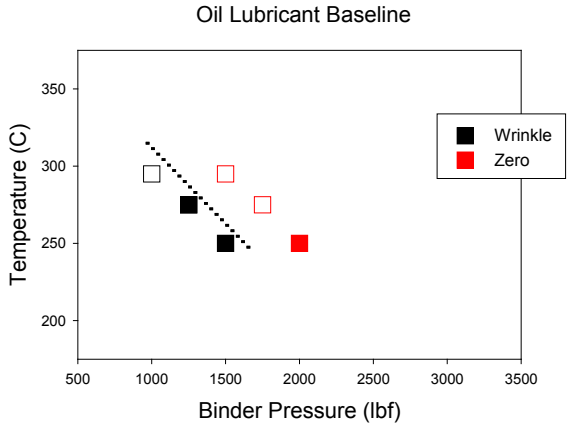

Figure 18. Plot shows a distinct transition from wrinkling to complete splitting for pans formed with oil-based lubricant up to 290°C.

Pan Depth

While the metric of successfully-formed corners has led to the development of the forming window shown in Figure 17, a more robust metric with improved resolution was sought. The chosen metric was pan depth. That is, the maximum depth a pan could be formed before splitting of any of the corners. In order to determine this value for a given set of forming parameters (temperature, binder pressure, etc.), a large number of pans would need to be formed. Since this method was impractical given the large number of variables under study, a method was developed to estimate maximum forming depth.

Pan depth was estimated by measuring the opening height of the largest corner crack (Figure 19) and subtracting that value from the full pan depth of 70 mm. This approach has been validated on a number of panels by re-configuring the press to draw to this target pan depth. In each of these tests a distinct neck was formed on the corner indicating the onset of splitting. Once splitting occurs, the material around the crack does not continue to deform and hence the crack opens the remaining stroke of the press.

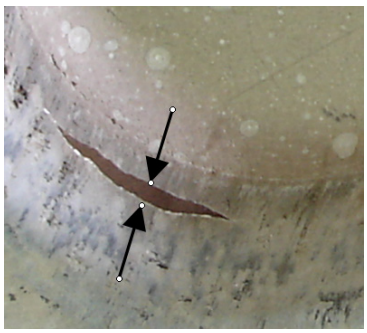

Figure 19. An example of a corner split measured for the estimation of pan depth.

This crack-measuring method was used to further evaluate the forming behavior of this baseline material under a number of different conditions. The first investigation was on the effect of temperature at various binder pressures.

As shown in Figure 20, the pan depth increases with increasing temperature. The straight line at 350°C is due to the fact that the die bottomed out at 70 mm and it was not possible to draw the

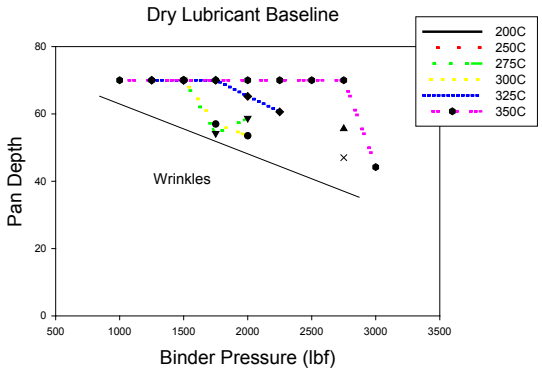

Figure 20. Plot of estimated pan depth as a function of binder force for various temperatures.

material further. If the tool were re-worked to allow for deeper forming, the suspicion is that there would be a series of parallel lines with a similar slope to the wrinkle line.

The pan-depth analysis approach was also used to compare the performance of the two lubricants used in this study. Pan depth as a function of binder pressure for temperatures ranging from 250°C to 290°C are plotted in Figure 21. For all conditions, use of the solid lubricant (dry) improves estimated pan depth. This shows a clear benefit of the dry lubricant even at lower temperatures of 250–295°C.

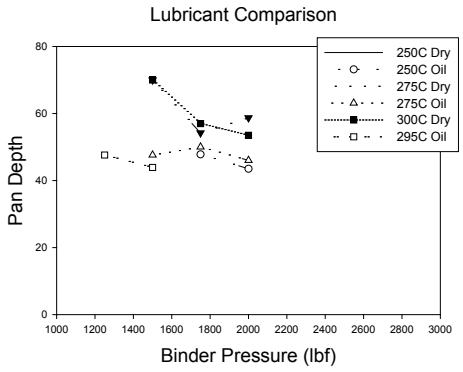

Figure 21. Estimated pan depth as a function of binder force for various temperatures for both lubricants.

Non-Isothermal Conditions

One method of improving the forming depth that has been demonstrated by several researchers is to slightly cool the punch. While the research to date on this approach has been mostly limited to laboratory-scale experiments, the concept is based on having hotter material on the binder to flow into the cavity while colder and hence stronger material in the cavity to resist necking and rupture. Preliminary experiments were attempted with the current pan die in an effort to reproduce the results from lab-based experiments. The method used was simply to turn off the heat in the punch and leave the binder in the lowest position to minimize heat transfer from the ring to the punch. While this did not offer precise control of the punch temperature, it did give a first approximation of what could be achieved in a non-isothermal system.

As noted in Figure 22, it appears that a cooler punch results in an increase in pan depth. The potential of non-isothermal warm forming will be studied further under more controlled conditions in the next forming trial.

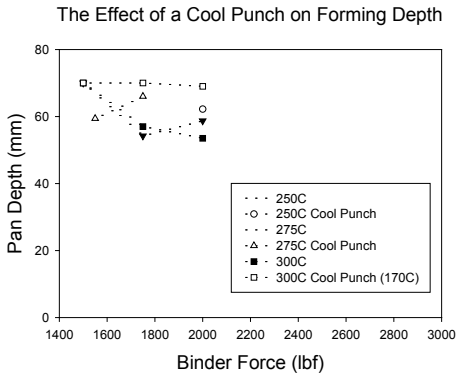

Figure 22. Estimated pan depth as a function of binder force for both isothermal and non-isothermal conditions.

Materials

A final study in this forming trial was conducted by comparing the formability of all four of the test materials at various temperatures. This preliminary study was limited to the use of the oil-base lubricants. In the next forming trial, the solid lubricant will used on all of the materials.

As noted in Figure 23, the estimated pan depth decreases with increasing temperature. While this is surprising since all of the previous data indicate improved formability with increasing temperature, this anomaly is most likely due to the further deterioration of the oil-based lubricant with increasing temperature. Follow-on studies using

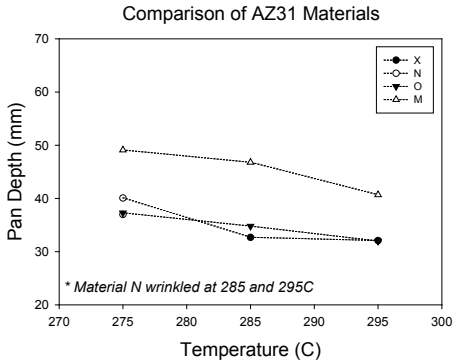

Figure 23. Estimated pan depth for all four materials in this study as a function of temperature.

the previously-developed solid lubricant will offer a better comparison of material formability.

Automated Cell and Demonstration

The final phase of the project will involve constructing a fully-automated warm-forming cell using the optimized pan die. Troy Tooling Technologies will integrate the conduction preheater and die using automated material handling to create a warm-forming cell that can produce a formed pan at a rate of 5 to 10 a minute. The process will be demonstrated to the OEM's and DOE.

Conduction Pre-Heater

A conduction preheater originally developed at GM was loaned to the AMD 602 project. This preheater was developed to rapidly heat metal sheets by conduction from two hot, steel platens placed in very close proximity to the sheet, without making intimate contact. Maintaining a small gap between the platens and the sheet is essential for achieving a very high rate of heat transfer. In this situation, the majority of the heat is transferred from the hot steel platen through a thin layer of open space (air) to the Mg sheet. For small gaps, conduction heat transfer is more dominant than either radiation or convection.

Modeling of heat transfer by conduction from solid heated platens through a controlled clearance gap of 0.5 mm on each side to a 1 mm thick Mg sheet indicate that the sheet can be heated to 400°C in less than 40 seconds (Figure 24).

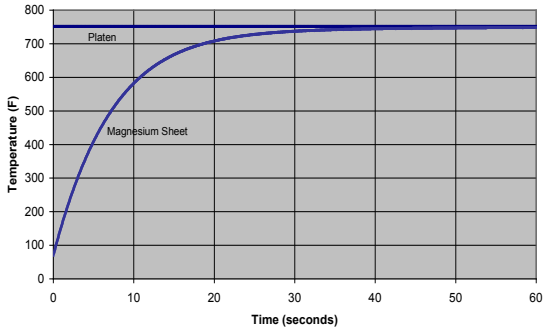

Figure 24. Heating curve of 1mm Mg sheet in the 400°C preheater with a 0.5 mm air gap on both sides of the sheet.

By placing three sheets in the preheater at once and then removing one sheet every 12 seconds and replacing it with a cold sheet, a production preheat cycle of 5 parts per minute can be achieved with the preheater. A photograph of the preheater is shown in Figure 25.

All subsequent forming trials will utilize this preheater.

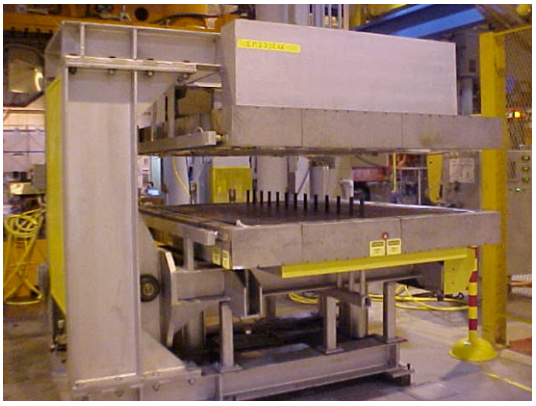

Figure 25. Photograph of the GM conduction preheater.

Deliverable:

- A heating system capable of producing blanks at target temperature at a rate fast enough to support the targeted production rate.

Cost Model

AMD 307 developed a cost model for warm forming in cooperation with Camanoe Associates. This model will be modified to understand the costs of warm forming of Mg sheet and to

establish the benefits of using lower-cost CC materials

References

1. "Standard Test Method for Determining the Superplastic Properties of Metallic Sheet Materials," *ASTM E 2448–06,* ASTM International, West Conshohocken, PA, 2006.
2. G. Vander Voort, in *Metallography Principles and Practice*, ASM International, Materials Park, OH (1984), pp. 447–449.
3. S. R. Agnew and O. Duygulu, "Plastic anisotropy and the role of non-basal slip in magnesium alloy AZ31," *Inter. J. Plasticity*. 21 (2005), pp. 1161–1193.
4. A. Jain and S. R. Agnew, "Modeling the temperature dependent effect of twinning on the behavior of magnesium alloy AZ31B sheet," *Mater. Sci. Eng. A*, 462 (2007), pp. 29–36.
5. L. Jiang, "Effect of twinning on texture and strain hardening in magnesium alloys subjected to different strain paths." Ph.D. dissertation, McGill University, Montreal, Canada (2007), pp. 46–66.
6. S. R. Agnew et al., "Constitutive behavior of four wrought magnesium alloys under warm forming conditions," in *Magnesium Technology 2008*, Ed. Pekguleryuz et al., TMS, Warrendale, PA (2008), pp. 159–164.
7. C. M. Sellars and W. J. Tegart, "Relationship between strength and structure in deformation at elevated temperature," *Mem. Sci. Rev. Metall.*, 63 (1967), pp. 731–745.
8. H. Takuda, H. Fujimoto, and N. Hatta, "Modeling on flow stress of Mg-Al-Zn alloys at elevated temperatures," *J. Mater. Proc. Tech.* 80–81 (1998), pp. 513–516.
9. M. R. Barnett, "Influence of deformation conditions and texture on the high temperature flow stress of magnesium AZ31," *J. Light Met. 1,* (2001), pp. 167–177.
10. S. S. Vagarali and T. G. Langdon, "Deformation mechanisms in h.c.p. metals at elevated temperatures—II. Creep behavior of a Mg-0.8% Al solid solution alloy," *Acta Metall.,* 30 (1982), pp. 1157–1170.
11. F. Kaiser et al. "Anisotropic Properties of Magnesium Sheet AZ31," *Mat. Sci. Forum.* 419–422 (2003), pp. 315–320

C. Electromagnetic Forming of Aluminum Sheet

Principal Investigator: Richard W. Davies
Pacific Northwest National Laboratory
P.O. Box 999, Richland, WA 99352
(509) 375-6474; fax: (509) 375-5994; e-mail: rich.davies@pnl.gov

Technical Coordinator: Sergey Golovashchenko
Ford Motor Company
Ford Research Laboratory, Dearborn, MI 48121-2053
(313) 337-3738: fax: (313) 390-0514; e-mail: sgolovas@ford.com

Technology Area Development Manager: Joseph A. Carpenter
(202) 586-1022; fax: (202) 586-1600; e-mail: joseph.carpenter@ee.doe.gov

Field Technical Monitor: Mark T. Smith
(509) 375-4478; fax: (509) 375-4448; e-mail: mark.smith@pnl.gov

Participants:
Nick Bessonov
EMF Simulations
University of Michigan-Dearborn

Jeffrey Johnson
EMF System and Control
Pacific Northwest National Laboratory

Vladimir Dmitriev
EMF R&D
Ford Motor Company

Contractor: Pacific Northwest National Laboratory (PNNL)
Contract No.: DE-AC06-76RL01830

Objective

- Develop electromagnetic forming (EMF) technology that will enable the economic manufacture of automotive parts made from aluminum sheet. EMF is a desirable process because the dynamic nature of the deformation results in benefits, including increased forming limits and reduced springback. These benefits would result in increased use of aluminum and therefore more fuel-efficient vehicles due to mass reduction.

Approach

- The project will address four main technical areas:
— Analysis methods for forming system design
— Development of durable actuators (coils)
— Industrial embodiment of the EMF process
- Modeling tools for simulation of the EMF forming process.

Accomplishments

- During the last year of this project, remaining funds were directed at completing documentation of the EMF modeling code approaches for reduced computational run times. This work was funded through a subcontract with Oakland University, and final work will be completed in early fiscal year (FY) 2009.
- Modeling of sheet-die interaction during EMF was completed during the reporting period, and results of this work were presented (and published) at the Third International Conference on High Speed Forming.
- A subcontract with Pennsylvania State University-Erie to evaluate the effects of electrical pulsing on the deformation characteristics of 5000-series aluminum alloys was completed. This work focused on evaluating whether the tensile ductility of the 5000-series aluminum alloys can be increased with the application of high energy electrical pulsing. This work resulted in a recent publication.

Future Direction

- This project will be finished with the completion of a final subcontract report documenting the EMF modeling code development and benchmarking computational efficiency improvements. A related high rate forming project has been initiated with participation by Chrysler, Ford, and General Motors. This project, titled "Pulse Pressure Forming of Lightweight Materials" (see report 2.E) is focused on the forming characteristics of aluminum, advanced high-strength steels, and magnesium sheet under electrohydraulic forming conditions.

Introduction

In the EMF process, a transient electrical pulse of high magnitude is sent through a specially designed forming coil by a low-inductance electric circuit. During the current pulse, the coil is surrounded by a strong transient magnetic field, the transient nature of which induces current in a nearby conductive workpiece that flows opposite to the current in the coil. The workpiece and coil act as parallel currents through two conductors to repel one another. The force of repulsion can be very high, equivalent to surface pressures approximately tens of thousands of pounds per square inch. Thin sheets of material can be accelerated to high velocity in a fraction of a millisecond.

A recent interest in understanding the EMF of metals has been stimulated by the desire to use more aluminum in automobiles. The high workpiece velocities achievable using this method enhances the formability of materials such as aluminum. In addition, the dynamics of contact with the forming die can help reduce or mitigate springback, an undesired effect that cannot be avoided in other forming techniques such as stamping. The commercial application of this process has existed since the 1960s, with the large majority of applications involving either the expansion or compression of cylinders (tubes). The forming of sheet materials is considerably more complex and receives relatively little attention.

Approach

This project addresses three main technical areas. The first involves establishing analysis methods for designing forming systems. These methods are based on developed knowledge of forming limits and relations between electrical system characteristics and deformation response for specific aluminum alloys of interest. The second area is coil durability. Existing EMF and relevant knowledge from pulsed power physics studies will be combined with thermomechanical analyses to develop durable coil designs that will be tested experimentally. The third technical area involves the industrial embodiment of the EMF process. In this project, EMF is expected to be hybridized with conventional sheet metal stamping. Different approaches to hybridization will be analyzed for issues affecting the economic implementation in a modern stamping plant, and different system concepts will be developed and studied. Existing knowledge of the EMF process and technical achievements in this project will be combined to establish a methodology for designing hybrid-forming systems that can be readily integrated into modern manufacturing facilities for the economic production of automotive sheet aluminum

components. Some of the project focus areas and results are discussed in the following sections.

PNNL EMF System

The EMF system at PNNL has been operational since 2001. The system typically operates at 6,500 volts, and current levels in excess of 225 kiloamperes (kA) have been demonstrated. Figure 1 shows a typical response of the EMF system during a 15 kilojoule discharge of the capacitor bank. The half-current of the system (measuring half the total system current) is approximately 86 kA so that a total current of 172 kA passed through the load coil is within 26 microseconds.

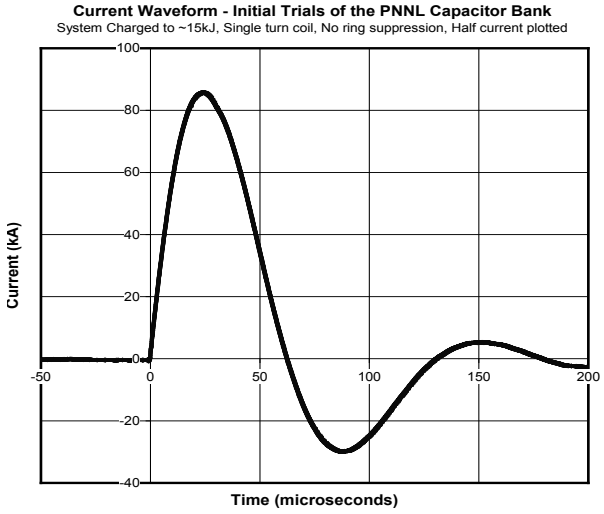

Figure 1. Typical EMF system waveform.

The system has also been cycled several thousand times at high current levels, while supporting our coil durability experimental work. The custom-designed control system was successfully demonstrated in automated cyclic loading operating modes. In the second half of FY 2007, a new power supply was installed and operationally validated. The supply has a significantly faster charge rate capacity that allowed faster recharging of capacitor banks so that the coils can be fired at higher cycle rates. This reduces the experimental run times required to test coil designs for coil durability.

EMF Process Simulation Tool Development

The first half of FY 2008 was primarily spent on further development of an EMF process simulation tool that will allow us to design the process by predicting the EMF field, stresses and strains in the blank and temperature distribution in the coil. Another focus area was the continued development of the flat coil design. Improvements were made to simplify and lower the manufacturing cost of flat coils. Further, the packaging of the flat coil assembly has been improved for robustness and ease of handling. Efforts were initiated to modify the code to run on Unix-based workstation clusters and to investigate advantages in parallelizing the code for faster run times.

EMF Process Numerical Simulation Results

The EMF process is challenging to simulate due to the need to model electromagnetic, thermal and elastic-plastic deformation of materials simultaneously. Many of the commercial research codes have serious limitations and an inability to predict EMF process results accurately. Originally, this project focused on integrating portions of existing commercial research codes to predict the important characteristics of a three-dimensional EMF process accurately. However, recent work focused on more accurate custom process simulations. The current modeling work involves collaboration with Dr. Nick Bessonov in cooperation with Oakland University and Dr. Sergey Golovashchenko at Ford.

During the last half of FY 2008, modelling focused on the interaction between the aluminium sheet formed at high velocity and the die into which it is being formed. The modelling of the sheet/die interaction requires development of the contact interaction, the most popular method of which is based on the geometrical analysis of the mutual position boundary nodes of each mesh. At every integration step, it is verifying whether a boundary node of the blank has penetrated through the certain element of the die surface mesh. If this happens, it would be necessary to make certain corrections to bring back the node to the die surface, along which the node could slide. A significant drawback of this approach is an occasional penetration of the node through the

surface, which can happen due to inaccurate calculations. As soon as the blank's node penetrates the die's surface, it is unable to return, so further calculations are useless. Therefore, a different approach was employed based on mild contact, which is popular in molecular dynamics where it is employed to model thousands of colliding atoms. The contact force is in inverse proportion to the distance between interacting surfaces. From a mathematical viewpoint, mild contact is some variable boundary of an unknown shape where the nonpenetration condition and equilibrium of forces between both surfaces must be satisfied. This idea is based on the introduction of acting-in-vicinity forces repelling the surfaces to be in contact. As a result, the surfaces do not come in contact but stay at a brief distance from each other. The force is localized in a small neighborhood of mesh elements, and it increases to infinity when the distance between them approaches zero.

In other words, when the blank and die are in geometrical contact, the force between them is localized on their joint surface. Mathematically, it can be considered as continuous functions where the absolute value of the force F is given by

$$F = \begin{cases} k\left(\frac{1}{h} - \frac{1}{h_0}\right) & \text{at} \quad h < h_0 \\ 0 \quad \text{at} \quad h \geq h_0 \end{cases},$$

where h is the actual distance from the node of the blank to the die surface and h_0 is the width of the layer where the force is different from zero. The direction of the force F is aligned along the local normal to the die surface. The described algorithm takes into account the Coulomb friction and other contact effects. Indeed, when the interaction of the node with an object of the other mesh is computed, the mutual positions and velocities are known. It is sufficient to find the friction directed along the tangent to the surface and opposite to the tangential part of the relative velocity vector.

Effect of Electrical Pulsing on Deformation Behavior of Various Aluminum Alloys

Under a subcontract with Pennsylvania State University-Erie, research was conducted to evaluate the effects of electrical pulsing on the deformation behavior of selected aluminum tensile test samples. Previous studies have shown that the presence of a pulsed electrical current applied during the deformation process of an aluminum specimen can significantly improve the formability of the aluminum without heating the metal above its maximum operating temperature range. This research extends these findings by examining the effect of electrical pulsing on 5052 and 5083 aluminum alloys. Two different parameter sets were used while pulsing three different heat treatments (as is, 398°C and 510°C) for each of the two aluminum alloys. For this research, electrical pulsing is applied to the aluminum while the specimens are deformed without halting the deformation process. The analysis focuses on establishing the effect of electrical pulsing on the aluminum alloy's various heat treatments by examining the material displacement throughout the testing region of dog-bone shaped specimens.

The results from this research show that pulsing significantly increases the maximum achievable elongation of the aluminum compared to baseline tests conducted without electrical pulsing. Significantly reducing the engineering flow stress within the material is another beneficial effect produced by electric pulsing. The pulses also cause the aluminum to deform nonuniformly such that the material exhibits a diffuse neck where the minimum deformation occurs at the ends of the specimen (near the clamps), and the maximum deformation occurs near the center of the specimen (where fracture ultimately occurs). This diffuse necking effect is similar to what can be experienced during superplastic deformation. However, when comparing the presence of a diffuse neck in this research, electrical pulsing does not create as significant a diffuse neck as superplastic deformation. Electrical pulsing has the potential to be more efficient than traditional methods of incremental forming because the deformation process is never interrupted.

Overall, with the greater elongation and lower stress, the aluminum can be deformed quicker, easier, and to a greater extent than is currently possible. Figure 2 shows the load/displacement record for the as received 5052 specimens tested

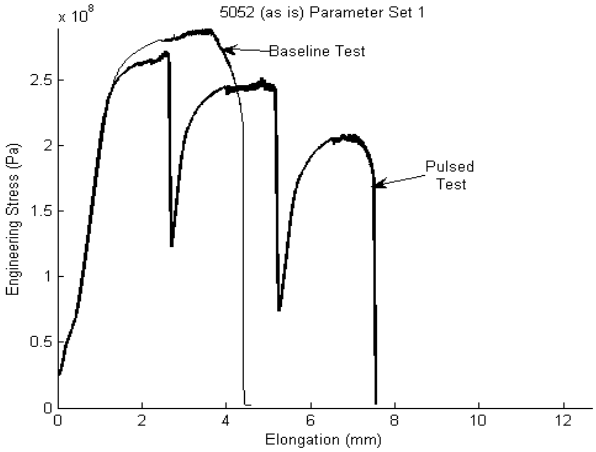

Figure 2. 5052 (as is) load/displacement results.

in baseline static tensile conditions and the same 5052 material subjected to parameter set 1 electrical pulsing. The pulsed specimens displayed significantly higher elongations prior to failure.

The test results show that electrical pulsing of the specimen results in significantly greater displacements (higher apparent formability) than that of the baseline test conditions. Similar results were observed for 5052 and 5083 aluminum alloys, and the subcontract effort resulted in publication of the results for the 2008 International Manufacturing Science and Engineering Conference.

Figure 3 shows summary displacement analysis data for 5052 aluminum deformed in tension under

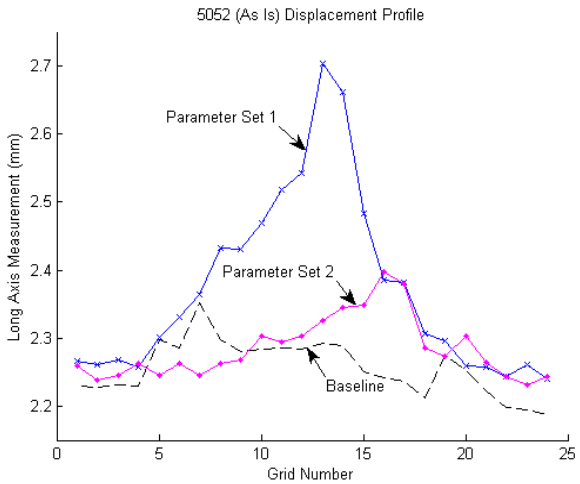

Figure 3. 5052 (as is) displacement analysis.

regular static test conditions and then with electrical pulsing using two different parameter sets.

Conclusions

This work has developed numerical models that describe three critical elements of the EMF process: propagation of the electromagnetic field through the coil-blank system and generation of pulsed electromagnetic pressure in specified areas, high-rate deformation of the blank and heat accumulation, and transfer through the coil with an air cooling system. The process models provide capability to analyze EMF restrike processes from the perspective of coil design, blank deformation, and coil cooling systems.

Presentations/Publications

1. W. Salandro, J. Jones, T. McNeal, J. Roth (Penn State-Erie), S. T. Hong, and M. Smith. 2008. *Effect of Electrical Pulsing on Various Heat Treatments of 5XXX Series Aluminum Alloys,* Proceedings of the 2008 International Manufacturing Science and Engineering Conference, Pacific Northwest National Laboratory, October 7–10.
2. R. W. Davies, N. M. Bessonov, and S. F. Golovashchenko. 2007. "Prototype Coil Performance during Electromagnetic Forming of Aluminum Sheet." Abstract submitted to *Materials Science & Technology*, Detroit, MI. PNNL-SA-54918.
3. S. Golovashchenko, N. M. Bessonov, and R. W. Davies. 2008. *Analysis of Blank-Die Contact Interaction in Pulsed Forming Processes.* Third International Conference on High Speed Forming. PNNL-SA-59420.
4. S. F. Golovashchenko, N. M. Bessonov, and R. W. Davies. 2008. *Modeling of Pulsed Electromagnetic Forming.* Numisheet 2008. PNNL-SA-60489.

D. Pulse Pressure Forming of Lightweight Materials

Principal Investigator: Richard W. Davies
Pacific Northwest National Laboratory
P.O. Box 999, Richland, WA 99352
(509) 375-6474; fax: (509) 375-5994; e-mail: rich.davies@pnl.gov

Technical Coordinators: Sergey Golovashchenko
Ford Motor Company
Ford Research Laboratory, Dearborn, MI 48121-2053
(313) 337-3738; fax: (313) 390-0514; e-mail: sgolovas@ford.com

John Bradley
General Motors Corporation
General Motors Research Laboratory, Warren, MI 48090-9055
(586) 986-0590; fax: (586) 986-3091; e-mail: john.r.bradley@gm.com

Jerry Olszewski
Chrysler LLC
Applied Materials Technology, Auburn Hills, MI 48326
(248) 512-8531; fax: (248) 512-7915; email: go5@chrysler.com

Technology Area Development Manager: Joseph A. Carpenter
(202) 586-1022; fax: (202) 586-1600; e-mail: joseph.carpenter@ee.doe.gov

Field Technical Monitor: Mark T. Smith
(509) 375-4478; fax: (509) 375-4448; e-mail: mark.smith@pnll.gov

---

Contractor: Pacific Northwest National Laboratory
Contract No.: DE-AC06-76RL01830

Objective

- Develop pulse pressure forming (PPF) sheet metal forming technologies [e.g., electromagnetic forming (EMF), electrohydraulic forming (EHF), laser shock forming (LSF) and other similar technologies] and manufacture cost effectively body-in-white and closure panels made from aluminum alloys, magnesium alloys, and high-strength and advanced high-strength steel (HHS and AHSS, respectively).

Approach

- Develop and enable a class of high strain rate metal forming processes to cost-effectively manufacture body-in-white and closure panels made from aluminum alloys, magnesium alloys, and HSS/AHSS.
- Overcome three technical barriers to using PPF processing for more cost-effective lightweight vehicles:
  - — lack of understanding of the formability and strain rates that develop during PPF processing
  - — lack of validated constitutive relations for lightweight materials during PPF processing
  - — lack of validation of finite element simulation of PPF processing

Accomplishments

- Design, development, and fabrication of a PPF chamber and electrode system and development of experimental procedures, including validation of high-speed camera imagining and forming of test samples in the free-forming mode.
- Implementation of a high-speed camera and image analysis system to record the forming of electrohydraulic aluminum sheet specimens and electromagnetic forming of aluminum samples. Efforts will be made to provide higher resolution of the sheet specimen forming surface in future experiments.

Future Direction

- Complete equipment development and characterize forming of aluminum and steel sheet specimens.
- Characterize real-time strain rates during PPF using the high-speed camera and image analysis system.
- Investigate mechanisms for enhanced formability at elevated strain rates.

Introduction

The ultimate goal of the project is to extend the formability of high strength light metals and AHSS through the application of high forming rate PPF techniques. The deliverables for the project will be the understanding and quantification of the effects of high-rate forming on the formability, residual stress state and formed properties of several high strength lightweighting metal sheet materials, facilitating the extended forming of complex, lightweight automotive sheet components.

PPF is emerging as an attractive alternative to both conventional stamping processes and forming methods that are more advanced, such as superplastic forming and EMF. Previous project work on EMF has demonstrated enhanced formability for aluminum sheet, but the process is limited to high-conductivity materials. Because the high energy discharge develops a rapid high pressure forming pulse, PPF is not limited by the inherent conductivity of the sheet material and can therefore be used to form AHSS, titanium, aluminum, magnesium and stainless steel sheets. As with EMF, PPF offers the ability to develop extended ductility, allows the use of less expensive, single-sided tooling and results in little or no springback after forming. Although there are a number of established methods for generating the forming pressure pulse, little is understood about how PPF interacts with the forming material and what the practical forming limits are for such metal alloys as magnesium, aluminum, titanium, and AHSS. This project will conduct a series of PPF experiments to determine basic PPF operational requirements and capabilities and to generate material formability/property relationships for a series of selected sheet materials. PPF will be demonstrated on materials having significantly lower electrical conductivity than aluminum, which can be electromagnetically formed. Results from the project will include an enhanced understanding of PPF effects and the impact PPF can have on basic metal formability, design properties and forming limits as well as material property data on post-PPF materials.

Approach

The purpose of this project is to develop a formability database and more fundamental understanding of the behavior of automotive sheet materials during PPF. PPF presents a number of important variables, including generation of the pressure pulse, transmission of the pulse to the working material and the displacement path of the sheet material within the tooling or die. The project will focus on the behavior of the sheet materials during PPF and will generate biaxial forming limit data, post-formed properties, and pressure-time-displacement relationships for selected sheet materials.

The deliverables of the project include the following.

1. Fundamental relationship between pulse-generated pressure forming of selected sheet

materials, including development of biaxial forming limit relationships for variable levels of pulse pressure, rate and duration.

2. Development of pre- and post-formed property relationships for selected sheet materials, including AHSS, titanium, and magnesium.
3. Development of a strain-path based forming relationship that can be used to guide PPF component and tooling design.
4. Validation of springback behavior as a function of PPF process parameters.
5. Demonstration of the technical basis for combining warm forming capability with the PPF process.

Results

Project work to date has focused on the design and fabrication of a suitable PPF chamber capable of forming sheet metal specimens under high strain-rate forming conditions. Figure 1 shows the hemispherical PPF chamber containing the two electrodes used to discharge the high voltage charge from the capacitor bank. The chamber is filled with water and the forming sheet specimen sealed to the top of the chamber, with a bolted hold down ring pictured alongside the PPF chamber. Discharge of the electrical pulse between chamber electrodes generates a rapid high-pressure event within the chamber, resulting in the formation of the sheet specimen under high strain rate conditions. Initial test firings of the chamber have confirmed general function and demonstrated suitable strain rates in the formed sheet samples. The use of a high-speed camera system based around Correlated Solutions, Inc. image analysis software was also completed during mid-September PPF tests.

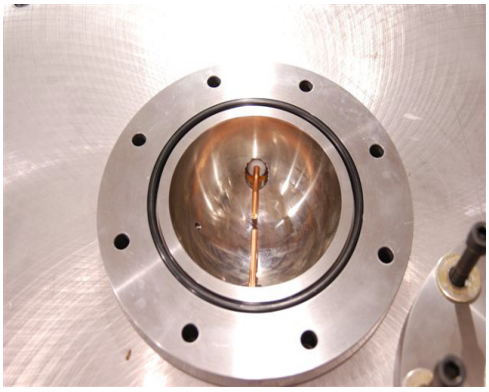

Figure 1. PPF chamber with discharge electrodes. Sheet specimen hold-down ring is shown to the right.

Conclusions

1. A survey of existing high strain rate testing and associated material constitutive modeling approaches was completed during the last quarter of fiscal year (FY) 2008.
2. The design, fabrication and testing of the PPF chamber and electrode system were completed in late FY 2008 using the PNNL capacitor bank.
3. A system of high-speed cameras was demonstrated in FY 2008, and resulting images were used by the Correlated Solutions system to determine specimen strain rates during PPF tests.

Presentations/Publications/Patents

1. R. W. Davies, E. Stephens, and M. T. Smith. 2008. *Pulse Pressure Forming of Lightweight Materials,* Project Review Meeting. October 28.

E. Ultrafine Grained Foils and Sheets by Large Strain Machining Processes

Principal Investigator: Mark T. Smith
Pacific Northwest National Laboratory
P.O. Box 999, Richland, WA 99352
(509) 375-4478; fax: (509) 375-4448; e-mail: mark.smith@pnl.gov

Principal Investigators: S. Chandrasekar and K. P. Trumble
Purdue University
West Lafayette, Indiana
(765) 494 3623; chandy@ecn.purdue.edu

Technology Area Development Manager: Joseph A. Carpenter
(202) 586-1022; fax: (202) 586-6109; e-mail: joseph.carpenter@ee.doe.gov

Field Technical Manager: Mark T. Smith
Pacific Northwest National Laboratory
P.O. Box 999, Richland, WA 99352
(509) 375-4478; fax: (509) 375-4448; e-mail: mark.smith@pnl.gov

---

Contractor: Pacific Northwest National Laboratory (PNNL)
Contract No.: DE-AC06-76RL01830

Objective

- Demonstrate the feasibility of producing magnesium (Mg) sheet and shaped products having superior formability and strength properties through the application of severe plastic deformation (SPD) developed by large-strain extrusion machining and peeling techniques.
- Evaluate the commercial economics of the candidate SPD techniques for production of fine-grained Mg alloy sheet.

Approach

- Establish the process and tooling capabilities for large strain extrusion machining (LSEM) and peeling in the context of creating bulk foil/sheet from Mg alloys. Specific attention will be paid to design of process conditions (e.g., pre-heating of sample, avoiding shear localization) to realize continuous chip formation.
- Carry out preliminary optimization of process conditions for foil/sheet production.
- Characterize the hardness and microstructure of the foil/sheet as a function of strain, using Vickers indentation, nano-indentation, optical microscopy and transmission electron microscopy (TEM). Microstructure characterization will involve examination of grain size and dislocation substructures. Note: Uniaxial strength measurements and electron back scatter diffraction (EBSD) characterization (for grain size distribution) will be done at PNNL.
- Identify the best processing conditions based on the property and microstructure characterization.
- In conjunction with PNNL, assess process scale-up, conduct cost-analysis, and suggest guidelines for process development for specific automotive applications.

Accomplishments

- Segmentation observed in preliminary experiments was overcome by tuning machining conditions to produce continuous AZ31 foils ~1 cm wide x 0.2 mm thick by both LSEM and peeling.
- A test matrix of ~20 different sets of machining conditions systematically varying strain, strain rate, and temperature showed segmentation could be suppressed for large positive rake angles, higher cutting speeds and preheating the workpiece.
- Up to a five-fold decrease in grain size was observed for the machining-based SPD processing with the smallest grain size of ~3 μm comparable to that observed in other types of SPD processing of AZ31.
- Modest hardness increases were measured, but preliminary tensile testing showed the foils exhibit strengths comparable to equal channel angular extrusion (ECAP) processed AZ31 together with large uniform tensile elongation, suggesting good formability.

Future Direction

- Samples of the large strain-processed materials will be supplied to PNNL for grain size and mechanical property evaluations. PNNL and Purdue will develop a cost model for scale-up of the process at the conclusion of the project.

Introduction

Shear strains in the 1–10 range can be imposed in a variety of materials, including those of moderate to high initial strength, in a single pass of a machining operation. Two variants of the chip formation process—LSEM and peeling—appear to be particularly attractive for the direct production of foil and sheet with ultrafine grain (UFG) microstructures. LSEM combines microstructure refinement by large-strain machining with simultaneous shape and dimensional control of the chip by "extrusion." *Peeling* is removal of material in the form of a strip (chip) with superimposed tension applied to the chip. The strain (hence the microstructure of the resulting strip) are controlled by the tool rake angle and applied tension. These approaches were used in preliminary experiments to create foils, which showed considerable segmentation that result in less than adequate mechanical strength. To overcome the segmentation challenge, pre-heating samples in the deformation zone of chip formation will be performed. A machining set-up has been devised for this purpose.

Results and Discussion

LSEM and peeling methods were applied to study the creation of foils by chip formation from Mg alloy AZ31. The preliminary experiments showed considerable segmentation of the chips, preventing realization of continuous foils. Subsequently, by using tools with large positive rake angles (15–45 deg) and higher machining speeds (100–1000 m/min), it was possible to create foils (chips) that were macroscopically continuous. While this indicated that the processing conditions were apparently accurate, microscopic observations still revealed segments in the foils. In addition, foil strength was not significant, consistent with the segmentation observed in the chips.

To overcome the segmentation challenge, pre-heating of the bulk Mg alloy sample up to 200°C in the deformation zone was employed to activate additional slip systems. This approach was based in part on work in the 1960s at the Atomic Energy Establishment in Saclay, France. A test matrix employing 11 different sets of peeling conditions (stain, strain rate, and temperature) and 8 different sets of LSEM conditions established the conditions for continuous foil production. Continuous foils ~1 cm wide and 200 μm thick were produced by both the LSEM and peeling processes. By adjusting conditions, continuous foils could be produced at ambient temperature using the LSEM process.

With grain refinement down to ~3 μm, a five-fold decrease from the starting bulk ("extruded") condition was observed (Figure 1). The grain size

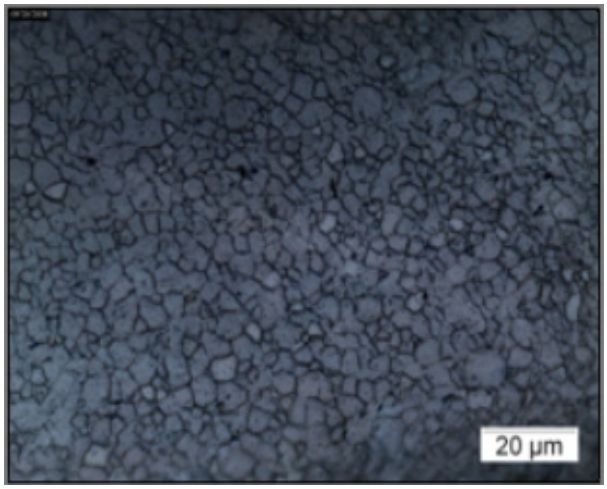

Figure 1. Continuous foil microstructure produced by LSEM at shear strain = 2, 25°C and cutting speed = 70 m/min. The means intercept grain size measured 4 µm with a uniform distribution through the foil cross-section.

distribution is uniform through the foil cross-section.

Only modest hardness increases of 5–10% were measured for the continuous foils, whereas hardness increases up to ~50% were observed in the segmented foils.

Preliminary tensile testing was conducted using test specimens cut from the continuous foils having 5.7 mm long × 2 mm wide (~0.2 mm thick) gage sections. Yield strength of ~160 megapascal (MPa) and tensile strengths up to 240 MPa with over 15% uniform elongation have been measured thus far. These properties are comparable to those reported for ECAP processed AZ31. Further testing is required to establish statistically significant tensile properties, but the results are certainly promising with respect to the anticipated forming characteristics.

Continuous foil production with UFG microstructures has been demonstrated successfully using the machining SPD approach in another hexagonal close-packed (HCP) system (titanium [Ti]) with similar deformation characteristics as Mg. Both ultra purity Ti (99.999%) and CP Ti (Grades 2 and 4) have been produced in foil form, with hardness values approximately twice that of the bulk microcrystalline material. The foils were in excess of 150 mm in length. Transmission electron microscopy showed the UFG microstructure to be composed of ~100 nm size grains. Stress-strain curves will soon be measured for these Ti foils and the resulting properties correlated with microstructure condition.

F. Formability of Continuous Cast Magnesium Sheet

Principal Investigator: Darrell Herling
Pacific Northwest National Laboratory
P.O. Box 999, Richland, WA 99352
(509) 375-6905; fax: (509) 375-4448; e-mail: darrell.herling@pnl.gov

Technology Area Development Manager: Joseph A. Carpenter
(202) 586-1022; fax: (202) 586-1600; e-mail: joseph.carpenter@ee.doe.gov

Field Technical Monitor: Mark T. Smith
(509) 375-4478; fax: (509) 375-4448; e-mail: mark.smith@pnl.gov

---

Contractor: Pacific Northwest National Laboratory (PNNL)
Contract No.: DE-AC06-76RL01830

Objective

- Characterize the post-formed properties of continuous cast magnesium sheet provided by the United States Automotive Materials Partnership (USAMP) Warm Forming Team (AMD 602).
- Evaluate the effects of tooling lubricant type on friction and formability under warm forming conditions.
- Determine the forming limits under biaxial conditions (limited dome height [LDH]) at warm forming temperatures.

Approach

- Mechanical testing of post-formed panels was received from original equipment manufacturers (OEMs) to characterize properties of continuous cast magnesium sheet, including ultimate strength and elongation to failure.
- A method was developed to evaluate the effects and down-select tooling lubricant types for warm forming magnesium sheet. Results will include coefficient of friction data for lubricant type as a function of temperature and formability under biaxial forming conditions.
- PNNL's warm biaxial forming equipment will be utilized to assist CANMET (Canada Centre for Mineral & Energy Technology) in developing biaxial forming limit diagram data and disseminate to the USAMP Warm Forming Team.

Accomplishments

- Initiated the project in late fiscal year (FY) 2008.
- Established a test plan for post-formed property characterization.
- Established both a plan and method to evaluate forming lubricants.

Future Direction

- Initiate and conduct mechanical property characterization on post-formed magnesium panels received from OEMs and the stamping supplier.

- Perform metallography on continuous cast magnesium sheet and post-formed panels in order to document microstructural and texture evolution during the warm forming process.
- Initiate biaxial formability testing and compare results with CANMET.

Introduction

The automotive industry is working continually toward reducing vehicle emissions and fuel consumption. A substantial portion of these efforts is focused on reducing overall vehicle weight. Magnesium technology gives automotive producers the ability to apply this low-density structural material selectively to automobiles ultimately to reduce cost, weight and fuel consumption. Magnesium sheet has potential application in body-in-white (BIW), body closures, interior frames/brackets and tubular components. A major barrier to use magnesium sheet is the cost of conventional wrought processing due to the hexagonal crystal structure and poor hot-short characteristics. Continuous casting of magnesium using twin-roll casting techniques offers the potential to reduce the cost of magnesium alloy sheet.

The work scope for this agreement was developed in conjunction with the USAMP Warm Forming Team (USAMP project AMD 602) and is directed at developing a fundamental understanding of the microstructure/formability relationship and post-formed properties of continuous cast sheet materials currently being considered for use by the domestic OEMs. The work focuses on a collaborative contribution to AMD 602 and is intended to work in conjunction with other program participants at the University of Virginia and CANMET.

PNNL will receive as-processed and as-formed samples from the USAMP project, will perform microstructural evaluations and analysis of failure modes and will relate these features to the formability measurements and experiments conducted collaboratively by USAMP and CANMET. Where needed, PNNL will conduct limited formability tests to complement work to be performed at the University of Virginia and CANMET.

Objectives

Currently, global suppliers are developing low-cost magnesium sheet. In this project, magnesium sheet from various suppliers and process variations will be tested to determine the warm formability and mechanical properties, hence suitability for automotive applications. The post-formed mechanical response of the supplied magnesium test panels will be characterized by room temperature tensile testing and endurance screening (fatigue). The microstructure will be documented primarily with optical microscopy and correlated to the processing methods and formability.

Formability is dependent on the friction characteristics between the sheet and tooling. As such, an evaluation of lubricants will be conducted to determine the most appropriate product that yields good formability and adequate surface finish. This testing will be conducted initially using the unique uniaxial friction test fixture at PNNL. This test rig will be set up with representative warm forming tool materials and both dry and synthetic lubricants. This uniaxial test will be used to screen lubricants for down-select, and further supplemental biaxial formability testing will be performed.

Finally, assistance will be provided to CANMET in developing forming limit diagram (FLD) data utilizing the heated-LDH test capabilities at PNNL. This work is designed to be synergetic to the effort led by CANMET in FLD development. CANMET is focused on FLD development using Marciniak in-plane stretching methods; biaxial stretching data will be complementary to this effort and will help establish a complete FLD.

Fiscal Year 2008 Activities

Activities at PNNL commenced in the latter part of 2008 and focused on establishing test matrices for post-formed property testing and lubricant evaluation. This included teleconference calls with

the USAMP Warm Forming Team to finalize the scope of work, schedules and define material sets of interest for evaluation and characterization.

Several post-formed magnesium panels have been received from the OEM participants, and test coupon schedules have been drafted. Mechanical testing of post-formed properties will commence in December 2008 and carry through the remainder of FY 2009.

In preparation for receiving magnesium samples for biaxial testing, heated LDH and Marciniak tooling was set up on an Interlaken, Inc. formability machine. The heated tooling will allow for warm formability experimentation to evaluate sheet deformation as well as lubricants. This testing will provide input into modeling and formability simulations led by the OEMs as well as the down-selection of adequate lubricant types for forming conditions up to 350°C.

Future Work

Fiscal year 2009 will be the first full year for PNNL activities in support of the magnesium warm forming program. With the receipt of materials from OEMs, PNNL can initiate the scope and conduct mechanical property characterization on post-formed magnesium panels as well as microstructural documentations. Also, a lubrication evaluation will be initiated with multiple types identified and planned for tribological evaluation. Finally, biaxial formability testing will be initiated and the results compared with work being performed at CANMET.

G. Development of High-Strength Superplastic Forming Aluminum Sheet for Automotive Applications

Principal Investigators: Curt A. Lavender, Daniel Edwards, Elizabeth Stephens
Pacific Northwest National Laboratory
P.O. Box 999, Richland, WA 99352
(509) 372-6770; fax: (509) 375-2186; e-mail: curt.lavender@pnl.gov
(509) 376-4867; fax: (509) 375-4448; email: dan.edwards@pnl.gov
(509) 375-6836; fax: (509) 375-4448; e-mail: elizabeth.stephens@pnl.gov

Technology Area Development Manager: Joseph A. Carpenter
(202) 586-1022; fax: (202) 586-1600; e-mail: joseph.carpenter@ee.doe.gov

Field Technical Monitor: Mark T. Smith
(509) 375-4478; fax: (509) 375-4448; e-mail: mark.smith@pnl.gov

---

Contractor: Pacific Northwest National Laboratory (PNNL)
Contract No.: DE-AC06-76RL0 1830

Objective

- Develop a cost-effective superplastic sheet with a post-formed strength greater than that of the commonly-used 5083 alloy.

Approach

- Identify candidate 5XXX, 6XXX, and 7XXX alloy systems.
- Establish operating limits for automotive pre- and post-superplastic forming (SPF) processes (such as heat-up rates and paint bake cycles) and assess alloy heat-treat response.
- Collaborate with aluminum (Al) suppliers to mill-process sheet materials with SPF microstructures based on selected 5XXX, 6XXX, or 7XXX alloy compositions.
- Demonstrate SPF of a high-strength sheet under simulated automotive manufacturing conditions.

Accomplishments

- A series of teleconferences were held with Sooho Kim and Paul Krajewski of General Motors (GM) and Peter Friedman of Ford to establish the automotive-specific objectives and processing constraints.
- Processing constraints were determined for:
  - Alloy superplasticity
  - Heating and cooling conditions
  - Forming rate and temperature
  - Post-SPF formability
  - Post-SPF heat-treat response during paint bake
- Two alloy systems were identified based on high-rate superplasticity developed by solute-drag (5XXX) and fine-grain size (6XXX), respectively.
- A biaxial forming die was fabricated with radii and forming depths consistent with expected automotive parts.

Future Direction

- Cast, homogenize, forge, and roll a series of alloys for evaluation for superplasticity by tensile testing using experimental heats.
- Form Al sheet materials using a biaxial forming die and evaluate the post-SPF mechanical properties using a test matrix of cooling rates and simulated paint bake cycles.
- Identify industrial Al mill to support process scale up.

Introduction

The objective of this project is to develop a cost-effective superplastic sheet with a post-formed strength >250 megapascal (MPa). Superplastic forming of Al alloys has been used in the forming of automotive outer body panels and closures. Because SPF involves forming of the Al sheet at elevated temperatures, the final formed material strength is similar to that of an annealed (soft) Al sheet. Current automotive SPF applications have focused on the use of Al 5083 alloy that, with relatively high magnesium content, develops a post-formed strength of ~150 MPa. The use of 5XXX-series Al alloys with magnesium (Mg) levels above 3% introduces the potential for stress-corrosion cracking (SCC) when exposed to an elevated temperature environment. The net result of these factors is that SPF 5083 alloys have been largely restricted from use in body-in-white (BIW) and under-hood applications where higher strength and resistance to SCC are required.

The current project is planned for three years and will evaluate a series of 5XXX-, 6XXX-, and 7XXX-series Al alloys to develop a modified alloy and mill processing methods to produce a high-strength SPF Al sheet with a post-formed strength of >250 MPa. The technical approach will evaluate modifications to existing heat-treatable alloys combined with thermo-mechanical processing methods to produce a fine-grained SPF sheet with a post-formed heat-treat response. The development of a fine-grain microstructure that remains stable at SPF temperatures generally requires a combination of alloy chemistry adjustment with hot and cold rolling into sheet. In the Al alloy system, individual alloy specifications contain significant ranges for many of the key alloying elements; from previous PNNL SPF development work, alloy modifications within the set alloy ranges can be used to optimize SPF microstructures. The focus of the project will be to develop a heat-treatable alloy that has a post-forming age-strengthening response compatible with automotive BIW thermal cycles (E-coat, paintbake). The result of the project will be development of a cost-effective SPF Al alloy sheet that can be used in higher-strength and elevated-temperature automotive applications, extending the use of SPF Al to BIW and underhood sheet components.

Automotive Superplastic Processing

Superplasticity

In order to meet the high-volume part production required for the automotive industry, it is unlikely that forming will be performed under ideal superplastic conditions (i.e., maximum strain-rate sensitivity or m-value). The criteria for superplasticity will be established by forming trials where the tray part (Figure 1) must be formed in less than 240 seconds (sec) or at an approximate strain rate of 1×10^{-3} sec^{-1}. Given that only very high-cost, rapidly-solidified powder metallurgy alloys have demonstrated fine-grained superplasticity at high rates, stable forming for this alloy will likely be achieved with a combination of solute drag and grain boundary sliding [1]. Temperatures for forming must be as low as possible in order maximize die life and minimize sheet oxidation; as a result, forming temperatures will be held below 515°C. Therefore, adequate "superplasticity" for this project has been defined as an alloy that can form to a minimum of 150% elongation at a strain rate greater than 1×10^{-3} sec^{-1} and at temperature less than 515°C.

Superplastic Forming Process

The automotive work-cell approach to superplasticity requires that the sheet blank be heated rapidly and the formed part cooled as

Figure 1. Superplastically-formed tray to be used as evaluation part for the high SPF alloy development project.

quickly as possible without excessive distortion in order to minimize production cost [2]. The fine grain size required for superplasticity in the conventional 5083 alloy is stabilized by a high level of second-phase eutectic constituent particles formed during ingot solidification and subsequent rolling. However, for Al alloys which harden by aging, the precipitate phases will dissolve during heating and therefore will provide no effective pinning of grains. In order to achieve fine grain sizes in age-hardenable alloys, a technique called particle stabilized nucleation (PSN) has been employed [3]. In PSN, an aged and cold-worked sheet is heated at high rates to maximize the number of grains nucleated while minimizing growth time. Fast heating rates are beneficial for both superplasticity and production rate; therefore, this parameter will be closely controlled.

Maximum age-hardening response in Al alloys is achieved from a solute-rich metastable solid solution formed by water quenching from a temperature where virtually all constituents are dissolved. However, when water quenches a complex shape such as an automotive panel, excessive distortion will require the use of re-strike tool, eliminating one of the most important advantages of SPF: low-cost tooling. Therefore, although high cooling rates are desirable for post-SPF paint-bake response properties, part distortion will determine that maximum cooling rate, like heating rate, will be a closely-controlled parameter.

Post-Superplastic Forming Properties

Post-SPF panel properties must be separated into two requirements: post-SPF formability and final part properties. For post-SPF formability, the panel must be ductile enough for secondary operations such as hemming and, therefore, must not exit the SPF die in the fully-hardened condition. The final part properties will be achieved after paint bake. If the strength level is greater than 250 MPa, a vehicle mass reduction of greater than 20% could be realized. However, typically high-strength Al alloys are susceptible to accelerated corrosion, particularly after cold work such as hemming. Alloying constituents known to promote accelerated corrosion such as copper (Cu) and zinc (Zn) will be avoided.

Superplastic Alloy Selection

The preceding section was a qualitative and quantitative analysis of the automotive SPF process in order to define the requirements of a high-strength SPF alloy. This analysis was required because many high-strength 2XXX and 7XXX SPF alloys have been developed for use in aerospace; however, the unique cost-sensitivity, corrosion and processing requirements (primarily production rate) of automotive prevent their use. The low-cost, high-strength SPF automotive sheet must be adapted to the existing low-cost SPF process.

The low-cost SPF process requires that the alloy be soft after SPF and achieve the 250 MPa strengths during the paint bake so that the panel can be subjected to secondary processing such as hemming, thereby eliminating alloys that might harden during the SPF process. This important requirement determines that the alloy must exit the SPF process with a metastable solid solution with adequate solute for precipitation. Therefore, the alloying elements must dissolve at 515°C or less and be retained in solution without a water quench. Previously, PNNL had demonstrated that this was possible with the 6013 alloy; however, the primary hardening phase was the AlMgCu, theta precipitate [4]. Given that Cu additions produce unacceptable corrosion resistance for automotive applications, the new alloy must rely on a silicon (Si) addition for precipitation hardening. A study similar to the previous 6013 alloy development will be undertaken, focusing on the precipitation hardening associated with Si rather than Cu.

The low-cost superplastically formable alloy composition can be summarized as follows:

1. Maximum eutectic constituent to minimize grain size (i.e., Manganese [Mn])
2. Minimum additions of Cu
3. Solution temperature less than 515°C
4. Age response consistent with a paint-bake cycle
5. Maximum solid-solution strengthening (Mg)
6. Maximum Si content.

The alloy development activity will focus on two base alloys: a 3.5% Mg 5XXX and a low Mg 6XXX. Each alloy will be modified to maximum Mn content to minimize grain size by nucleation and Mg/Si ratio to achieve maximum paint bake response. Commercially available compositions will be used, where possible. Elements such as Si, Mn, and the like will be skewed within the existing commercial tolerances to avoid development of alloys difficult to produce on an industrial basis.

Conclusions

During this reporting period, the following conclusions were derived:

- The high-strength SPF alloy must develop elevated strength by a post-forming aging treatment during the paint bake.
- The metastable solid solution required for paint bake response must be formed during the SPF process and subsequent cooling.
- The primary constituent for hardening during paint bake will be the Mg_2Si precipitate.
- Given the forming rates desired for automotive production, stable deformation will likely require a combination of fine-grained superplasticity and solute-drag.

Presentations/Publications/Patents

DOE Vehicle Technologies Program Annual Merit Review. February, 2008.

References

1. E. M. Taleff, “An Overview of Creep Deformation Behaviors in 5000-Series and Al-Mg Alloys,” 2004. *Advances in Superplasticity and Superplastic Forming*. Eds. E. M. Taleff, P. A. Friedman, P. E. Krajewski, R. S. Mishra, and J. C. Schroth, TMS (The Minerals, Metals & Materials Society).
2. J. C. Schroth, “General Motors Quick Plastic Forming Process,” 2004. *Advances in Superplasticity and Superplastic Forming.* Eds. E. M. Taleff, P. A. Friedman, P. E. Krajewski, R. S. Mishra, and J. C. Schroth, TMS (The Minerals, Metals & Materials Society).
3. N. E. Paton and C. H. Hamilton, “Method of Imparting A Fine Grain Structure to Aluminum Alloys Having Precipitating Constituents,” U.S. Patent No. 4,092,181, May 30, 1978.
4. C.A. Lavender, *Enhanced Plasticity in AA6013 at Elevated Temperatures,* Presentation at THERMEC 2006, Vancouver, British Columbia. July, 2006.

H. Aluminum Automotive Closure Panel Corrosion Test Program

Project Co-Chair: Tracie Piscopink-Jafolla
General Motors Corporation
3300 General Motors Road
MC: 483-370-101
Milford, MI 48380-3726
(248) 676-7014; fax: (248) 685-5279; e-mail: tracie.l.jafolla@gm.com

Project Co-Chair: Francine Bovard
Alcoa Technical Center
100 Technical Drive
Alcoa Center, PA 15069
(724) 337-3249; fax: (724) 337-2044; e-mail: Francine.Bovard@alcoa.com

Technology Area Development Manager: Joseph A. Carpenter
(202) 586-1022; fax: (202) 586-1600; e-mail: joseph.carpenter@ee.doe.gov

Contractor: United States Automotive Materials Partnership (USAMP)
Contract No.: FC26-020R22910 through the DOE National Energy Technology Laboratory

Objective

- Develop a standardized cosmetic corrosion test for finished aluminum automotive body panels that provides a good correlation with in-service testing and field performance.

Approach

- Conduct laboratory testing, outdoor exposures, test track exposures, and in-service testing.
- Evaluate test data to determine which accelerated tests correlate with in-service testing.
- Conduct iterative laboratory testing to improve correlation between lab tests and on-vehicle exposures.

Accomplishments

- Test track exposures, on-vehicle exposures, and outdoor exposures have been completed.
- Many laboratory tests have been conducted and compared with service-relevant exposures.
- Corrosion product analyses conducted for some laboratory tests and exposures on vehicles.
- Key environmental parameters have been identified as important for inclusion in an accelerated test for painted aluminum.

Future Direction

- As this program draws to a close, the remaining work will be focused on repeatability and reproducibility of the American Society for Testing and Materials **(**ASTM) G85-09 A2 and G85-09 A4 tests, the two accelerated corrosion tests that have shown the greatest promise at replicating in-service aluminum corrosion.

Introduction

All original equipment manufacturers (OEMs) and their suppliers rely on various laboratory tests to assist in prediction of real life service performance, even though it is well recognized that many of these lab tests do not fully represent observed corrosion behavior. Part of the difficulty lies in the large number of variables in service that influence corrosion rates and how to fully take all of these factors into account with one single test procedure. OEMs have also developed elaborate test tracks or proving ground tests in attempts to more closely simulate service conditions but in general the proving ground tests also have not correlated well with on-vehicle performance for painted aluminum [1–4].

In addition to real life corrosion conditions, there are also many factors in the OEM production process that influence the aluminum surface condition, chemical treatment and paint performance of a closure panel that are difficult to fully control on lab prepared panels. Nonetheless, the potential for time and cost savings that could be achieved by having a general agreement on a lab test capable of closely mimicking real life performance was highly desirable and in 2000 resulted in the formation of a group of representatives from the U.S. automotive manufacturers, aluminum industry, and coating and other suppliers to establish that correlation. Since then, a number of papers have been presented at the Society of Automotive Engineers (SAE) Congress [1–4] to disseminate the findings of this group to the automotive corrosion community.

In this progress report, the results of the past year's experimentation are reviewed. The latest results cover not only correlation of lab tests with the extent and morphology of in-service corrosion, but also an analysis of corrosion products to help determine whether the mechanisms of corrosion propagation are the same in lab and field exposure.

Experimental

Materials

The painted panels used in this program are listed in Table 1. The substrate materials, metal finish, and paint processing variables were selected to give a range of cosmetic corrosion performance.

Several aluminum alloys used in the Unites States and in Europe, both current and historical, were included, with two alloys processed to simulate metal finishing in an automotive assembly plant body shop. Panels made from electro zinc coated steel and uncoated cold rolled steel were included as reference materials [5].

Table 1. Materials

Panel code	Alloy substrate	Metal finish	Paint system
A or 1	AA6111-T4PD	Mill	Standard
B or 2	AA6111-T4PD	Mill	Low F^-
C or 3	AA6111-T4PD	Mill	Ecoat
D or 4	AA6111-T4PD	Sanded	Standard
E or 5	AA6016-T4	Mill	Standard
F or 6	AA6022-T43	Mill	Standard
G or 7	AA2036-T4	Sanded	Standard
H or 8	EG 60 steel	Mill	Standard
I or 9	CR steel	Mill	Standard

Two sizes of panels, 2 in. × 4 in. and 4 in. × 6 in., of each of the materials were painted with a typical automotive paint system. This paint system included zinc phosphate pretreatment, medium-build cathodic electrophoretic priming (E-coating), and spray painting with a primer surfacer and white basecoat/clear topcoat system for a total paint film thickness of approximately 100 μm. One set of 6111 panels (Panel Code B) was processed through the phosphate pretreatment with lower fluoride concentration (comparable to the fluoride level used for steel only vehicles which results in lower phosphate coating weight). Also, since qualification testing is often done on panels that are processed only through the electrophoretic primer (E-coat) step, another set of 6111 panels (Panel Code C) was processed only through the E-coat step (i.e., standard fluoride for Al but no basecoat or clear coat applied). Panel code C was evaluated in lab tests only (no on-vehicle or proving ground exposures).

Panels were prepared as needed for testing with two parallel scribes penetrating through the coatings to the substrate. The panels were provided to the testing laboratories as fully

prepared painted and scribed panels. Triplicate sets of the painted and scribed samples have been exposed in a variety of environments, including: laboratory, static outdoor exposure, proving ground, and on-vehicle exposure.

Evaluation Method

For this study, an optical imaging system developed by Atlas Material Testing Technology, LLC was employed to quantitatively interpret the degree of cosmetic corrosion. The imaging system employs controlled illumination conditions, high-resolution digital image capture, and advanced algorithm-based image and data analysis methodologies [6].

Four geometrical attributes of the cosmetic corrosion were measured: area of corrosion, maximum length, minimum length, and average length. The area of corrosion was found to be the most representative and comprehensive measurement. Because the size of the panels and therefore the scribe lengths for the lab tests were different from the other tests, the corrosion area was normalized to the length of the scribe (i.e. area per length). The normalized corrosion areas for triplicate panels (two scribes per panel) were then averaged and the results are reported as "normalized average area."

On-Vehicles Exposures

It is critical when developing a laboratory based test that test-to-field correlation be performed. In an effort to capture real-world data in developing this test, it is preferable to expose these panels to severely corrosive environments that represent "worst case" real-world service environments. Suitable environments exist in the northeastern United States, southeastern coastal areas of the United States, and southeastern Canada. Two of these environments (northeastern United States and southeastern Canada) were part of this program. The sites selected for this study were: (1) Detroit, Michigan, (2) St. John's, Newfoundland, (3) Montreal, Quebec, and (4) Cleveland, Ohio, to Buffalo, New York, truck route. Two sets of 2 in. × 4 in. test panels are exposed on each vehicle (two vehicles per site). Each set of 24 (three each of eight material variables) were attached to a mounting panel (16 in. × 12 in.) using double-backed tape prior to mounting on the vehicle. At the Detroit, St. John's, and Montreal sites, one set is mounted on the hood of each vehicle (horizontal orientation) and one set on the right front door of each vehicle (vertical orientation). For the Ohio-New York (OH/NY) truck route the panels were mounted beneath the trailer frame behind the front wheels (vertical orientation only). Each panel contains two diagonal scribe lines which are 2 in. long and 1 in. apart. The panels were exposed for a total of 4 years of in-service exposure. Intermediate evaluations were conducted when possible. Upon completion, the panels were removed and sent to Atlas Material Testing Technology, LLC for evaluation.

Laboratory Tests

Several rounds of laboratory testing have been conducted to date [1–4]. All of the accelerated laboratory tests that have been evaluated thus far are listed in Table 2.

Table 2. Laboratory tests evaluated in this program

	Test Procedure	Duration
1	SAE J2334	40, 60, and 80 cycles
2	ASTM D2803 (80% RH)	6 weeks
3	Modified ASTM D2803 (60% RH)	6 weeks
4	Modified ASTM D2803 (100% RH)	6 weeks
5	ASTM G85-09 A 2	1, 2, and 3 weeks
6	VDA 621-415	10 cycles/ 70 days
7	ASTM B117	500 and 1,000 hours
8	CCT IV	35 and 70 cycles
9	KWT	6 weeks
10	Ford Arizona Proving Ground Exposure (APGE) (Manual)	35 and 70 cycles
11	Ford APGE (Automated)	35 and 70 cycles
12	HCl Dip	3, 6, and 8 weeks
13	GM9511P	4 weeks
14	GM9682P	4 weeks

Table 2. (continued)

	Test Procedure	Duration
15	ASTM G87	20 cycles
16	ASTM G85-09 A5	500 hours
17	ASTM G85-09 A4 (continuous spray)	500 hours
18	ASTM G85-09 A4 (intermittent spray)	500 hours
19	Modified ASTM G85-09 A4 (continuous spray)	500 hours
20	Modified ASTM G85-09 A2	500 hours

Subsequent to comparison of the results from several rounds of laboratory tests (performed in the preceding years) with preliminary results from on-vehicle exposure; the list of lab tests of interest has been narrowed to the following for 2008 and beyond:

- ASTM G85-09 A2—Cyclic Acidified Salt Spray Test [7]
  - Test Cycle: 6 hour repetitive cycle with 3 steps/cycle:
    - 45 min. *Spray*
    - 2 hour dry-air *Purge*
    - 3 hour + 15 min *Soak* (RH gradually increases during soak)
  - Test Solution: 5% NaCl acidified to pH = 2.8–3.0 with acetic acid
  - Temperature: 49°C (120°F)
- ASTM G85-09 A4—Salt/SO_2 Spray Test (Continuous) [8]
  - Test Cycle: 6 hour repetitive cycle Continuous *Spray*; *w*ith introduction of SO_2 gas for 1 hour each cycle
  - Test Solution: 5% NaCl acidified to pH = 2.5–3.2
  - Temperature: 35°C (95°F)
- ASTM G85-09 A4—Salt/SO_2 Spray Test (Intermittent) [8]
  - Test Cycle: 3 hour repetitive cycle with 3 steps/cycle:
    - 30 min *Spray*
    - 30 min SO_2
    - 2 hour *Soak*
  - Test Solution: 5% NaCl acidified to pH = 2.5–3.2
  - Temperature: 35°C (95°F)
- HCl Dip Test
  - Test Cycle: 1 week cycle with 3 steps/cycle:
    - Immersion for 2 minutes at 35°C
    - Drip dry for 28 minutes in lab air
    - 143.5 hours at 40°C and 85% RH
  - Test Solution: 3.1% HCl
- APGE Simulation Test
  - Test Cycle: 24 hour repetitive cycle with 3 steps/cycle:
    - Immersion for 15 minutes at 23°C
    - Drip dry for 1.25 hours in lab air
    - 22.5 hours at 50°C and 85–90% RH
  - Test Solution: 5% NaCl pH = 6–8

Although the HCl Dip and APGE tests had shown some degree of correlation with the on-vehicle exposure results and they continue to be of some interest, they were not the focus of the work done in 2008. This work concentrated on the ASTM G85-09 A2 and A4 (including their variants) accelerated tests and corrosion product analysis.

Corrosion product analysis of panels from preliminary on-vehicle testing indicated that sulfur and chloride are significant components in aluminum corrosion products. Prior to 2007, none of the tests evaluated incorporated any form of sulfur. Another factor that has influenced the lab test selection process is that on-vehicle exposures tended to produce higher corrosion levels than the results seen in the many lab tests. Generally, the solutions used for lab tests that showed little or no corrosion were neutral pH and it became evident that more acidic environments in the lab tests increased the extent of the corrosion observed.

ASTM G85-09 A2 and ASTM G85-09 A4 (continuous spray) were previously identified as lab tests that most closely mimicked in-service corrosion performance in terms of the type and extent of the corrosion. The ASTM G85-09 A4 (continuous spray) test with SO_2 and NaCl in the exposure environment was the only test that had exhibited sulfur in the corrosion products.

Therefore, testing in 2008 was conducted to determine reproducibility of this test. The alternate cycle of the ASTM G85-09 A4 (intermittent) was also evaluated.

OEM Test Track Exposure

Completed OEM test track results were published previously [3] and are not repeated in this report.

Outdoor Exposure

Completed outdoor exposure test results were published previously [3] and are not repeated in this report.

Corrosion Product Analysis

Corrosion product analysis was performed on panels A, D, G, and I removed from 4-year long exposures on vehicles in St. John's and Montreal. In addition, panels from ASTM G85-09 A4 test (incorporating SO_2 gas) have also been examined in this study. For the top down analysis of the corrosion products, the paint layer was stripped in 1-methyl-2-pyrrolidone solvent. Water was not used during the stripping procedure so as to preserve any chloride/sodium species present within the corrosion product.

The panels were examined using a Leo 440 Scanning Electron Microscope (SEM) equipped with a Quartz XOne Energy Dispersive X-ray (EDX) analysis system. SEM/EDX technique was chosen for this examination because the amount of corrosion product on aluminum closure panels is very small, making more traditional analytical procedures impractical. In addition, the use of SEM/EDX allows not only for a measurement of the chemical species present, but also for an analysis of the distribution of these species in and around the corroded area on the panel. This technique is relatively sensitive with detection limits sometimes less than 0.1% w/w for most elements including sulfur and chlorine, which are the species of interest in this study.

Results and Discussion

On-Vehicle Exposures

Although the extent of corrosion in the on-vehicle exposures varied considerably from vehicle to vehicle for the various sites, panels D, G, and I typically exhibited significantly more corrosion than the other substrates, as illustrated by the images in Figure 1. The aluminum panels with metal finishing (D and G) generally have more corrosion than the other aluminum substrates, and cold rolled steel (I) has more corrosion than the electro-galvanized steel (H). Normalized average area from on-vehicle service relevant exposures in Detroit, Montreal, St. Johns, and the OH/NY Truck route are plotted in Figure 2. In this plot the results for the aluminum panels with metal finishing (D + G) have been averaged and the results from the other aluminum panels with standard paint system (A + E + F) have been averaged. Where possible, the results for the hood (H = horizontal) and door (V = vertical) locations are also indicated. For the 4-year exposures in Montreal the traceability of the locations was not certain so the results for H and V locations have been combined into a single average area. In the Detroit and St. Johns exposures the corrosion was more severe in the H location, but in the Montreal exposures the corrosion tended to be more severe in the V location. For the OH/NY highway trailers, panels were exposed in a vertical position only. Based on these on-vehicle results, only those accelerated tests that show a significant difference between the aluminum substrates with metal finishing (i.e., sanding) and those without metal finishing are currently being considered.

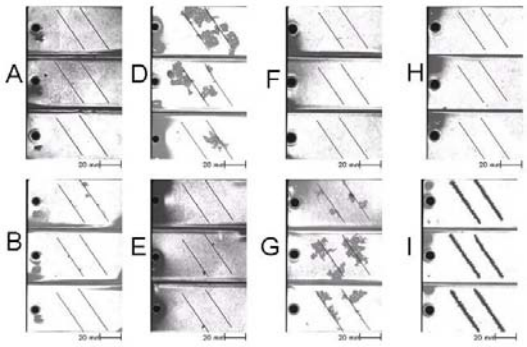

Figure 1. Images of the 3 replicate panels of each substrate from a Detroit on-vehicle exposure with ~2 years' exposure.

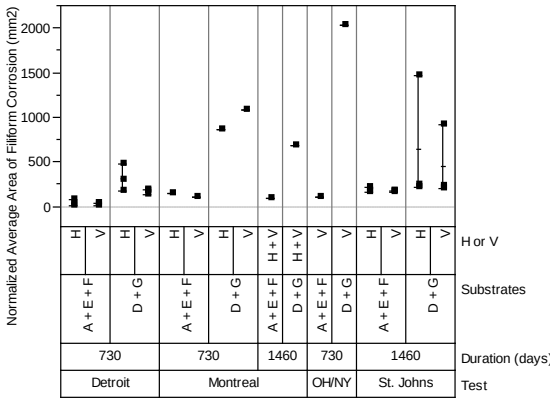

Figure 2. Compiled results from on-vehicle exposures with 2 and 4 years' exposure.

Regardless of position on the vehicle, the aluminum panels with metal finishing (D + G) exhibited more corrosion than the other aluminum panels with standard paint system (A + E + F) at all of the different exposure sites. This is consistent with other reports in the literature which indicate that metal finishing significantly impacts the susceptibility to filiform corrosion [9,10]. In 1997 Colvin et al. [9] evaluated the filiform corrosion performance of sanded vs. mill finish aluminum surfaces with zinc phosphate pretreated and painted panels in several different service environments. They observed that sanded surfaces exhibited significantly more corrosion and paint delamination in both seacoast and on-vehicle exposures. In this same study, an in depth evaluation of the impact of sanding on the deposition and growth of zinc phosphate crystals on aluminum surfaces was conducted [10]. The impact of the sanding on the filiform corrosion was attributed to localized inhibition of zinc phosphate precipitation which resulted in inconsistency of the zinc phosphate pretreatment layer on sanded surfaces.

Figure 3 presents the optical micrographs of the panels from a St. John's on-vehicle test with ~4 years' exposure. These panels were placed in the hood (horizontal) location and indicate that the aluminum panels with metal finishing (D + G) exhibited greater corrosion than the standard aluminum panel (A). In addition, the steel panel (I) also exhibited significant blistering around the scribe marks. The panels from the door (vertical)

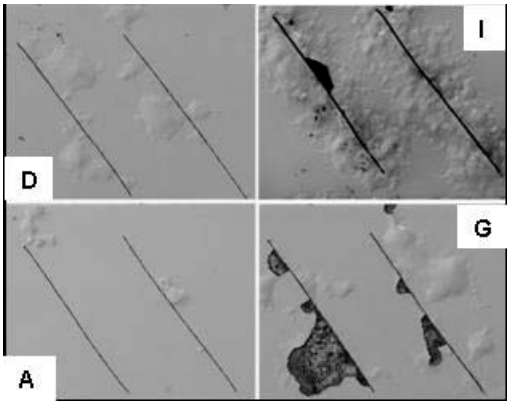

Figure 3. Images of the panels of four substrates from a St. John's on-vehicle exposure (hood) with ~4 years' exposure.

location and the panels from 4-year Montreal exposures also exhibited a similar trend.

Figure 4 presents the secondary electron micrograph and the elemental distribution maps for chlorine, sulfur, and aluminum for the G panel from the hood location at 4 years' exposure in St. John's. In the elemental distribution maps, the brighter regions qualitatively represent the greater presence of the element of interest. The white arrow in this figure indicates the scribe mark. The elemental distribution maps indicate the presence of sulfur species at the scribe mark and at the coarse corrosion product regions. Chloride species were observed at the tip of the filiform filament.

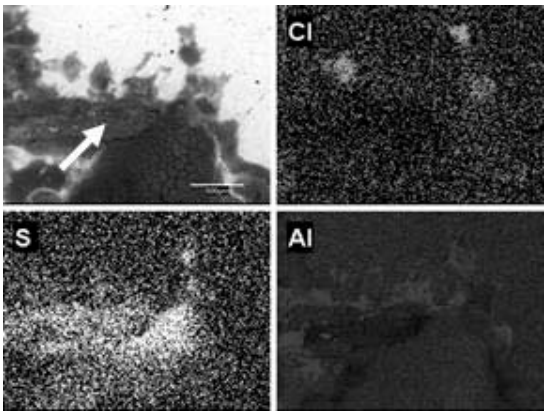

Figure 4. Secondary electron micrograph (top left) and elemental distribution maps for sulfur, chlorine, and aluminum from panel G of 4-year St. John's exposure (hood). In these images, brighter regions represent greater presence of the element of interest. Scribe mark is indicated by the arrow in this figure.

This trend is consistent for all panels from St. John's exposure including those from hood and door locations.

It should also be mentioned that while filiform corrosion was observed on the aluminum panels, the steel panel (I) exhibited a more uniform corrosion attack. Corrosion products in the steel panel also exhibited greater presence of chlorides compared to sulfur species. Finally, the corrosion product morphology and its composition on the 4-year exposure panels are similar to those observed from the 2-year exposure panels [2].

Table 3 presents the results from the EDX spot analysis of the corrosion products on the 4-year St. John's exposure panels (hood). Composition of the corrosion products was determined at three different locations. The results indicate that the aluminum panels, in general, exhibited sulfur species at more locations than the chloride species. In addition, as discussed previously, the steel panels did not exhibit sulfur enrichment to the same extent as the aluminum panels. Besides sulfur and chlorine, sodium, potassium and calcium were also detected, mostly at the scribe marks. These could arise from the presence of de-icing salts. Finally, other elements like magnesium (Mg), silicon (Si), phosphorous (P), manganese (Mn) and titanium (Ti) (not shown in the table) were also detected within the corrosion products.

Table 3. Composition of corrosion products from 4-year St. John's exposure (hood)

Panel ID	Number of Spots	Elements Detected (wt. %)									
		C	O	Na	Al	S	Cl	K	Ca	Fe	Zn
A (Hood)	4	11.3	51.1	0.2	23.8	1.7	0.2	0.1	4.9	0.4	1.9
D (Hood)	6	10.1	44.0		36.1	0.7	2.4		0.1		2.5
G (Hood)	9	9.0	51.9		25.9	0.8	1.3	0.2	0.1	0.2	4.3
I (Hood)	3	8.4	32.8	1.0	3.2	0.0	0.1	0.9	0.5	41.3	

Figure 5 presents the secondary electron micrograph and the elemental distribution maps for chlorine, sulfur, and aluminum for the G panel from 4 years of exposure in Montreal. As before, in the elemental distribution maps, the brighter regions qualitatively represent the greater presence of the element of interest. The scribe mark and the corrosion originating from the scribe mark could be clearly seen in this figure. In general, the Montreal panels qualitatively appeared to exhibit

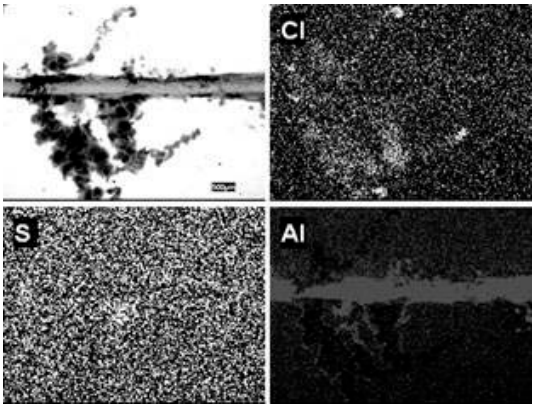

Figure 5. Secondary electron micrograph (top left) and elemental distribution maps for sulfur, chlorine, and aluminum from panel G of 4-year Montreal exposure.

less corrosion than the St. John's panels. The elemental distribution maps indicate the presence of chloride species within the corroded regions. Sulfur was detected at very few locations within the scribe mark. This is consistent with the results from the 2-year Montreal exposures [2]. This is also in contrast with the results from the St. John's exposures in which greater amounts of sulfur species could be detected within the corrosion products.

Unlike the aluminum panels, the steel panel (I) from Montreal exposure did not exhibit filiform corrosion, a trend consistent with the results from previous exposures [1,2]. Also, similar to the St. John's 4-year exposures, the steel panel exhibited greater levels of chloride species compared to the sulfur species.

The results presented in Figure 5 are also confirmed by the EDX spot analysis performed at various locations within the corrosion products. The results from these measurements are presented in Table 4. This table shows that chloride species were detected at greater locations on the aluminum panels compared to the sulfur species. In addition, the steel panel exhibited fewer sulfur-containing locations compared to the aluminum panels.

To determine the source of sulfur and chloride species, aluminum wire-containing CLIMAT units were exposed to atmospheric conditions in Montreal for a period of 3 months. Analysis of the

deposit on the aluminum wires indicated the presence of both sulfur and chlorine species with concentrations ranging from 0.3 to 2.6% by wt. for sulfur and 1.9 to 6.8% by wt. for chlorine. Thus, the results from the atmospheric corrosion exposures are consistent with those from the corrosion product analysis reported in Table 4. A similar exercise is being performed in St. John's in which the deposits on the aluminum wire exposed for a certain period will be examined by SEM/EDX technique. It is expected that results from the CLIMAT sample will be useful in explaining the trends observed in the corrosion product analysis from St. John's location.

Table 4. Composition of corrosion products from 4-year Montreal exposure

Panel ID	Number of Spots	Elements Detected (wt. %)									
		C	O	Na	Al	S	Cl	K	Ca	Fe	Zn
A	5	18.7	33.9	0.1	39.7	0.1	1.2				3.4
D	7	14.0	21.1	0.3	28.8	0.1	0.2	0.2	1.2		1.2
G	6	15.8	29.7		26.5	0.1	0.5	0.3	1.0		4.0
I	3	15.4	32.2	0.3	1.8	0.3	0.2	1.0		43.0	3.1

Laboratory Test Results

The normalized average area results from the ASTM G85-09 A2, the ASTM G85-09 A4 (constant spray) and the ASTM G85-09 A4 (intermittent spray) tests are shown in Figure 6.

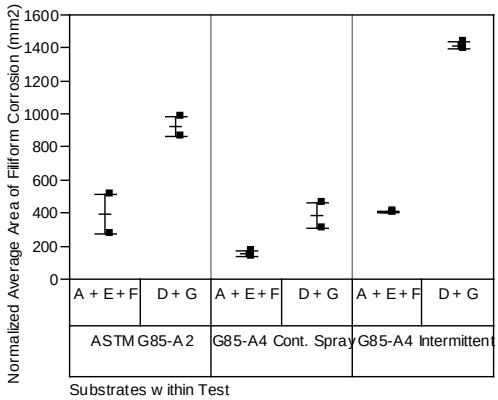

Figure 6. Normalized average area results from the ASTM G85-A2, the ASTM G85-09 A4 (constant spray) and the ASTM G85-09 A4 (Intermittent spray) tests. Duration for all 3 tests = 21 days (~500 hours).

All three tests show more corrosion area on the aluminum panels with metal finishing (D + G) than the other aluminum panels with standard paint system applied to the mill finish (nonsanded) substrates (A + E + F). The intermittent spray cycle for the ASTM G85-09 A4 test is more severe than the constant spray test and therefore appears to better differentiate between the sanded and mill finish panels. However, relative to the on-vehicle exposures, the intermittent ASTM G85-09 A4 and the ASTM G85-09 A2 test slightly over-predicted the corrosion for the mill finish substrates.

The lab test results are compared with the on-vehicle results in Figure 7. The diagonal line in the plot represents a 1:1 correlation between "D + G" and "A + E + F". All of the data for both the on-vehicle and the three lab tests are above the line reflecting the fact that the more corrosion occurred on the sanded panels (D + G) than on the nonsanded panels (A + E + F). The numbers next to the symbols on the plot are the actual ratios of (D + G) to (A + E + F). For the on-vehicle exposures the ratios range from 6:1 to 26:1. The ratios are lower for the lab tests (for example, the ASTM G85-09 A4 intermittent spray test has the highest ratio for the lab tests at 3.5:1).

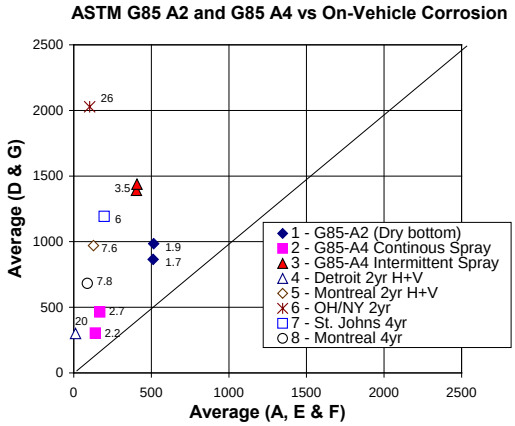

Figure 7. Average normalized corrosion area (mm^2) for substrates "A + E + F" versus that for substrates "D + G" for on-vehicle exposures and lab tests: ASTM G85-09 A2, ASTM G85-09 A4 (constant spray) and ASTM G85-09 A4 (intermittent spray).

Figure 8 shows representative images of substrate D after the ASTM G85-09 A2 and ASTM G85-09 A4 accelerated tests. Comparison of the morphology of the corrosion in these tests with those on substrate D from the on-vehicle exposures (Figure 1) shows that the corrosion

tends to be more continuous along the scribe line in the lab tests than is observed in the on-vehicle exposures. Of these three lab tests the morphology of the corrosion in the ASTM G85-09 A4 (continuous spray) appears to be more similar to that from the service relevant exposures on vehicles.

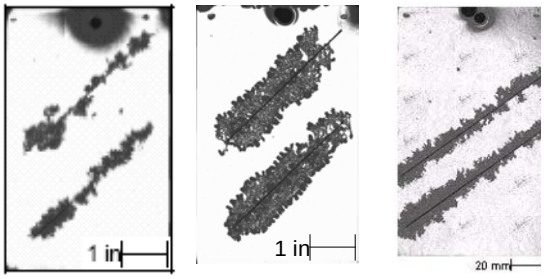

Figure 8. Images of corrosion on substrate D after accelerated corrosion testing.

Corrosion product analysis was also performed on the aluminum and steel panels exposed to G85-09 A4 (constant and intermittent) and G85-09 A-2 tests. The results from the G85-09 A2 tests have been reported previously [1] and hence only the results from G85-09 A4 tests will be presented here.

Visual examination of the G85-09 A4 test panels indicated that the intermittent salt spray exposure resulted in a more extensive corrosion along the scribe mark for the aluminum panels. However, the lengths of a few individual filiform tracks were greater for the continuous salt spray tests. For the steel panels, both tests produced similar corrosion behavior, though a slightly greater amount of corrosion was observed for the intermittent salt spray exposures. Corrosion product analysis indicated that the corrosion product composition was similar in both cases and, hence, only the results from the constant spray tests will be presented here.

Figure 9 presents the secondary electron micrograph and the elemental distribution maps for chlorine, sulfur, and aluminum for the panel D exposed to ASTM G85-09 A4 constant spray salt test. In the elemental distribution maps, the brighter regions qualitatively represent the greater presence of the element of interest. The scribe mark is at the bottom of the figure, running parallel to the bottom edge. Sulfur species were observed to be present at the scribe mark and at the coarse corrosion product regions. Chloride species were detected at the edge of the corrosion products and at the tip of the filiform filament. Thus, the results presented in this figure show that this test closely mimics the results from the St. John's 4-year exposure panels.

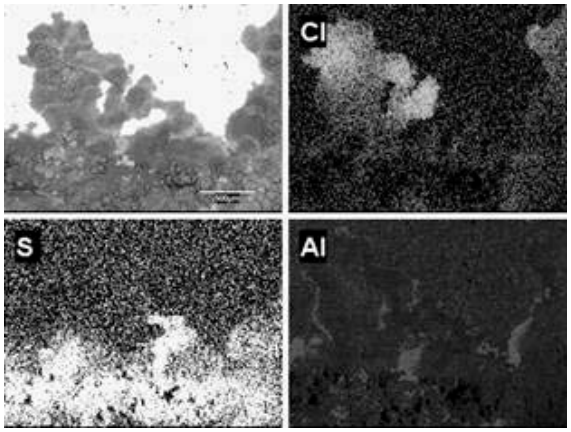

Figure 9. Secondary electron micrograph (top left) and elemental distribution maps for sulfur, chlorine and aluminum from panel D exposed to ASTM G85-09 A4 (constant spray) salt spray test.

EDX spot analyses were also performed at selected locations within the corrosion products on panels A, D, G, and I. The results from the EDX analysis are presented in Table 5. It should also be noted that, in addition to the elements shown here, Mg, Si, P, and Mn were also detected within the corrosion products. The results presented in this table indicate that sulfur and chloride species could be detected in significant quantities at most of the regions analyzed. Thus, this test appears to encompass the features observed from the 4-year on-vehicle exposures at St. John's and Montreal.

Table 5. Composition of corrosion products from ASTM G85-09 A4 (constant spray) laboratory salt spray test

Panel ID	Number of Spots	Elements Detected (wt. %)									
		C	O	Na	Al	S	Cl	K	Ca	Fe	Zn
A	7	10.8	49.9	0.6	30.6	1.5	2.1				2.6
D	6	13.8	46.1	0.9	30.4	1.4	1.6				3.4
G	8	11.2	48.8	0.6	26.2	1.3	1.3				6.1
I	6	11.2	29.3	0.2	0.8	2.4	4.2			46.8	2.9

Conclusions

An evaluation of the 4-year, in-service panel exposures shows that all of the panels that were exposed to metal finishing (sanding) prior to paint application exhibit a significantly higher level of filiform corrosion than those that were not sanded. Although a detailed understanding of the mechanism for the higher level of corrosion for sanded aluminum is outside the scope of this project, this result is consistent with the results of other studies [9, 10]. Because of this observation, the sanded panels were considered as a separate group from the nonsanded (mill finish) panels in comparisons of accelerated corrosion test results to the in-service exposure results.

Another observation from the in-service panel exposures was the presence of sulfur along with chloride in the corrosion product on aluminum panels. It is interesting to note that sulfur was found only in the corrosion products on the aluminum panels and not in the corrosion products on steel panels that were exposed to the same environment. The presence of sulfur in the corrosion products of in-service aluminum exposure panels led to an evaluation of accelerated corrosion tests that include sulfur in the exposure. It is unclear what the mechanistic role of sulfur is in the corrosion (beyond the scope of this project), but to mimic corrosion products observed on in-service aluminum sheet corrosion in certain atmospheric environments, sulfur may need to be included in the accelerated test exposure.

The accelerated corrosion tests that show the greatest promise at mimicking in-service aluminum corrosion are ASTM G85–09 A2 and ASTM G85–09 A4. Both of the accelerated tests were acidified to a pH of 2.5–3.2. An acidic exposure environment appears to be a key parameter when trying to mimic in-service corrosion performance with an accelerated test. However, many of the industry accepted standards for accelerated corrosion tests of steel are run in neutral environments. Neutral environments evaluated in this program induced little or no corrosion on the painted aluminum panels. While the ASTM G85—Annex 2 does not include sulfur in the exposure, the acidic exposure provides the necessary environment to induce corrosion on aluminum that replicates the morphology of corrosion on the in-service panels. ASTM G85-09 A4 provides both the acidic exposure and the exposure to sulfur, but can be a difficult test to run due to the use of sulphur dioxide (SO_2) gas. Although attempts were made to modify both of these tests using sulfuric acid in the exposure, it was found that sulfuric acid in the exposure was not as effective at inducing corrosion on the painted aluminum panels as either acetic acid in ASTM G85–A2 or with the SO_2 in ASTM G85–A4.

Presentations/Publications/Patents

SAE 2002B-203
SAE 2003-01-1235
SAE 2005-01-0542
SAE 2006 Oral Only
SAE 2007-01-0417
SAE 2008-01-1156

References

1. F. S. Bovard, J. Tardiff, T. Jafolla, D. McCune et al., “Development of an Improved Test for Finished Aluminum Autobody Panels,” SAE Paper No. 2008-01-1156, SAE 2008, April 2008.

2. F. S. Bovard, J. Tardiff, T. Jafolla, D. McCune, et al., “Update on the Development of an Improved Test for Finished Aluminum Autobody Panels,” SAE Paper No. 2007-01-0417, SAE 2007, April 2007.

3. F. S. Bovard, J. Tardiff, T. Jafolla, D. McCune, et al., “Development of an Improved Test for Finished Aluminum Autobody Panels,” SAE Paper No. 2005-01-

0542, SAE 2005 Transactions Journal of Materials and Manufacturing, March 2005.

4. G. Courval, K. Smith, C. Meade, F. Lutze, et al., "Development of an Improved Test for Finished Aluminum Autobody Panels," SAE Paper No. 2003-01-1235, Proceedings of SAE World Congress, March 2003.
5. SAE J2334, "Cosmetic Corrosion Lab Test," Society of Automotive Engineers, Warrendale, PA, June 1998.
6. Lee, F., B. Pourdeyhimi, and K. Adamsons, "Analysis of Coatings Appearance and Surface Defects Using Digital Image Capture/Processing/Analysis," The International Symposium on a Systems Approach to Service Life Prediction of Organic Coatings, Breckenridge, CO, Sept. 14–19, 1997.
7. ASTM G85-09 98 Annex 2, "Cyclic Acidified Salt Fog Testing," Annual Book of ASTM Standards, Vol. 3.02, 2005.
8. ASTM G85-09 98 Annex 4, "Salt/SO2 Spray Fog Testing," Annual Book of ASTM Standards, Vol. 3.02, 2005.
9. E. L. Colvin et al., "Filiform Corrosion of Aluminum Auto Body Sheet in Accelerated and Outdoor Environments," SAE Paper No. 970735, Proceedings of SAE World Congress, Feb. 1997.
10. L. F. Vega et al. "Influence of Surface Treatments on Durability of Painted Aluminum Alloys," SAE Paper No. 970731, Proceedings of SAE World Congress, Feb. 1997.